5-26-2006

High Pressure Chemical Vapor Deposition: A Novel Approach for the Growth of InN

Vincent Timothy Woods

HIGH PRESSURE CHEMICAL VAPOR DEPOSITION: A NOVEL APPROACH FOR THE GROWTH OF INN

by

VINCENT TIMOTHY WOODS

Under the Direction of Nikolaus Dietz

ABSTRACT

The development of next generation devices for high speed switching, high efficiency energy conversion, spintronic devices require the development of advanced material systems. While conventional group IV, group II-VI and group III-V based materials systems have served as a base material in many modern device structures, they posses fundamental materials properties that limit their suitability in next generation device structures. The group III-N material system is very promising for the development of advanced device structures. GaN is currently widely used in high efficiency lighting applications. However, the development of this material system has been limited to material systems with limited indium. The growth of high indium concentration materials such as InN and $Ga_xIn_{1-x}N$ has proven difficulty due to the high thermal decomposition pressure of InN. In response to this difficulty, a high pressure chemical vapor deposition reactor system has been developed for the growth of InN which enables elevated processing temperatures as compared to conventional low-pressure growth techniques. The

design criteria and implementation of this unique design is presented here. In addition, the results of *in-situ* real time optical characterization capabilities of this reactor system are presented as applied to thermal characterization, flow dynamics, gas phase kinetics and surface reactions. *Ex-situ* InN thin films grown on sapphire substrates and GaN epilayers have been analyzed by x-ray diffraction, transmission spectroscopy and raman spectroscopy. These results indicated single crystal indium nitride films with an optical absorption edge which varies between 0.7 and 1.9 eV as a function of precursor flow stoichiometry.

INDEX WORDS: Indium nitride, Real time optical characterization, Nitrides, High pressure, Chemical vapor deposition, Flow dynamics, Gas phase kinetics

HIGH PRESSURE CHEMICAL VAPOR DEPOSITION: A NOVEL APPROACH FOR THE GROWTH OF INN

by

VINCENT TIMOTHY WOODS

A Dissertation Submitted in Partial Fulfillment of the Requirements for the Degree of

Doctor of Philosophy

in the College of Arts and Sciences

Georgia State University

2006

HIGH PRESSURE CHEMICAL VAPOR DEPOSITION: A NOVEL APPROACH FOR THE GROWTH OF INN

by

VINCENT TIMOTHY WOODS

Major Professor:	Nikolaus Dietz
Committee:	Vadym M. Apalkov
	Douglas Gies
	Mark Stockman
	Brian Thoms

Electronic Version Approved:

Office of Graduate Studies
College of Arts and Sciences
Georgia State University
May 2006

Dedication

This work is dedicated to my wife Mary. She has made enormous sacrifices in order for me to fulfill my dream of attaining a Ph.D.. Her love, dedication, and constant support gave me the strength to complete this work.

ACKNOWLEDGEMENTS

I would like to acknowledge support of this work by:

- NASA grant NAG8-1686, DOD MURI Grant F-49620-95-1-0447.
- The collaborative support by Prof. Ferguson and his research group at Georgia Institute of Technology.
- Support through GSU-RPE.

I would also like to acknowledge the steadfast support of Nikolaus Dietz, Ph.D.. His constant vigilance, patience and guidance has enabled me to achieve results.

Finally, I would like to thank my father, Hugh “Roy” Woods, Ph.D.. His support and understanding of the difficulties which accompany earning a Ph.D. were essential to help me persevere through the inevitable difficulties which I encountered.

TABLE OF CONTENTS

LIST OF TABLES

LIST OF FIGURES

LIST OF FIGURES

1 Motivation

1.1 Introduction

The development of micro-electronic devices based upon semiconducting material systems has radically changed the abilities and lifestyles of mankind. In the short period of time since the invention of the first solid state transistor, the influence of these devices on modern life has become practically immeasurable. Micro-electronics have been developed from the research laboratory environment to the present where they are found in devices with applications ranging from alarm clocks and wristwatches, to medical pacemakers and deep-space probes. While there remains no doubt as to the profound influence that these electronic devices have had up to now, great effort will be required to provide the base material systems the next-generation device structures.

Currently, there exists great need for devices for applications such as ultra-high speed switching, high temperature-high power radiation hardened amplification, opto-electronic emitters/detectors and spintronic devices that will require fundamental advances in the areas of material science, device processing and device engineering. The following sections provide a survey of current semiconductor technology with respect to these applications and the areas in which material systems advancements are required for the realization of new applications

1.2 Status of current semiconductor technology

Technological advances have been made with regard to microelectronic device applications, requiring major efforts in the research and development of materials

systems and device design. For example, the research and development efforts of corporations such as INTEL, inc. has led to a 2^7 increase in the computational power and speed of the silicon based integrated circuit (IC) in the last 30 years. However, many of the current base materials currently employed in device structures do not present likely pathways to the realization of many next generation devices. In particular, applications such as ultra high speed (terahertz) switching, radiation hardened and/or high temperature operation, optoelectronic devices and magneto-optical devices cannot be met with the current semiconductor base-materials that are currently in commercial development

Currently developed materials systems provide an adequate basis for many applications in the realm of electronics, opto-electronics and the development of spintronic devices. For example the group-IV semiconductor Si has proven to be an excellent base material system for microelectronic integrated circuit (IC) applications. In addition, several optoelectronic applications have been realized using II-VI and III-V compound semiconductors such as ZnS and GaAs. Recently, spintronic devices have been created in the laboratory setting using the group II-VI semiconductor GaMnAs. However, these results are limited to temperatures below 100K.[1] Recently, Group III-nitrides such as GaMnN have been developed for room temperature spintronic applications.

While there has been considerable success in developing individual material systems for use as basis materials in electronics, opto-electronics and spintronics, no single material system has been sufficiently developed to offer a complete solution for all applications. Rather, as shown in Table 1.1, basis materials for specific applications have

focused on the material system which present the greatest advantages and least difficulties. For group IV, III-V and II-VI materials systems, there exist fundamental materials issues which prevent application across the spectrum of applications. A brief survey of these limitations is offered in the following discussion.

As shown in Table 1.1, the group III-nitride system has not yet been sufficiently developed for use in all of the potential device applications. However, it is one of the main material systems for which the associated challenges for future applications relate to process engineering rather than fundamental limitations. The effort to continue to development group III-nitrides is of crucial importance for the successful realization of these next generation applications.

	Current Applications			**Next Generation Applications**			
	Electronics	Opto-electronics	Spintronic	High Speed Switching	Opto-electronics	Harsh Conditions	Spintronic
IV	Prominent	Limited	NA	Limited	NA	NA	NA
II-V	Limited	Prominent	NA	NA	Limited	Limited	NA
III-V	Limited	Prominent	Limited	Limited	Prominent	Limited	Limited
III-N	NA	Prominent	NA	Promising	Promising	Promising	Promising

Table 1.1: Current and future applications for various semiconductor material systems. Note that while the group III-N system is currently prominent in optoelectronics only, it shows the most promise as a pathway to next generation applications.

1.2.1 High speed switching devices

The most readily apparent result from the development of devices based upon semiconductor materials has been the exponential growth of the computation power of the integrated circuit (IC). The Si-based IC represents the most mature of the semiconductor based microelectronic technologies. In addition, Si-based IC production also accounts for the greatest economic strength of the semiconductor industry, with a world wide market capitalization in excess of $180 billion (US)[2]. As Si represents the most concerted effort in the development of a single semiconductor material for device applications, a more careful treatment of its development, and limitations is warranted.

The exponential increase in the switching speeds of of Si-based CPUs has not been the result of research efforts aimed at one area, such as material quality. Rather, the current performance of Si-based devices is a result of research and development aimed at a wide variety of disciplines related to device manufacturing. For example, advances in the Czochralski growth method has enabled the production of Si substrates with 300mm diameters and intrinsic defect densities $\leq 10^{12}$ cm^{-3} which is well below the density of intentionally introduced defects (doping level) found in most device structures[3-5]. In addition, efforts aimed at the development of advanced junction devices such as the metal oxide semiconductor field effect transistor (MOSFET) has resulted in a dramatic improvement in device performance[6] .

There is, however, a physical limit to the maximum switching speeds for Si-based device structures. The switching speed of a transistor is primarily a function of the mobility of the basis material. The concentrated research and development efforts aimed at the Si material systems has led to the production of intrinsic Si layers with mobility values very close to the theoretical maximum[7,8], as shown in Figure 1.1a. This suggests that the advances in switching speeds required for next generation devices cannot be achieved by devices based upon Si. Several group III-V binary semiconductor materials, exhibit high mobility values, particularly GaAs (Figure 1.1b). While there has not been as much development of these systems, partly due to the ability of Si based systems to meet current needs, recent efforts have resulted in GaAs-based PIN transistors with operational frequencies in the 60-80 GHz range[9].

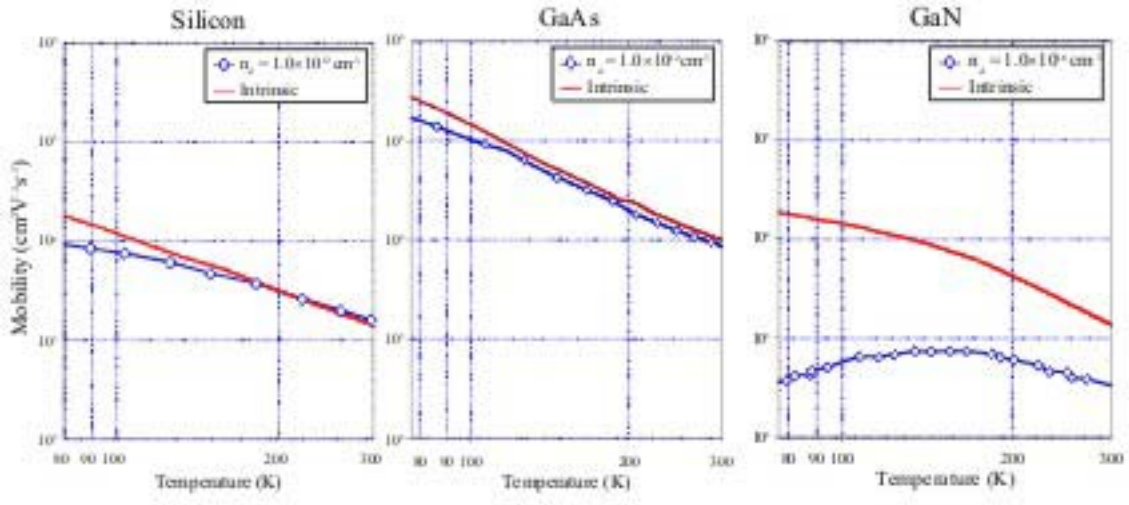

Figure 1.1: Mobility for **(a)** Silicon, **(b)** GaAs and **(c)** GaN

In spite of these fundamental base material limitations, there has been success in drastically improving the speed of Si-based *devices,* particularly in integrated circuit devices used for central processing units (CPUs). These efforts have focused on increasing the effective speed of devices by increasing the population of individual transistor devices on a single IC. Gordon Moore, the co-founder of INTEL corporation, stated that the transistor population of an IC would double approximately every 2 years. This statement has become commonly known as "Moore's Law". As shown in Figure 1.2a, transistor population in high performance Si-based ICs manufactured by INTEL corporation does, in fact, closely follows "Moore's Law."[10]

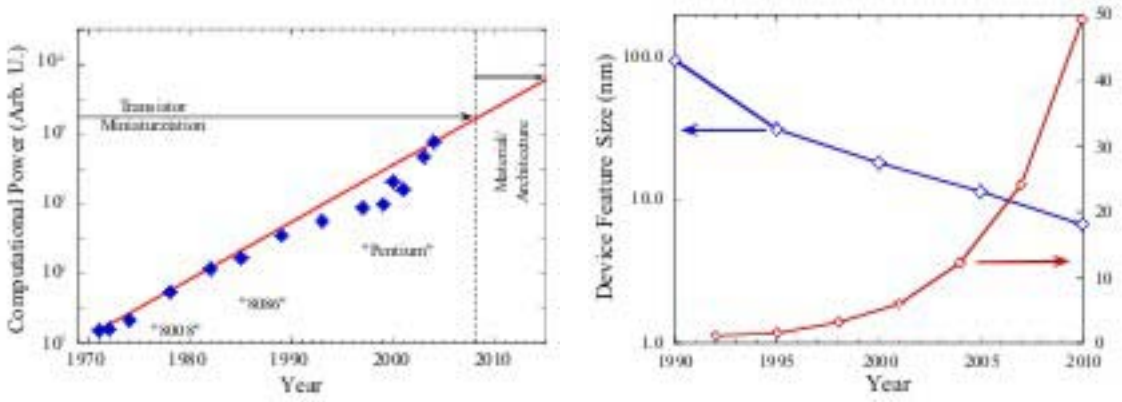

Figure 1.2(a): Transistor population on Si-based ICs manufactured by INTEL corporation, which closely follows "Moore's Law". Labeled processor models represent major improvement in performance. (**b)** Device feature size and fabrication plant cost as a function of time. It should be noted that for the year 2010, the cost of a fabrication plant will be approximately 10% of the total market capitalization

While increasing the transistor population in a given IC does result in an increase in the effective speed of the device, there are serious concerns that the design limit for Si-based IC devices is approaching[11]. In order to maintain the trend in performance improvement through an increase in the transistor population, the physical dimensions of each individual device feature must get smaller, as shown in Figure 1.2(b). The processing of ICs with these feature size requirements presents many challenges. On the fundamental level, as channel lengths are scaled into the nanometer range, the electrical barriers of CMOS device structures begin to degrade due to thermal carrier generation and quantum mechanical tunneling[12]. The lithographic imaging for next generation devices now requires highly stabile extreme ultraviolet (EUV) light sources operating in the sub 65nm or even 10nm wavelength regions[13]. Ultra-clean room conditions must be maintained in order to prevent accidental contamination which will destroy processor performance. These and other factors have caused a sharp rise in the cost of a IC fabrication plant construction and operation, also shown in Figure 1.2(b). It is predicted that by 2010, the cost of a new fabrication plant capable of producing Si-based ICs with performance improvements matching the predictions of "Moore's law" will fall between $30 and $50 billion (US)[14]. This cost is projected to be approximately 10% of the world wide market capitalization for all Si-based ICs. So, it can be seen that the pathway of increased transistor population is reaching a critical point, at which the required economic expenditures are no longer justified by increase device speed.

1.2.2 Opto-Electronic Devices

Next generation opto-electronic applications such high efficient energy conversion and terahertz optical communication systems cannot be met by current semiconductor material systems. While great progress has been made in the development of several materials systems, physical limits have hindered development of devices for these much needed applications. While Si based devices have shown great applicability to electronic applications, they are not suited for opto-electronics for several reasons. First, the 1.15 eV band gap energy of Si corresponds to an emission wavelength of 1078 nm, well beyond the visible range[15]. In addition, this band gap transition is indirect, requiring phonon-photon coupling which greatly reduces the maximum efficiency.

Many binary compound semiconductor systems have been developed for opto-electronic device structures. Figures 1.3(a) and 1.3(b) show the band gap energy, optical absorption/emission wavelength and lattice constants for binary semiconductor systems in the group III-V and group II-VI material systems. While the range of band gap energies spanned by these material systems allow effective spectral tuning, there are many associated difficulties. Due to the effects of internal strain on a semi-conductor, the growth of high quality material systems with a lattice mismatch of more than 2% is very difficult and requires special processing conditions. As a result, many combinations of binary systems are impossible or extremely difficult and expensive to produce. The large number of constituent elements in these material systems require the use of many

precursor solutions during growth resulting in different, often incompatible processing parameters.

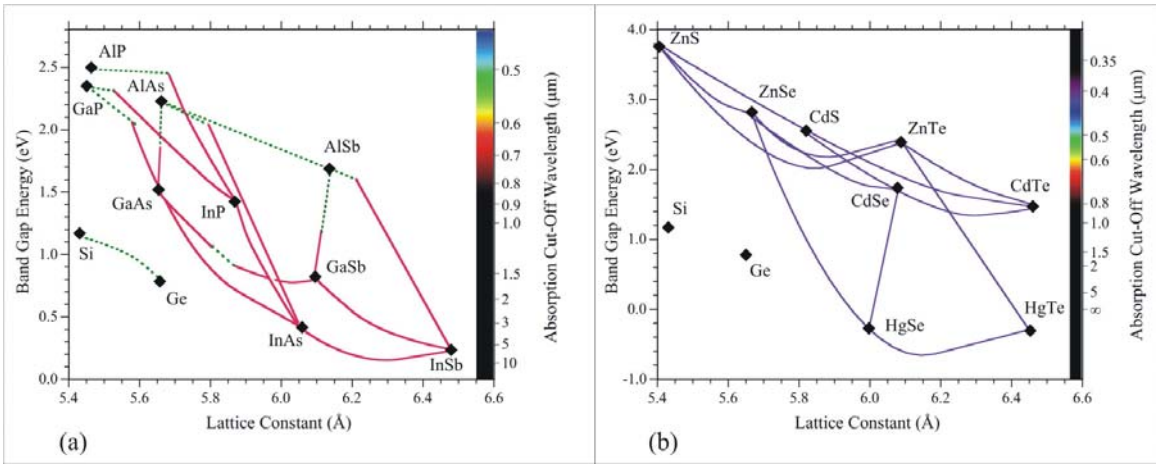

Figure 1.3. (**a**): Band gap energy and optical absorption wavelength values for group III-V semiconductor material systems. (**b**) Band gap energy and optical absorption wavelength values for group II-VI semiconductor material systems. Note the wide range of constituent materials and lattice constants which limit the growth of these material systems for applications in opto-electronics materials.

Group III-N based opto-electronic materials show great promise for meeting the needs of next generation applications. As shown in Figure 1.4, the group III-Nitride material system spans a wide range of band gap energies which correspond to optical emission from the near infrared to deep ultraviolet. In addition, the band gap of the Group III-N system is direct, leading to high quantum efficiency and faster switching speeds. It

should be noted, however, that there are still many difficulties in producing high quality group III-N material, which is discussed in detail in Chapter 2.

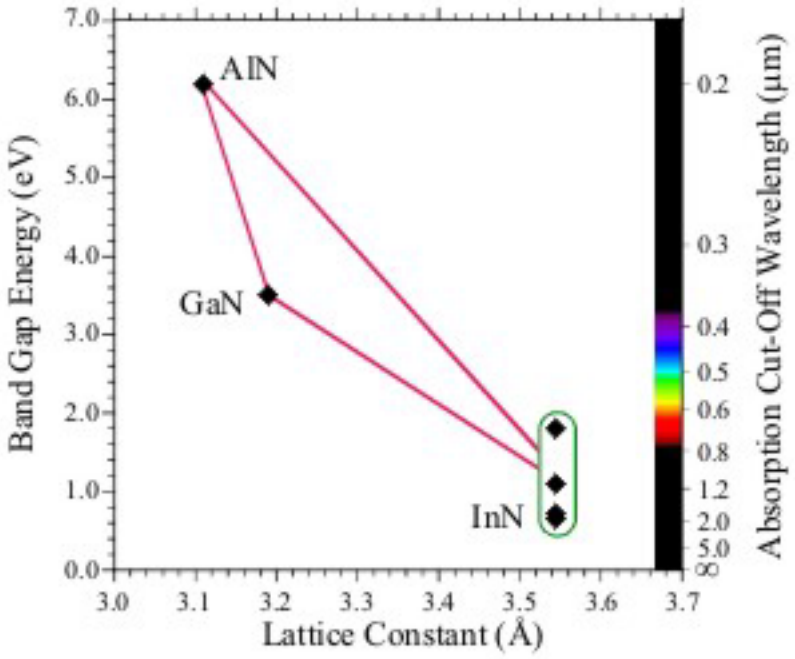

Figure 1.4: Band Gap Energy vs. Lattice Constant for binary Group III–N Semiconductor Materials. Lines indicate band gap energy for varying composition between constituent end points**.**

1.2.3 Devices operating under extra-normal conditions

There is a great need next generation device structures capable of operating in high radiation/ambient temperature environments and at high power, which current semiconductor material systems are incapable of achieving. Many crucial industrial, scientific and military applications of microelectronic and opto-electronic devices depend upon this capability. In this section, a brief overview of the physical limitations of current semiconductor technology with respect to these extra normal applications is presented.

The primary mechanism limiting the operation of devices in a high radiation environment is the formation of electron-hole pairs. As shown in Figure 1.5, high band gap materials such as SiC and GaN exhibit a high electron-hole activation energy[16]. This increased activation energy allows these high band gap semiconductors to operate in high radiation fluxes compared to low band gap structures such as Si and GaAs. As the energy gap associated with the formation of defects in a high radiation environment falls far from the wide band gap of GaN, this material system is particularly promising for developing devices which operate in high radiation fluxes. Development of group III-N device structures will be greatly helpful for next generation space based applications in that the effects of radiation induced defects would be limited. As the threshold radiation dosage for failure of current CMOS technology depends primarily on the square of the oxide thickness, developers of space based electronics have been forced to rely on outdated 8086-based ICs in which the wide channel width allows increased operational lifetimes in high radiation environments[17].

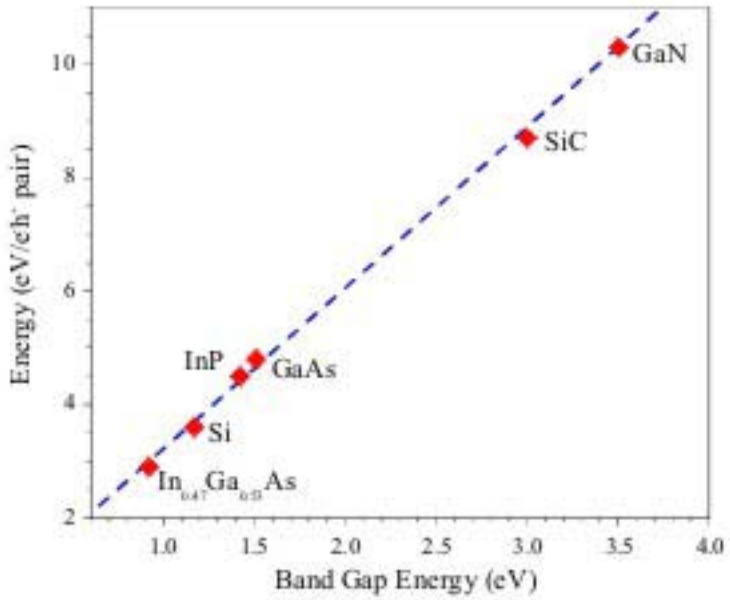

Figure 1.5: Ionization energy for selected semiconductor material systems. The line serves as a guide to the eye

The functional operation of current Si-based technology above 150°C is extremely limited, requiring external cooling or remote location of sensitive equipment[18]. While some high temperature applications can be successfully addressed by bulk Si and silicon on insulator (SOI) technology, these materials do not function in ambient temperatures above 300°C. Therefore applications such as high temperature monitoring, in-situ combustive and industrial control cannot be achieved. The current state and probable future technological response to several high temperature applications are summarized in Table 1.2.

Application	Peak Ambient Temp (°C)	Current Technology	Future Technology
Automotive			
Engine	150	Si/SOI	WBG
Exhaust	600	NA	WBG
Jet Turbine			
Control	300	Si/SOI	WBG
Actuation	600	NA	WBG
SpaceCraft			
Power	150	Si/SOI	WBG
Venus/Mercury Exploration	550	NA	WBG
Industrial Processing	600	NA	WBG

Table 1.2: Ambient Temperature environments for several microelectronic applications. Not that no technology is not currently available for many applications. [18].

The fundamental physical mechanism which limits the operation of a semiconductor device in a high temperature environment is the thermal generation of free carriers. If one considers Si-based devices, the minimum intentional doping concentration is typically between 10^{14} to 10^{17} cm^{-3}. Thermal energy from a high temperature ambient generates an additional intrinsic free carrier density which can be expressed as

$$n_i = \sqrt{N_C N_V}\, e^{-E_g / 2kT},$$

where E_g is the fundamental band gap energy, k is the Boltzman constant, T is the ambient temperature, and N_C and N_V are the effective electron and hole densities, respectively. As shown in Figure 1.6, the lower intrinsic thermal carrier concentration of wide band gap materials such as SiC and GaN results in a significant reduction in the

thermally generated intrinsic carrier concentration. Wide band gap voltage rectifiers composed of SiC have recently been demonstrated with ambient operating temperatures of 600°C[18].

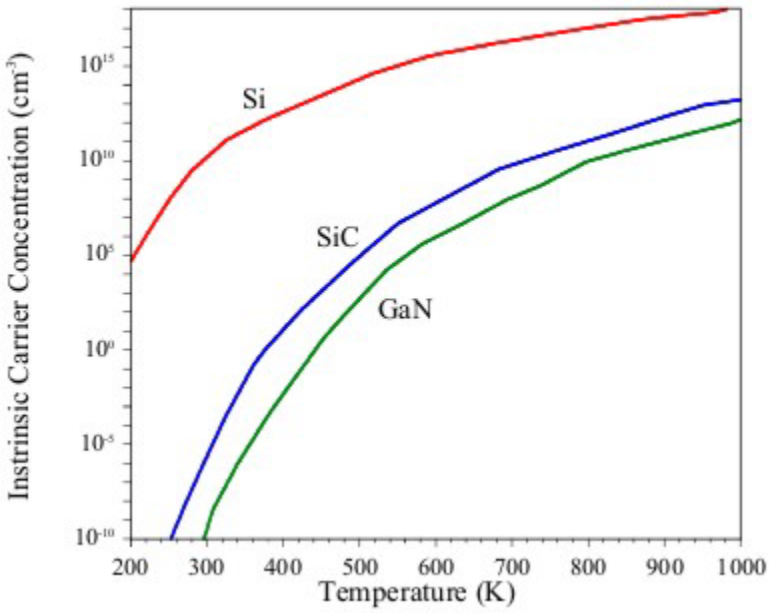

Figure 1.6: Intrinsic carrier concentration for Si, 6H-SiC and 2H-GaN. Note that the wide band gap of SiC and GaN allow for greatly reduced n_i at elevated temperatures.

As in the case of high frequency switching applications, the currently available technology for high power applications is beginning to reach the maximum theoretical performance. Overcoming this power limitation is crucial for the realization of next generation applications where power management is key to functionality, such as electric

powered automotive applications, industrial control systems and fuel cell power generation. Si based device structures offer a pathway to achieve high power applications, but at significantly increased technological challenge and production cost.

Of primary concern in the design of a high power semiconductor device structure is the breakdown voltage of the diode channel. Improvements can be achieved by increasing the area of the device channel, but this presents significant cost disadvantages. In addition, the increased channel area presents fundamental limits on the maximum operating speed of the device, forcing designers to choose between high speed/high power devices. Of added concern is the internal heat generation that comes from transient high current/high voltage conditions during switching. This dynamic power dissipation can become so significant that device operation is compromised.

1.3 Conclusion

The need for advanced materials systems and advanced next generation semiconductor devices has been outlined in this chapter. High speed optoelectrics, high efficiency energy conversion, ultra high speed switching and high power/radiation hardened devices require material parameters that current Si-based and conventional group III-V materials are incapable of meeting. In addition, the need to have an *integrated* device capable of all of the above applications dictates that new material systems be investigated. While many material systems are capable of meeting one individual requirement, the most promising pathway to the realization of all these capabilities lies with the group III-nitride material system. In the following chapter, the current status and limitations of the group III-nitride

material system are outlined. As the development of these materials has been closely focused on GaN, emphasis will be placed on this material system, with a brief outline of the challenges presented by the InN and In-rich $Ga_xIn_{1-x}N$ material system.

2. Group III-Nitrides

2.1 Introduction

The last decade has seen profound excitement from and efforts aimed toward the research and development of devices based up the group III-nitride material systems[19-22]. As outlined in the previous chapter, there are many next generation applications for which currently existing Si-based and conventional group III-V and group II-VI materials systems are not well suited. Group III-Nitride materials show great promise for the development of device structures for short wavelength light emission which can be used in full color displays, high density optical information storage media and blue laser diode structures[23]. In addition, high temperature and high power transistors for turbine engine sensors, all-electric automotive technology and chemical sensing in corrosive environments can be realized with group III-N material systems. The direct band gap values of GaN, AlN and InN are 3.4eV, 6.9eV and 1.9eV, respectively, which enables the production of $Ga_{1-x-y}In_xAl_yN$ alloys which completely span the visible radiation spectrum[15]. In addition, the extremely high mobility of the group III-N nitride system, as shown in Figure 2.1, indicates that it will be an excellent material system for high speed switching devices. While the current development of group III-N materials has been dominated by GaN, alloys of AlGaN, InGaN and AlGaInN are becoming increasingly prevalent.

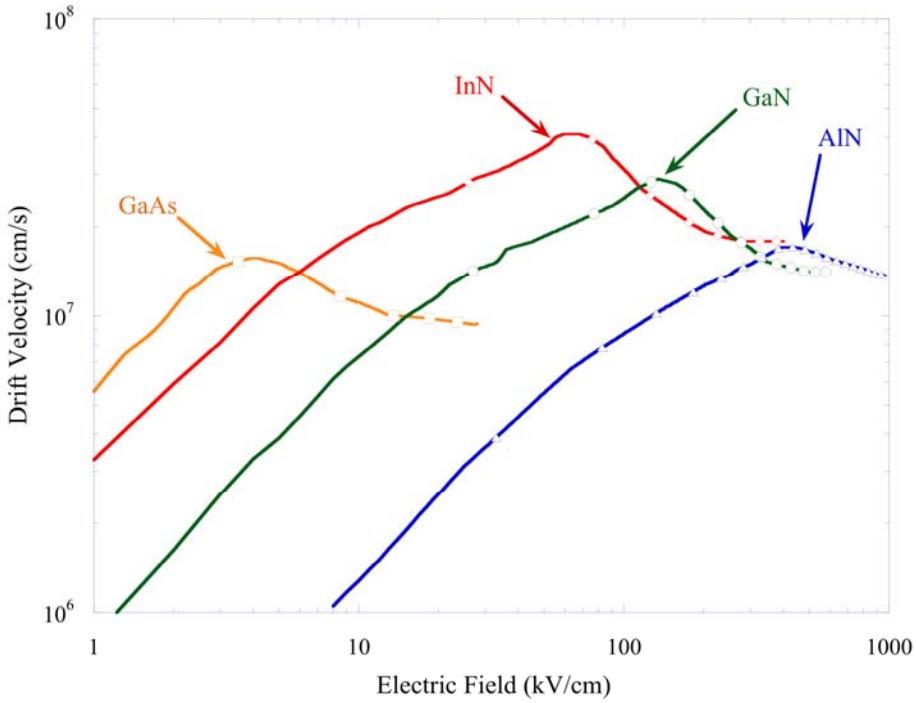

Figure 2.1: Drift velocity of group III-N materials and GaAs. Note the maximum drift velocity of InN is approximately 5x that of GaAs. In addition, group III-N materials exhibit very high field strengths[24,25].

This chapter deals briefly with the current technological state of the group III-N material system. Emphasis is placed on current growth methods and the resultant optical, electrical and structural characteristics. Special emphasis is placed on the InN material system and the current debate regarding the inherent properties of InN such as band gap energy.

2.2 Growth of group III-nitride materials

2.2.1 Historical perspective

Group III-N materials have been studied since the late 1930s when Juza and Hahn attempted to synthesize needles of GaN by passing NH_3 over high temperature Ga[26]. This experiment was repeated by Grimmeiss *et al.* in 1959 and produced small crystals of GaN[27]. The first successful growth of GaN on sapphire was achieved by Maruska and Tietjen in 1969 via chemical vapor deposition[28]. Research efforts on the group III-N material system intensified in the 1980s.. Yoshida *et al*. produced the first high quality GaN layers using a two step process (outlined below) of GaN on AlN buffer layers[29]. However, defect concentrations greater than 10^{10} cm^{-2} have persisted.

The 1990s saw prodigious effort and success in the development of group III-nitrides. Akasaki *et al.* developed p-n junctions from GaN and Nakamura developed high brightness blue LED structures[30]. This work was culminated with Akasaki *et al.* announcing the fabrication of a 376 nm laser diode based upon the GaN material system[31]. This represented the shortest wavelength injection laser developed to that date.

Even with this success and effort, there remains much work required to develop the group III-N material system. Defect densities remain very high in the group III-nitride material system, and require special processing techniques to overcome, as outlined below. While the associated energies of these defect densities are small compared to the fundamental band gap energy of GaN and AlN, they may play a crucial role in the

development of InN based device structures. The following sections outline the current state of technology as it pertains to the growth of group III-nitride materials.

2.2.2 Current Methods used for growth

Given the excitement and promise of the group III-nitride material system and extremely large numbers of scientific publications pertaining to the growth of these materials, it is reasonable to assume that many different growth methods have been applied to group III-nitrides. While this chapter will focus on organo-metallic chemical vapor deposition, molecular beam epitaxy and a few variations on these techniques, there are basic considerations for the growth of group III nitrides that must be considered, regardless of the growth technique employed.

2.2.3 Organometallic growth of GaN and related allows

By far, the most commercially viable method for the large scale production of semiconductor materials is organometallic chemical vapor deposition (also refered to as metal-organic chemical vapor deposition, vapor phase epitaxy or metal organic vapor phase epitaxy). OMCVD offers advantages over other growth methods in the areas of cost, coating uniformity, short maintenance cycles, flexibility in precursor selection and a wide range of processing conditions. For this reason, most efforts in the production of the group III-nitride GaN, AlN, and the $Ga_xAl_{1-x}N$ alloy system have focused on OMCVD. However, there are difficulties in the OMCVD production of high quality, indium rich $Ga_xIn_{1-x}N$ alloys, which will be discussed later in this chapter. This section will deal

briefly with the current state of OMCVD technology as it pertains to the production of commercially viable group III-nitride materials. As most efforts have been aimed toward GaN based devices, special emphasis will be placed on this material system.

2.2.3.1 Substrates and Chemical Precursors

A primary requirement for the epitaxy of any material system is the availability of an appropriate substrate. While high quality, lattice matched substrates are readily available for Si, GaAs and Ge, there does not exist high quality bulk group III-N substrates which has limited the development of low defect density group III-N thin films. Currently, the growth of group III-N thin films occurs predominately on sapphire and 6H-SiC substrates[19]. As shown in Figure 2.2, these substrates are not closely matched to the entire group III-N material system, requiring special growth techniques to alleviate strain and reduce intrinsic defect densities. While SiC does offer a closer lattice match to GaN and AlN, its commercial development as a substrate material has been limited by high economic cost and high screw dislocation densities (micropiping). As a result, sapphire, which is available at relatively low cost and high quality, has become the preferred substrate choice for the epitaxy of group III-N materials. It should be noted, however, that several very successful device structures are based upon the GaN/SiC material system.

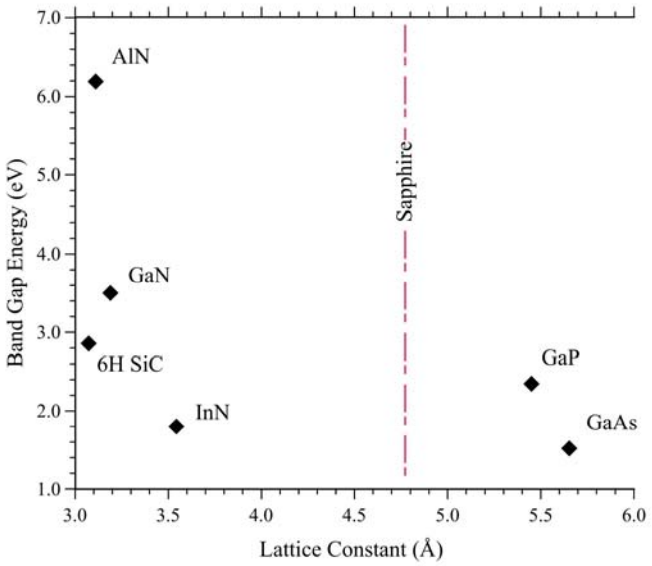

Figure 2.2: Band gap energy of several group III-V semiconductor material systems. Note that the substrate materials sapphire and 6H-SiC do not provide a close lattice match to all elements of the material system.

In addition to SiC and sapphire substrates, much effort has been aimed at the growth of group III-nitrides on Si substrates[32,33]. While there is a significant lattice mismatch between Si and all the group III-nitrides (see Figures 1.3(a), 1.3(b) and 1.4), the potential rewards of successfully implementing such a material system are understandable. The ability to vertically integrate optically active group III-nitride device structures onto existing chip technology would offer pathways to greatly enhanced processing speeds[34]. However, current efforts have yielded disappointing results. Group III-nitrides grown on Si substrates are of poor quality, with mixed phases and large defect densities.

The chemical precursors utilized during the growth of group III-nitrides via OMCVD are well established. The group III elements Al, Ga and In are most often supplied by trimethylaluminium (TMAl), Trimethylgallium (TMG) and Trimethylindium, respectively. These organometallic precursor gases are diluted into carrier gases, most often Hydrogen or N_2, for delivery to the reactor chamber. As these chemical precursors begin to decompose at approximately 450 °C, sufficient cracking of the precursors occurs at processing temperatures. Atomic N is most often supplied by ammonia (NH_3) for OMCVD growth. While NH_3 does not decompose as readily as the organometallic precursors (see Chapter 5), sufficient cracking does occur at growth temperatures. Hydrazine is sometimes used as a N source, especially when reduced growth temperatures are required.

2.2.3.2 **Growth Methodology**

In order to grow group III-N on sapphire via OMCVD, a modified two step epitaxial approach is utilized, first proposed by Yoshida *et* al[29](Figure 2.3). First an AlN or GaN buffer layer is deposited at low temperatures, followed by an increase in temperature and annealing step. Finally, GaN is deposited at optimal growth temperatures.

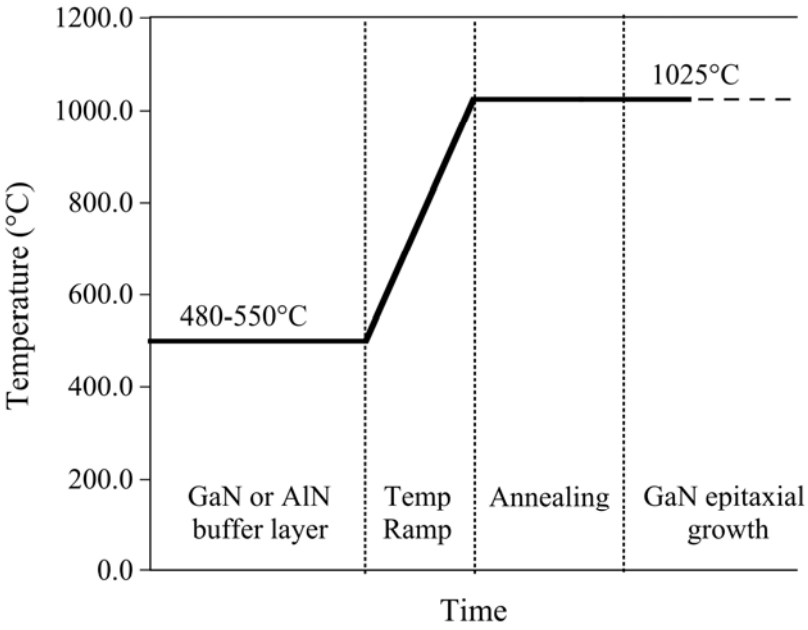

Figure 2.3: Typical two step technique for the epitaxial growth of GaN on sapphire by OMCVD.

Elaborate methods have been developed to overcome the lattice mismatch in substrate materials. For example, success in lowering the defect densities has been achieved using epitaxial laterally overgrowth substrates (ELOG)[32,35,36]. As shown in Figure 2.4, ELOG is achieved via the deposition of a SiO_2 mask on a GaN thin film. GaN is subsequently grown laterally on the windows. After approximately 10 μm of GaN overgrowth occurs, the stripes coalesce and a continuous 2D GaN layer is produced. This technique has been successful in producing GaN thin films with dislocation densities of approximately $2x10^{-7}$ cm^{-2}. While the ELOG growth method is capable of producing GaN layers with very low defect densities, it does have limitations. As any device

requires low defect densities throughout the entire area, the size of a device produced by this method is limited to the width of the SiO_2 stripes. In addition, extreme care must be taken in the alignment of the SiO_2 masks to ensure proper device structures, which greatly increases the associated cost of producing such materials.

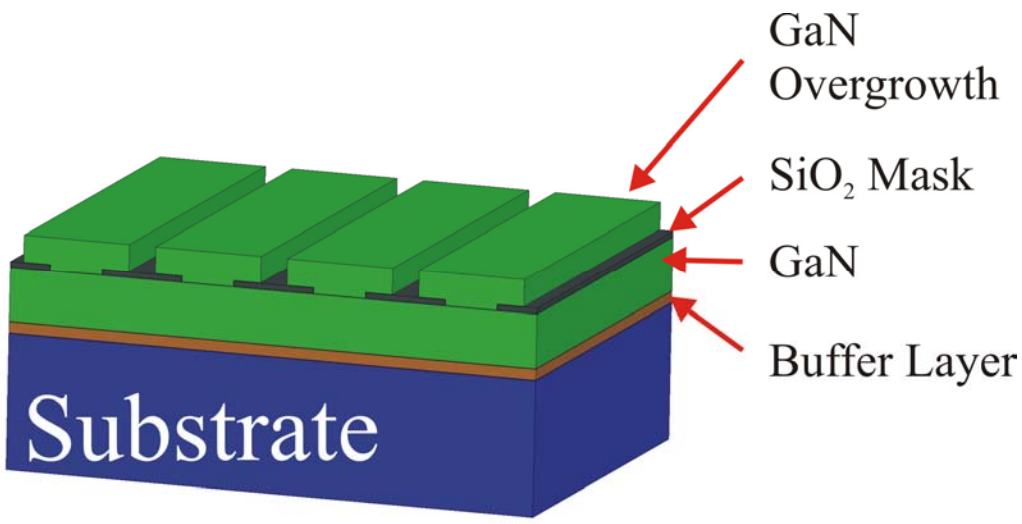

Figure 2.4: Basic design of and ELOG substrate. GaN is grown laterally on the SiO_2 mask, which relieves internal strain and lowers dislocation densities.

Another modified OMCVD approach to the production of high quality GaN and related alloys has focused on a pendeoepitxy (PE) approach[37-42]. In the PE method, a thin GaN layer less than the critical thickness is deposited on an AlN buffer layer. This layer is then etched and masked with SiN_x. Subsequent growth is initiated on the *sides* of the GaN columns, which eventually meet, and begin two-dimensional vertical growth. As no

nucleation is occurring on the substrate, areas of GaN with low defect densities can be produced. This PE process is shown schematically in Figure 2.5.

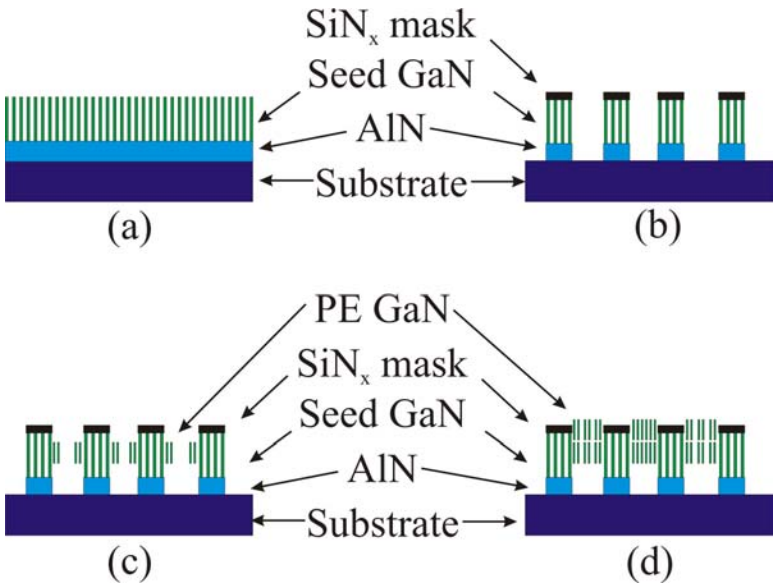

Figure 2.5: Pendeoeptixay of GaN via OMCVD process in which the following steps are used: (a) a GaN seed layer of thickness < $t_{critical}$ is deposited on an AlN buffer layer, (b) etching of GaN in to columns, (c) partial growth of PE GaN on the columns and (d) coalescing of the PE GaN.

2.2.4 Molecular Beam Epitaxy

While the growth of group III-nitrides, particularly GaN, is dominated by OMCVD techniques, there has been significant research into the epitaxy of group III-nitrides via molecular beam epitaxy (MBE)[43-46]. There have been several difficulties unique to the MBE growth environment that have hindered its prevalence as a growth technique, which are discussed below. In addition, the associated costs, maintenance

cycles and low growth rate associated with MBE have prevented it from being a commercially viable method for the industrial production of group III-N materials.

2.2.4.1 Substrates and precursors for MBE growth of group III-nitrides

As in OMVCD, the preferred substrates for the growth of group III-nitrides in MBE are 6H-SiC and sapphire. While MBE occurs at much lower pressures than conventional OMCVD, both of these substrates offer sufficient thermal stability to withstand elevated temperatures at low pressures. However, there does exist a major limitation in substrate selection for MBE. As MBE utilizes ballistic beams of atomic precursors, the use of patterned substrates such as those used in ELOG and PE is limited due to shielding. In addition, the low pressure environment also limits the use of preprocessed substrates to those whose constituent materials possess very low thermal decomposition pressures.

One of the most serious limitations in the growth of group III-nitrides via MBE is the reduced processing temperatures required to ensure stable thin films. As shown in Figure 2.6, the thermal stability of group III-nitrides is greatly reduced at low pressures[47,48]. In fact, it is this thermal stability issue that has served as the major motivation for this work. As MBE growth techniques are performed at reduced temperatures (usually ≤ 800°C) the thermal decomposition efficiency for ammonia is greatly reduced, leading to low growth gates of approximately 0.4 μm/h. Recently growth rates of approximated 1-2 μm/h have been achieved at 750-850°C for GaN via

OMCVD[44]. However, these growth temperatures are incompatible for high In content $In_xGa_{1-x}N$ alloys, as discussed in detail throughout this work.

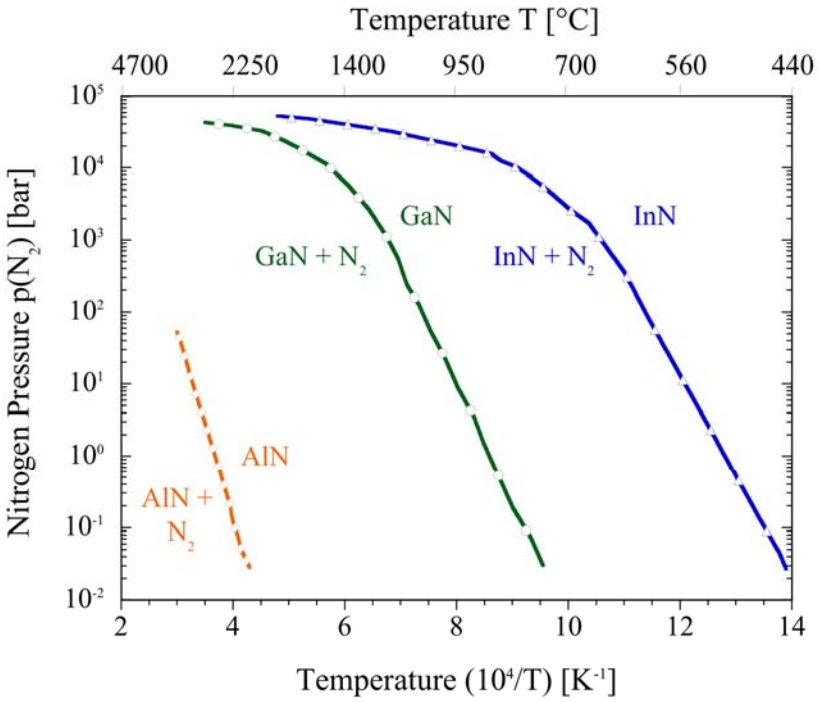

Figure 2.6: Thermal Stability of group III-nitrides under N_2 background pressure. Note that for nitrogen pressures below 10^{-2} bar, GaN becomes unstable at approximately 750°C which is well below the optimal processing temperature for OMCVD growth.

2.3 Challenges of In rich materials

The development of InN materials has closely followed that of GaN, in that the ternary allow GaInN is extremely important for many device applications. However, due to reasons elaborated below, the In content of these devices has been very low, typically below 10%. Even at these low compositions, the addition of In to GaN semiconductor material systems has had a remarkable effect on the development of advanced devices. It has been shown that very small additions of In to the active region of GaN LED

structures greatly increase the emission efficiency. Also, the $Ga_xIn_{1-x}N$ alloy system has enabled the development of high efficiency LED structures operating in the green wavelength region.

While great effort has been expended on the study of InN, there remains fundamental questions regarding the basic materials properties of InN, such as the band gap energy, lattice spacing and effect of defect structures on electrical properties. As outlined in the following sections, several fundamental questions remain whose solutions require unique growth methods.

2.3.1 Historical Perspective

The initial attempt to produce InN was made by Juza *et al*. in 1938[26] using $InF_6(NH_4)_3$ which resulted in the first report of its wurtzite crystal structure. Several additional attempts were made[49,50]. McChensey *et al*. (whose paper provides the motivation for this work) reported the high dissociation pressure of InN[48]. Hovel and Cuomo produced polycrystalline InN on silicon substrates in 1972[51]. Marasina *et al.* utilized chemical vapor deposition to produce epitaxial layers of InN with electron concentrations of approximately $2x10^{20}$ cm^{-3} [52]. The initial growth of InN by OMCVD was developed by Matsuoka, *et al.* and Wakahara *et al*. in 1989[53,54].

2.3.2 Growth Techniques for producing InN and In rich alloys

The growth of InN via traditional OMCVD techniques has proved difficult and has not yielded high quality InN. This is due primarily to the low processing temperatures

required to prevent the decomposition of InN at the surface, as shown in Figure 2.5. These low processing temperatures result in very poor cracking of the NH_3 which is the preferred N precursor. It has been shown that increasing the processing temperature leads to improved NH_3 decomposition, but also increases the thermal etching of the InN thin film. Hybridized OMCVD methods such as Laser enhanced OMCVD have yielded some positive results. However, the fundamental limitation of low processing temperatures associated with the reduced pressure environments remains.

This low processing temperature for InN is even more pronounced in MBE growth conditions. While MBE has been successful in producing InN of high crystalline quality, the processing temperatures have been limited to ≤ 450 °C. This low processing temperature has yielded InN thin films with increasing low band gap energies, as discussed in detail in the following chapters.

3. High pressure organometallic chemical vapor deposition reactor

3.1. Introduction

This chapter outlines the design of a high-pressure chemical vapor deposition (HPCVD) system with integrated real-time optical monitoring capabilities[55-57]. The objective of this system is the real-time evaluation of the growth kinetics of nucleation and coalescence of heteroepitaxial thin films, which is an important step of chemical vapor deposition since it defines the perfection of the heteroepitaxial film both in terms of extended defect formation and chemical integrity of the interface. Presently, most growth efforts focus on low pressure processing to minimize the influence of flow dynamics on process uniformity and favors organometallic chemical vapor deposition (OMCVD) for III-V compounds. However, the extension to above atmospheric pressures is necessary for retaining stoichiometric single phase surface composition for materials that are characterized by large thermal decomposition pressures at optimum processing temperatures. For example, $Ga_xIn_{1-x}N$ heterostructures have been identified as an important basis for manufacturing optoelectronic and microelectronic devices, such as light sources, detectors and high power microwave devices for which large potential markets can be identified. Due to the high thermal decomposition pressure of InN, these devices are at present limited to gallium-rich compositions. High nitrogen pressure has been demonstrated to suppress thermal decomposition of InN, but has not been applied yet in chemical vapor deposition or etching experiments. Because of the difficulty with maintaining stoichiometry at elevated temperature, current knowledge regarding

thermodynamic data for InN, e.g., its melting point, temperature-dependent heat capacity, heat and entropy of formation are known with far less accuracy than for InP, InAs and InSb. Gaining access to these data will require the development of new real-time optical diagnostics to obtain sufficiently accurate data on flow conditions, gas phase reactions and surface reaction kinetics to support modeling and simulations of thin film growth under laminar and/or turbulent flow conditions at sup-atmospheric pressure.

This chapter focuses on the base material InN and addresses both: (a) the prediction and simulation of gas phase reactions and surface kinetics of InN growth at high pressures (up to 100 bar) and (b) real-time optical monitoring of gas phase- and surface chemistry processes during high pressure chemical vapor deposition (CVD) of InN. Modeling and simulations of gas phase and surface reactions kinetics for InN growth at high pressures are presented, which are based on a numerical solution of nonlinear, coupled partial differential equations representing the conservation of momentum, energy and total mass as well as balances over the individual species involved in the InN deposition. The operating conditions modeled correspond to flow dominated by forced convection where $Gr << Re^{2.}$. That is, the Grasshoph number is sufficiently small to be ignored. The capabilities of the implemented high-pressure CVD reactor and the real-time optical monitoring techniques available in this reactor are also presented .

3.2 High-pressure Reactor

The growth of III-nitrides under HPCVD conditions with integrated optical diagnostics requires a completely unique reactor design as well as new gas mixing and gas injection controls. Figure 3.1(a) depicts a side view of the assembled HPCVD reactor with flow direction from right to left. The flow control panel depicted in Figure 3.1(b) is fully computer interfaced and provides:

- the compression of the III- and V-gas sources ($\leq$ 100bar),
- the mixing of the gas sources and dilution of the gases in nitrogen carrier gas,
- the pulsed injection of all gas sources,
- the pressure control of the reactor in the pressure range of 1 to 100 bar.

The flow channel of HPCVD reactor has constant cross section from entrance to the exit with symmetric sapphire substrates arrangements in the upper and lower channel walls. Thus, the bifurcation of nutrient fluxes to the top and bottom channel walls is symmetric to the center-line. Thus well behaved flow and deposition can be expected in the targeted pressure range. Pressure test were performed up to 120 bar with flows from 10 standard liters per minute (slm) to 50 slm. In the next step we interfaced the reactor to the gas injection panel shown in Figure 3.1(b). The gas injection sequences are tested and optimized in timing and flows. An exact timing is not only important to avoid pressure fluctuations during the switching sequences, but also to synchronize the gas precursor injection with the optical monitoring techniques.

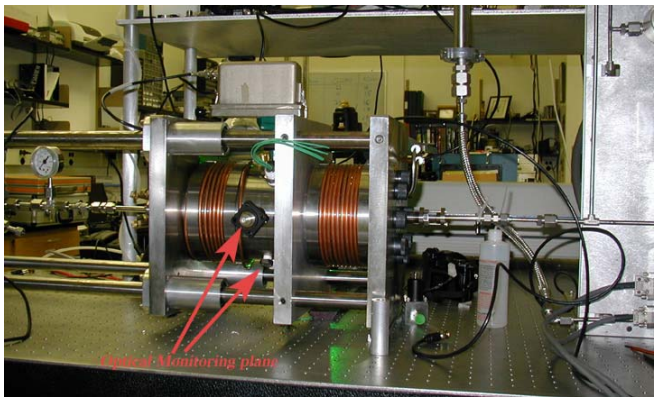

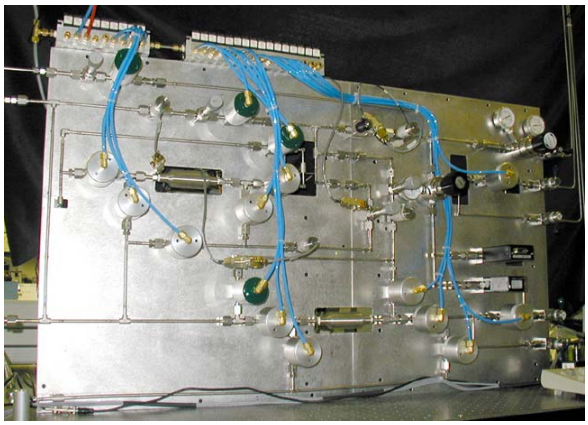

Figure 3.1(a): Side view of the completely assembled HPCVD reactor with gas injection from the right. The optical monitoring plane is in the center of the substrates. **Figure 3.1(b):** Flow control panel for precursor compression and pulsed precursor gas injection

For real-time gas flow dynamics studies as well as the analysis of the gas-phase decomposition kinetics during the thin film growth process, optical access ports are integrated in the reactor as schematically shown in Figure 3.2. The access ports allow the optical monitoring perpendicular to the flow direction at the center line of the two symmetric in the upper and lower channel walls inserted substrates. Two optical ports

provide access to the flow channel and allow the monitoring of gas flow and gas-phase decomposition kinetics. As depicted in Figure 3.3a, three ports in each half of the symmetric reactor provide access through the backside of the substrate to the growth surface and with it to the growth process itself. The optical rods are made of sapphire and index matched to the sapphire substrates. The rods are inserted through the outer reactor shell in to the inner shell and touch the substrates from the back. The pressure is retained by a double o-ring seal within the outer reactor shell. A protective cap on the outer side of the holder prevent the rod from moving outwards.

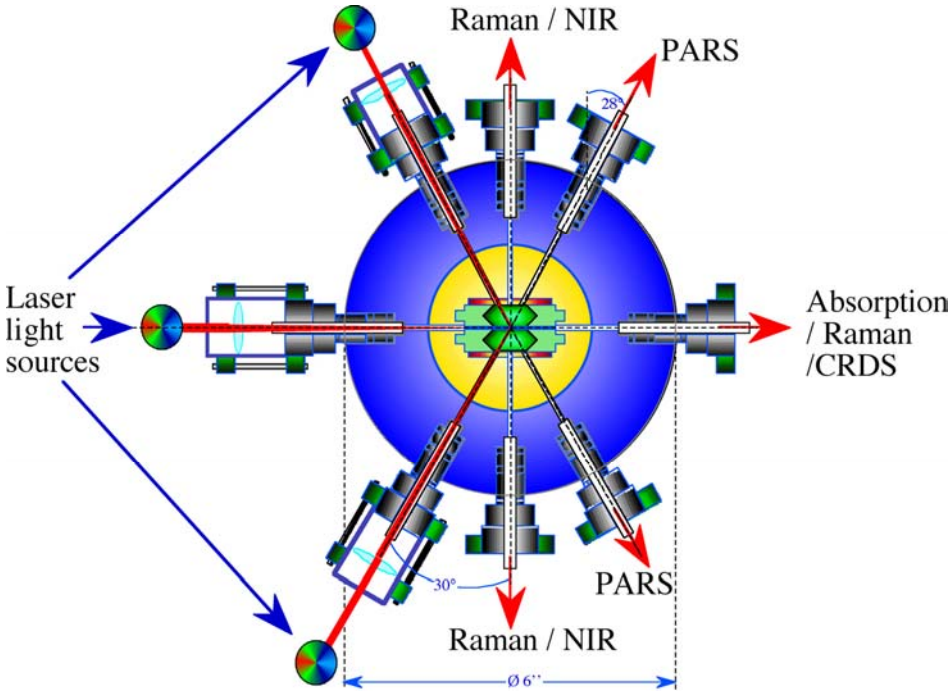

Figure 3.2: Cross Section of HPCVD reactor, which contains the integrated optical access ports. The cut is perpendicular to the flow channel.

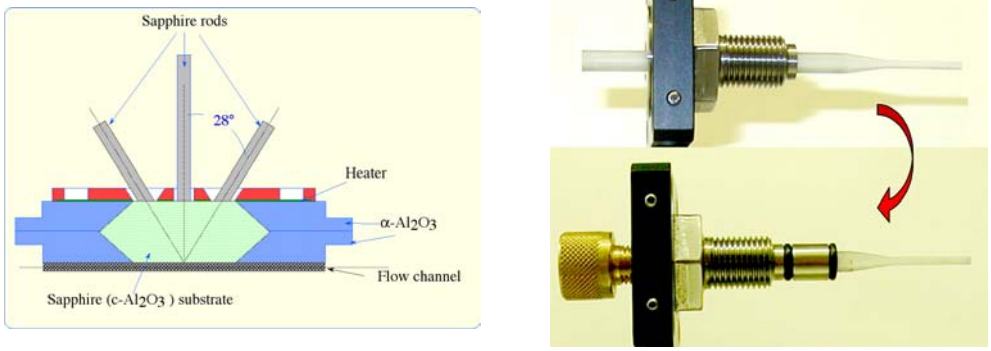

Figure 3.3(a): Optical access rods to monitor the growth process through the backside of the substrates. **Figure 3.3(b):** Double O-ring sealed sapphire rod assembly before inserting in reactor.

The optical real-time monitoring capabilities provide crucial experimental data needed as input parameters for process models and simulation codes as well as to establish growth parameter sets needed for analysis and control of chemical vapor deposition at elevated pressure. In the following sections, modeling and simulation efforts on gas phase and surface reactions kinetics for InN growth at high pressures are presented.

3.3 Modeling and Simulations

The HPCVD reactor simulations are based on a numerical solution of nonlinear, coupled partial differential equations representing the conservation of momentum, energy and total mass as well as balances over the individual species. The modeling equations

were solved using the finite volume element method based upon an integral form of the equations to be solved. The integration of the differential equations leads to a set of algebraic equations which are solved internally by the CFD-ACE(U) iterative, segregated solution method wherein the equation sets for each variable are solved sequentially and repeatedly until a converged solution is obtained. The operating conditions correspond to flow dominated by forced convection where $Gr << Re^2$.

The surface reaction mechanism for growth of InN has been described by a reduced-order model, noting that a larger number of possible reactions may have to be taken in to account[58-60]. The reduced order model is based on pulsed chemical vapor deposition, which substantially reduces the number of reacting species. A typically precursor injection sequence is depicted in Figure 3.4. The V/III ratio has to be chosen properly to assure the incorporation of In-atoms supplied to the surface into the InN lattice. The assumed surface reactions are summarized in Table 3.1. which is the adsorption of the reactive species that are present in the gas phase, with rate parameters given by Cardelino et al.[61]. The growth of InN from trimethylindium (TMI) and ammonia (NH_3) has been simulated based on the reduced-order model, with flow, heat and mass transfer in the HPCVD reactor evaluated for a symmetrical positioning of the substrate wafers.

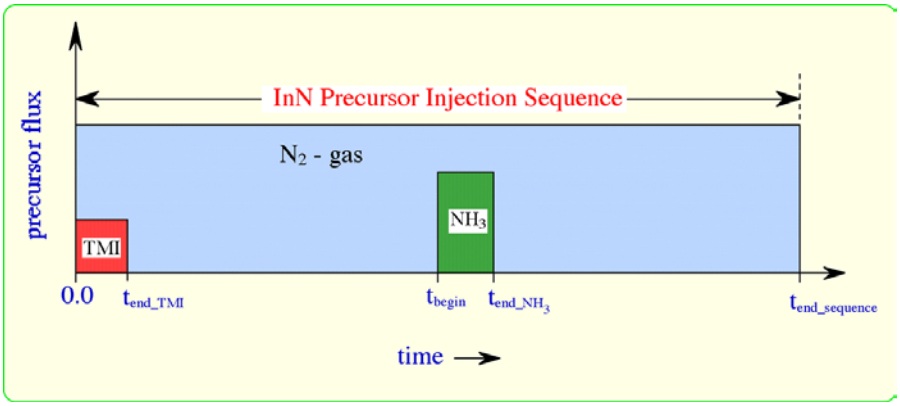

Figure 3.4: Schematic timing sequence for the precursor injection for InN growth

The gas phase reactions of TMI according to Table 3.1 were obtained in the pressure range of 10 to 100 atm as a function of substrate temperature and centerline flow velocity under steady-state conditions. The predicted gas phase reaction variations with centerline flow velocity for p = 100 atm and T_s= 900 K are depicted in Figure 3.5. The simulations show the vapor phase concentration of MMI at the gas - substrate interface with p = 100 atm, **u** = 12 slm and T_s = 900 K and with p = 10 atm, **u** = 60 slm and T_s = 900 K, in Figures 5a and 5b, respectively. A comparison shows that for **u** = 12 slm and p = 10 atm the maximum concentration of MMI is at the center of the substrate (see Figure 5a), whereas for **u** = 60 slm and p = 10 atm, the maximum concentration of MMI has shifted downstream. The simulations indicate that for higher centerline velocities the maximum concentration of MMI will shift downstream, which would prevent the maximum MMI flux to become adsorbed at the center of the substrate. When the flow rates increased to 120 slm at p = 10 atm and T_s = 900 K, the Re number equals 3000, which requires the use of the k-epsilon model to account for the effects of

turbulence.

Table 3.1. Reduced-Order Model: Pulsed TMI followed by Pulsed NH_3

Gas Phase Reactions:	$TMI(g) \rightarrow DMI(g) + CH_3$
	$DMI(g) \rightarrow MMI(g) + CH_3$
	$NH_3(g) + h\nu\ (170\text{-}220\ nm) \rightarrow NH(g) + H_2$
Surface Reactions:	$MMI(g) + S_1 \rightarrow MMI_{ad}$
	$NH(g)+MMI_{ad} \rightarrow (HN:MMI)_{ad} \rightarrow InN(s) + CH_4\uparrow$

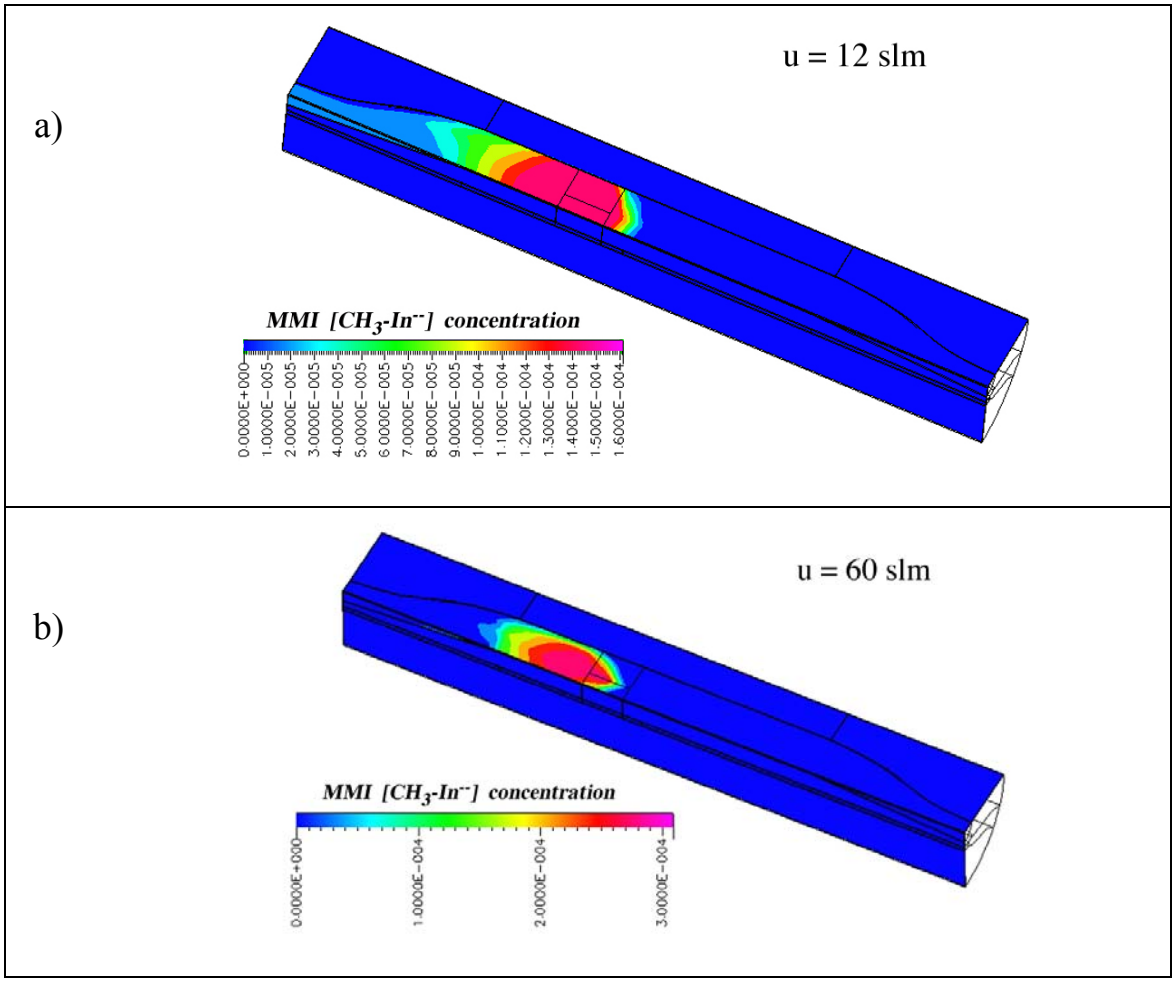

Figure 3.5: Effect of Centerline flow velocity for P = 100 atm and T_s= 900 K

At the optimum growth temperature of T_s = 900 K in the pressure range of 10 to 20 atm, the concentration of MMI and atomic indium is evenly distributed over the substrate surface as seen in Figures 3.6(a-d), respectively. The effect of the increasing pressure on the gas phase kinetics is summarized in Figure 3.7 for a substrate temperature

of 1000K and a centerline velocity u=12 slm.

a)

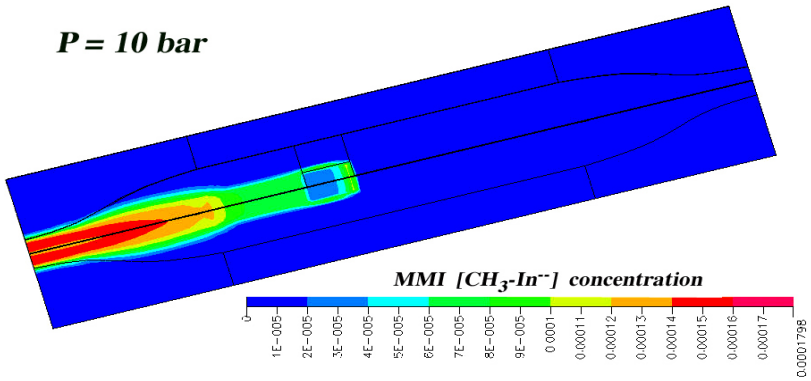

b)

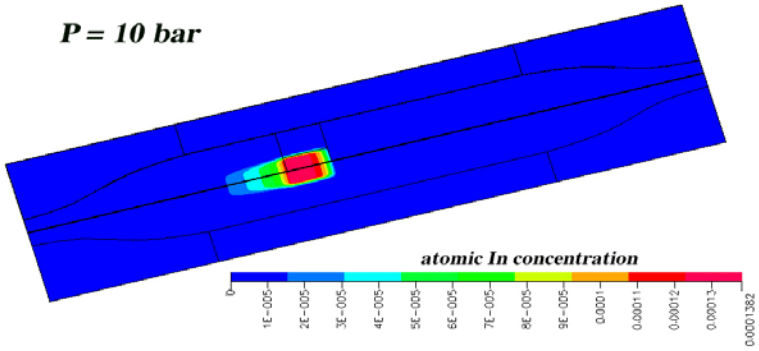

c)

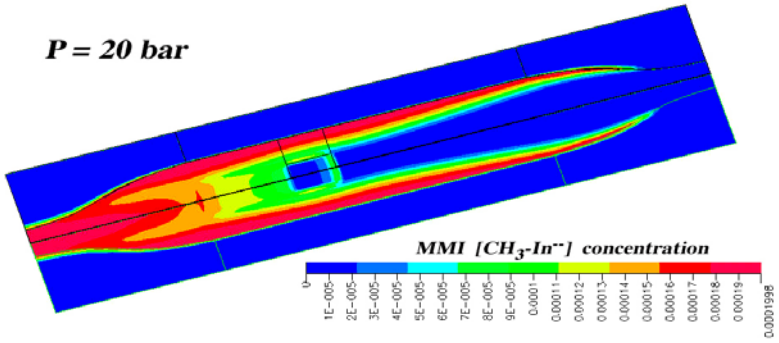

d)

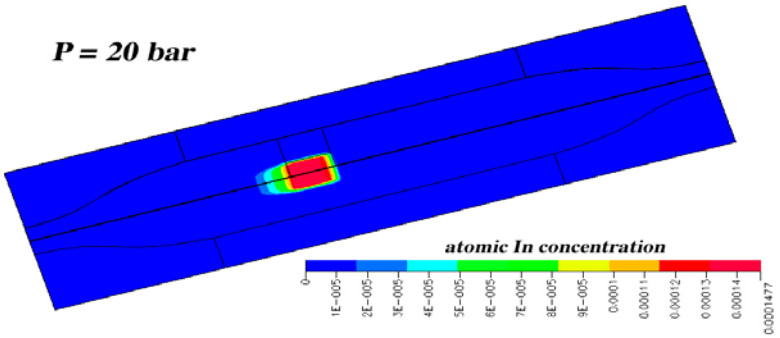

Figure 3.6: Trimethlyindium (TMI) gas phase decomposition in monomethylindium (MMI) and atomic indium at 10 and 20 bar at a substrate temperature of 1000 K and a flow of 12 slm.

The most dominate changes in the DMI, MMI and atomic indium concentrations are expected in the pressure range between 1 and 20 atm. As depicted in Figure 3.7, a further pressure increase beyond 40 bar does not significant alter the MMI and atomic indium concentration at the center of the substrate, which is accessible for experimental validation. These results are in good agreements with *ab initio* calculations by Cardelino et al., which show in inversion of monomethylindium versus atomic indium concentration in the pressure range of 1 bar to 20 bar

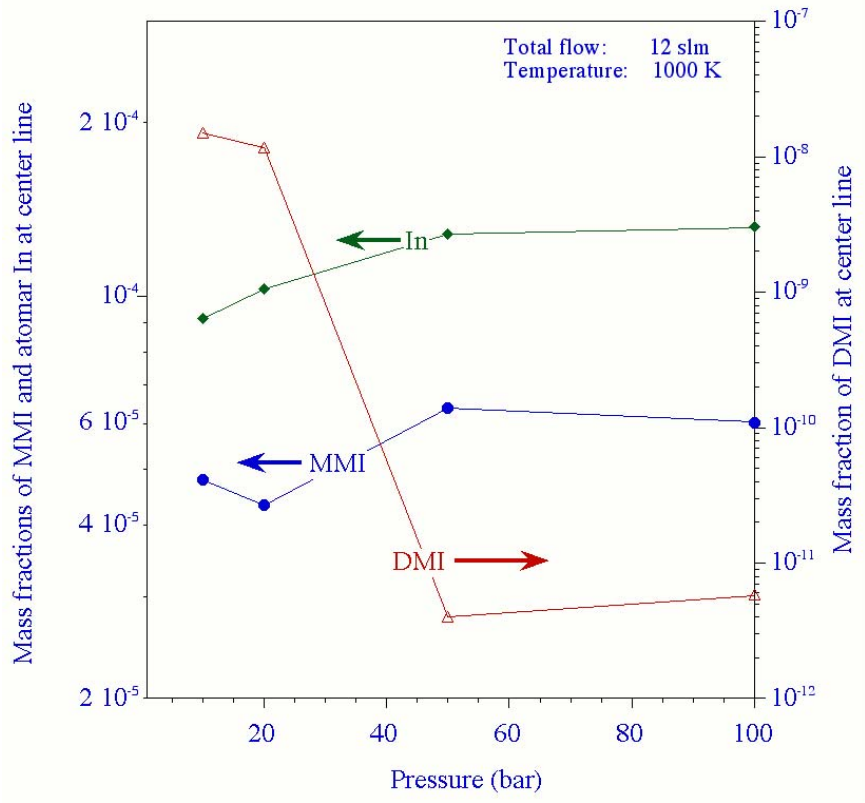

Figure 3.7: Effects of Pressure on Gas Phase Kinetics at T_s = 1000K and **u** = 12 slm.

3.4 InN Growth Rate Simulations

A two dimensional, time-dependent simulation model was used to study the gas phase reactions and transport with surface reactions leading to InN formation using a pulsing sequence as illustrated in Figure 3.4. The timing of the precursor injection keeps the process gases separate and thus precludes homogeneous formation and transport of adducts in the gas phase. The injection sequence introduces N_2 + TMI; N_2; N_2 + NH_3; N_2. into the reactor flow channel with an experimental limit of approximate 0.2 seconds. Figure 3.8(a). illustrates the site fraction of MMI adsorbed to the surface as a function of time. As shown in Figure 3.7(b)., the surface of the substrate is completely covered by MMI until NH is introduced and InN is formed. This film growth begins when NH is generated and interacts with the MMI covered substrate. The results are tentative in that experimental work needs to be done to validate the mechanisms selected and preliminary reaction rates theoretically derived.

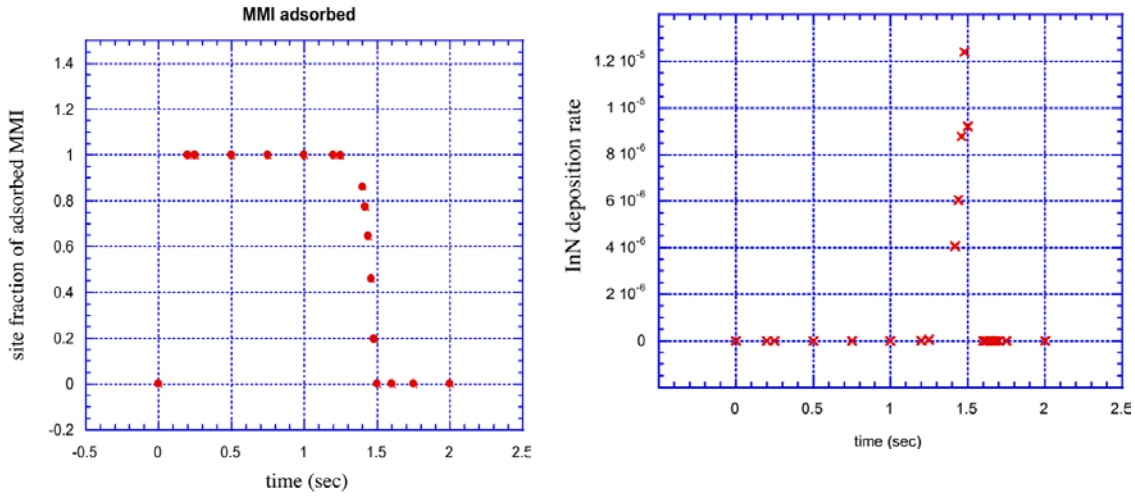

Figure 3.8(a): Site fraction of adsorbed MMI as a function of time. **Figure 3.8(b):** Deposition rate of InN vs. time at the center of the substrate.

4. Real Time Characterization of Gas Dynamics

Published as: "Real time optical characterization of gas flow dynamics in high pressure chemical vapor deposition." Vincent Woods, Harald Born, Martin Strassburg, and Nikolaus Dietz, Journal of Vacuum Science and Technology A **22**, 1596-1599 (2004)

4.1 Introduction

Solid solutions of group III nitrides, in particular of the GaN-InN system, are presently under intense development for optoelectronic and microelectronic applications. High quality Ga-rich epilayers of $Ga_xIn_{1-x}N$ can be fabricated successfully by traditional low pressure chemical vapor deposition (CVD) methods that focus on low pressure processes in order to minimize the influence of flow dynamics on growth conditions. However, low-pressure deposition processes are limited to a regime where the partial pressures of the constituents do not differ vastly and the decomposition process can be countered by off-equilibrium process conditions. In particular, the small formation enthalpy of InN hampers its epitaxial growth[62]. Off-equilibrium conditions such as employed in MBE and organometallic (OM) CVD growth of InN require low growth temperature to overcome the thermal decomposition pressures[63-66], which limits the quality of InN and In rich $Ga_xIn_{1-x}N$ epilayers. Due to the low temperatures, extremely high V-III ratios have to be applied to prevent the formation of metal droplets on the surface.[66-68] Meanwhile theoretical considerations suggest smaller V-III ratios[69]. Therefore, new approaches to InN growth must be explored. A CVD growth technique utilizing elevated pressure is required in order to stabilize the surface of InN at optimal

processing temperatures[48]. A high background pressure of nitrogen has been shown to stabilize the surface of InN at elevated temperatures but has not yet been incorporated into a CVD growth scheme. Therefore, growth of InN at higher pressures (1 – 100 bar) is expected to expand the processing window towards higher temperatures, leading to an improved crystalline quality and providing a closer match to the optimal processing temperature of InN.

However, the growth in an elevated pressure regime requires an assessment of the thermodynamic driving force and kinetic limitations of growth for understanding and optimization of high-pressure organometallic chemical vapor deposition (HPOMCVD) processes. The maintenance of laminar flow conditions during CVD growth is also crucial in order to provide homogeneous growth conditions.

In order to gain insights in the growth dynamics of HPOMCVD, we constructed a high-pressure reactor system for the growth of group III-nitrides that incorporates real time optical characterization capabilities. Only optical diagnostics will provide the real time information pertaining to gas flow dynamics in the reactor, allowing the characterization of laminar and turbulent flow regimes. In the following we introduce the high-pressure reactor design and the real time optical techniques used to characterize the gas flow conditions in the flow channel reactor. The characterization of the gas flow conditions in the reactor system are presented and analyzed in order to determine the process parameter under which laminar and turbulent flow can be maintained.

4.2 The High-pressure Reactor

The growth of group III-nitrides under high-pressure CVD conditions utilizing real time optical characterization requires the use of a new reactor system design. Figure 4.1 schematically illustrates the high-pressure reactor system which is composed of: a) a flow channel CVD reactor, b) a control and data acquisition system, and c) a gas flow and pressure control system with pulsed precursor compression and injection.

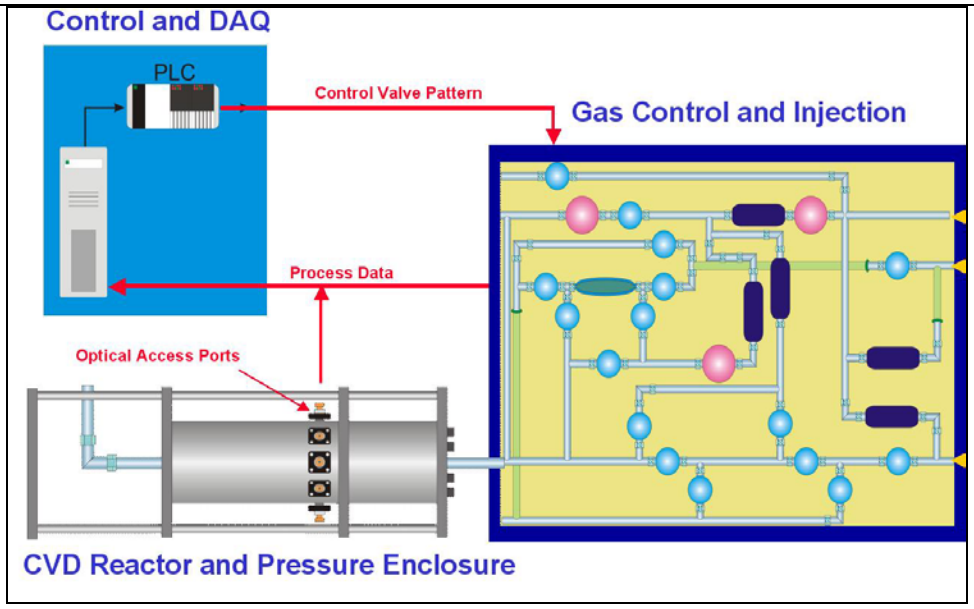

Figure 4.1: Schematic illustration of high pressure OMCVD system including the reactor and pressure enclosure, control and data acquisition and gas control and injection system.

The HPCVD reactor can be operated from atmospheric pressure up to 100 bar. The reactor provides optical access ports for the real time monitoring of gas flow dynamics and precursor decomposition kinetics. Additional optical access ports allow the monitoring of growth surface itself. Constant pressure and flow conditions in the reactor are maintained by the gas control and injection system. In addition, the gas control system provides for the compression of chemical precursors, (via carrier gas) and the subsequent timely controlled injection in the reactor. The temporally separated injection of precursors is important in order to suppress gas phase reactions, which become dominant in a dense gas phase. The system is fully computer controlled and utilizes a programmable logic controller (PLC) to provide precise synchronization between precursor injection and optical data acquisition.

Figures 4.2(a) and 4.2(b) depict the reactor flow channel assembly in the HPOMCVD reactor. Figure 4.2(a) shows one half of the reactor flow channel, which is symmetric in design. According to the applied design consistent thermal conditions are provided and simultaneous optical measurements from two substrates are enabled. The symmetry substrate/heating design provides an uniform heat profile in the reactor channel and avoids an undesired deposition on the opposite reactor channel. To maintain laminar flow conditions, the cross sectional area is kept constant through out the flow channel. Figure 4.2(b) depicts the cross sectional view of the center section of the reactor flow channel. The flow channel can be seen along the center axis of the assembly. The reactor flow channel in the center section is 50 mm in width and 1 mm in height.

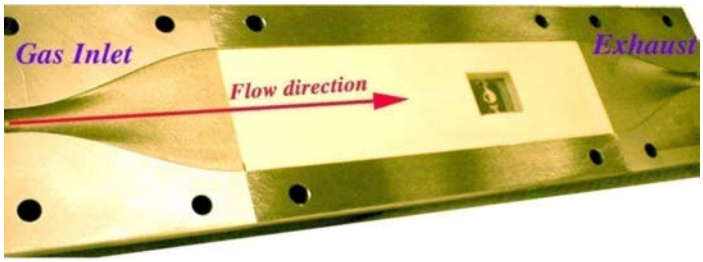

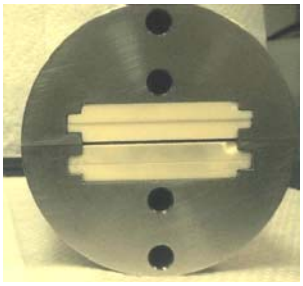

Figure 4.2(a): Half of the reactor flow channel assembly showing flow direction. The flow channel is designed with a constant cross sectional area for the maintenance of laminar flow. The sapphire substrate is seen along center axis of flow and is held in two α-Al_2O_3 plates. **Figure 4.2(b)**: Cross sectional view of the center section of the reactor flow channel assembly. The flow channel is visible along the center axis of the assembly between the sets of α-Al_2O_3 plates.

The reactor flow channel assembly is contained in a high-pressure enclosure, which can sustain pressures up to 100 bar. Figure 4.3(a) provides a view at the open high-pressure enclosure with the inserted flow channel reactor (arrow). The optical access ports are visible on both the top and sides of the pressure enclosure. These optical access ports enable the optical monitoring perpendicular to the flow direction along the centerline of the substrate as shown schematically in Figure 4.3(b). Two ports provide access to the flow channel and allow characterization of the gas flow conditions and gas phase reactions. Each half of the symmetric reactor provides three optical access ports to the backside of the substrate for the characterization of surface chemistry, thin film nucleation and coalescence, and for scattering processes from the gas phase.

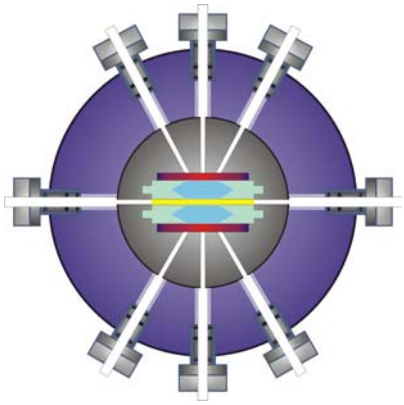

Figure 4.3(a) Cross sectional view of the open pressure enclosure. The top half of reactor flow channel assembly is indicated by the arrow. The two optical access ports to flow channel are shown on the sides and three of the six access ports to substrate are shown on the top. **Figure 4.3(b)** Schematic illustration showing the cross section view of the reactor system. The two optical access ports to the flow channel are illustrated on the sides.

4.3 Characterization of Flow Dynamics and Laminar Flow Regime

Maintaining laminar flow is crucial in CVD reactor systems in order to provide a consistent supply of precursor constituents that allows the correlation of gas phase constituent concentrations to the diffusion process and to the surface chemistry processes which drive the thin film growth. Therefore, the first task is to establish the process conditions under which laminar flow can be maintained. To characterize the gas flow dynamics, two real time optical characterization techniques were utilized simultaneously; laser beam profile analysis and laser light scattering (LLS). As schematically illustrated

in Figure 4.4, laser light was focus through an optical access port at the center of the flow channel. The transmitted beam passes through an exit rod, where the beam size is expanded and the intensity distribution analyzed via a CCD array. Simultaneously, a photo-multiplier tube was employed to monitor the forward component of LLS. The flow rates were varied from 3 slm to 21 slm for a given constant reactor pressure. The optical monitoring experiments were performed for both increasing and decreasing flows.

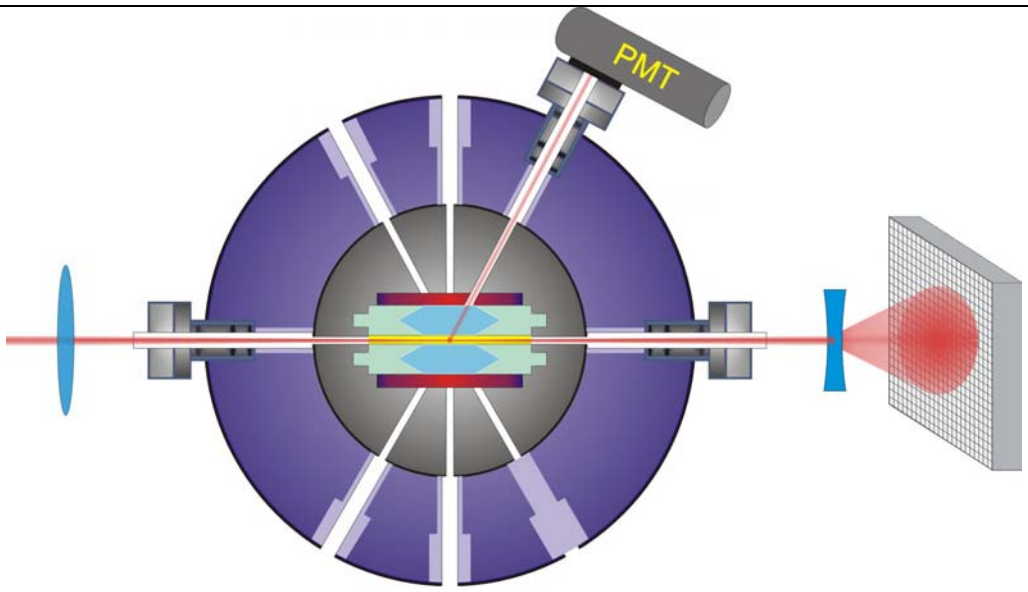

Figure 4.4: Cross sectional view of the HPOMCVD reactor showing optical access ports utilized for real time characterization of gas flow conditions. Laser light is focused to the center of the flow channel. Laser beam profile analysis was performed using a CCD camera. The forward component of the laser light scattering intensity was measured with a photo multiplier tube (PMT).

For laminar flow conditions, an uniform gas density is expected that results in a homogeneous index of refraction throughout the reactor flow channel. As the flow moves in to a turbulent flow regime, density fluctuations are introduced in the flow channel. The resulting temporal and spatial variation in the index of refraction is expected to increase the LLS intensity and to broaden the Gaussian laser beam profile. Images of the laser beam intensity were monitored by the CCD array at varied flows and pressures. A representative image is shown in Figure 4.5(a) with the outline of the optical access port indicated by a dotted circle. The intensity variations of the laser beam image are due to imperfections in the fused Silica rods uses as optical access ports. Beam profile analysis has been performed in order to fit a Gaussian distribution to the beam profile and is shown in Figure 4.5(b). The imperfections in the fused Silica rods introduced an additional broadening in the laser beam profile, which is superimposed to the beam broadening expected for turbulent flow conditions. The error bars obtained from the analysis for different flows and pressures indicated the laser beam profile analysis is not a reliable flow characterization technique.

The analysis of the simultaneously monitored LLS intensity showed surprisingly good results, which allowed the focusing solely on LLS analysis for the characterization of the flow dynamics. The LLS intensities as a function of flow rate at a constant pressure are depicted in Figure 4.6. The data were collected under constant pressure (9 bar) conditions and flow rates between 3 slm and 21 slm. The LLS intensity remains constant for flow rates below a critical point of approximately 7 slm. For flow rates above the critical point, a monotone increase in the intensity of LLS is observed. The

region (*"transition point"*) where the steady LLS intensity begins to increase indicates a transition from a laminar to turbulent flow condition. In order determine the laminar/turbulent *"transition point"* for our HPOMCVD reactor, the LLS intensities were measured and analyzed for pressures between 5 bar and 15 bar and flow rates from 3 to 21 slm.

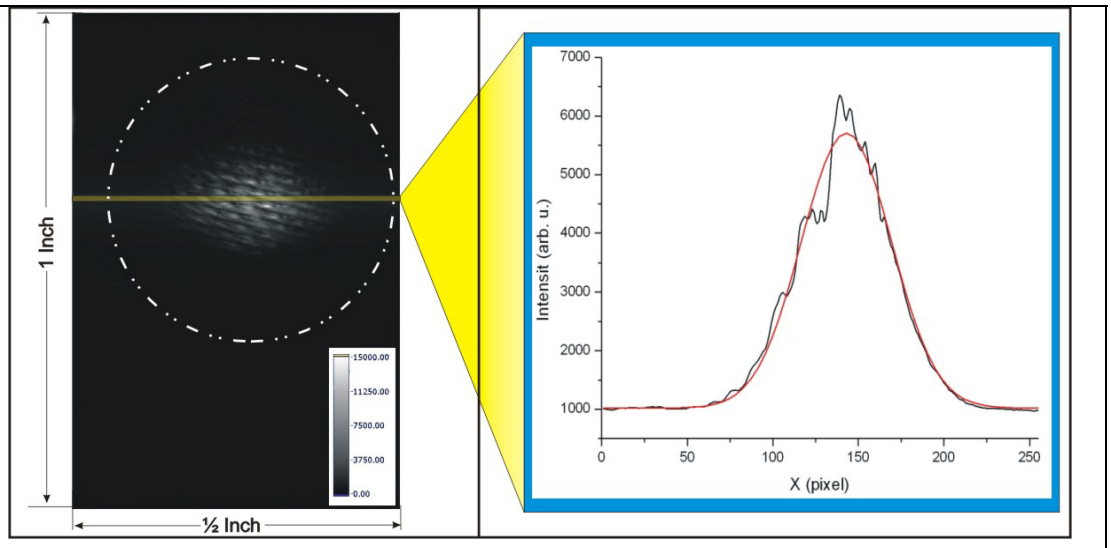

Figure 4.5(a): CCD image of laser beam at normal incidence. The variations in intensity are due to imperfections in the optical access ports. The dotted circle indicates the radius of the access port and the light band indicates the location of the profile analysis. **Figure 4.5(b):** Profile analysis of CCD image of laser beam at normal incidence showing CCD intensity as a function of location and Gaussian fit. The variations in intensity due to optical access port imperfections are clearly visible.

The LLS analysis is summarized in Figure 4.7 which shows the onset of turbulent flow (*"transition point"*) as a function of pressure and flow rate. As indicated, the onset of turbulent flow occurs at lower flow rates for increased pressures. This behavior is expected from the definition of the Reynolds number, $Re = \frac{\rho u l}{\eta}$, where ρ is the density and η is the viscosity of the gas, l is a characteristic length determined by the geometry of the flow channel and u is the flow velocity. Moreover, the density is proportional to the pressure of the gas. The obtained results support the inverse relationship between flow rate and pressure in laminar/turbulent flow transitions.

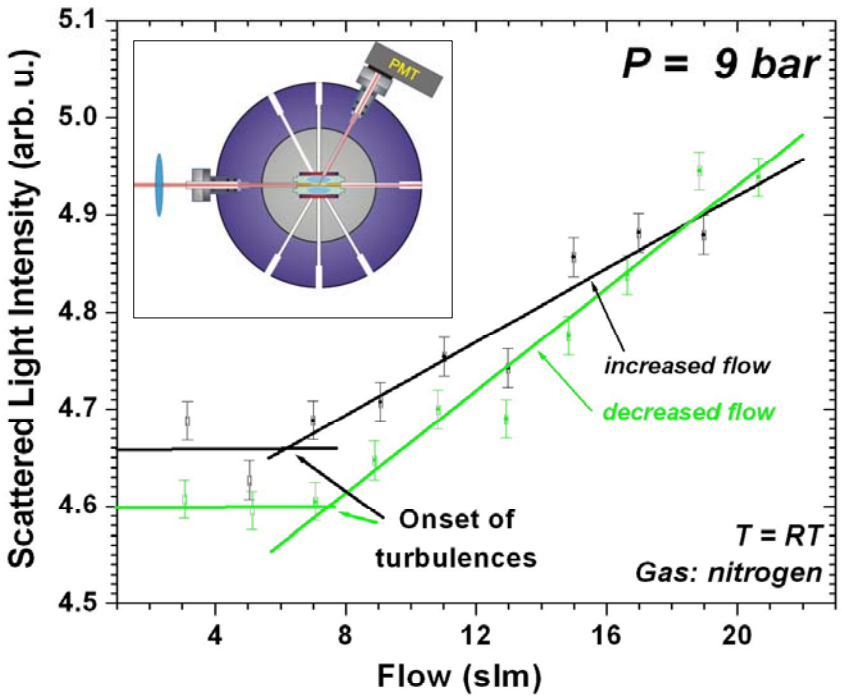

Figure 4.6: Scattered light intensity as a function of gas flow. These data were collected at 9 bar for flows of 3 slm to 21 slm. The onset of the increase in intensity corresponds to the transition from laminar to turbulent flow and occurs at approximately 7 slm.

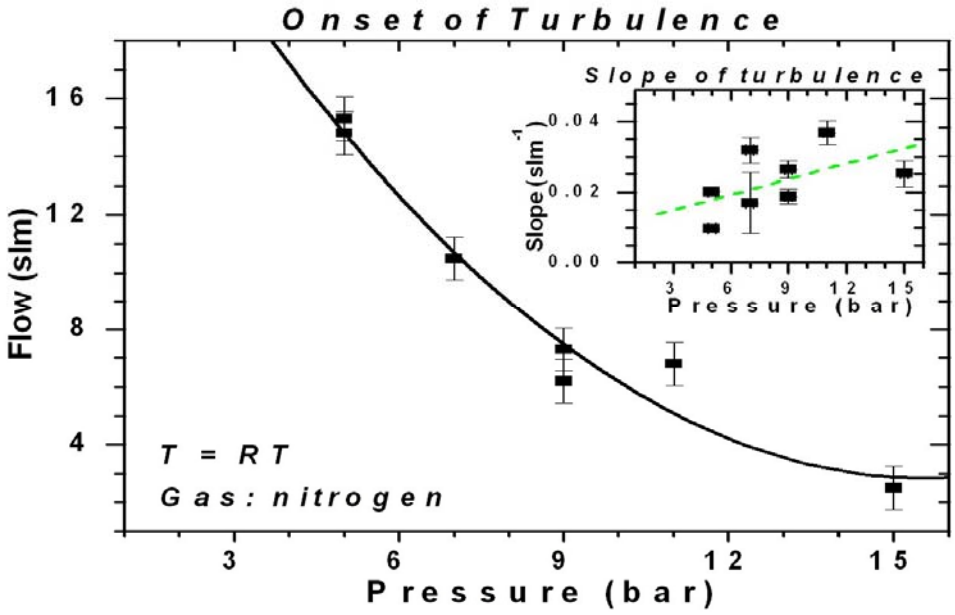

Figure 4.7: Summary analysis of the transition from laminar to turbulent flow conditions as determined by LLS intensity measurements. Data reveal that the onset of turbulence occurs at decreased flow rates for increased pressures. Laminar flow condition is expected for pressure and flow rate settings that fall beneath the line connecting the onset points.

The LLS analysis indicates that for the high-pressure flow channel reactor laminar process condition can be maintained for flows up to 20 slm and pressures up to 20 bar.

4.4 Conclusions

We analyzed the flow dynamics in a high-pressure flow channel reactor utilizing its integrated real time optical characterization capabilities. The process window for laminar growth conditions has been established by analyzing the laser light scattering

(LLS) intensity as a function of flow rate and pressure. The analysis determined the onset of turbulent flow as the transition point where the LLS intensity monotone increases. Laminar flow conditions can be maintained in a processing window of pressure ranges from 1 bar to 15 bar and flow rates from 3 slm to 21 slm. LLS has been demonstrated as a simple and robust tool for the characterization of gas flow conditions.

Acknowledgements

This work has been supported by NASA under Grant No. NAG8-1686. M.S. gratefully acknowledges the support of the Alexander von Humboldt-Foundation.

5. Gas Phase Kinetics

5.1 Introduction

Improvements in the materials quality and a more detailed understanding of the growth kinetics of group III-nitride compound semiconductors is of crucial importance to advance the fabrication of optical electronic device structures. Even though much progress has been made for the GaN material system, InN and AlN have become increasingly significant due to their unique properties as low band gap and wide band gap materials, respectively. At present, low-pressure deposition processes such as organometallic chemical vapor deposition (OMCVD - also denoted as MOVPE)[66,70] and molecular beam epitaxy (MBE)[24,71] are used, with limitations in the temperature regime and the control of the partial pressures of the constituents. The off-equilibrium conditions employed in MBE and OMCVD for the growth of InN also require low growth temperatures to overcome the thermal decomposition pressures, thus limiting the quality of InN and related group III-nitride epilayers[24,72-74], as outlined in controversial reviews on the present status of InN growth and characterization provided by Bhuiyan et al.[24] and Davydov et al.[75].

In order to get a handle on the vast difference in the vapor particle pressures of group III elements and nitrogen, and to control the thermal decomposition pressures over the growth surface, new approaches for the growth of In-rich group-III-nitride alloys need to be explored to control the point defect chemistry, leading to improved structural and optical properties of InN and related alloys.

Recent studies of the indium - nitrogen system[76] show much uncertainty in the p - T - x relationship due to missing experimental validation. However, studies of the nitrogen pressure required to prevent thermal decomposition of bulk InN, provided a relationship given by

$$p(N_2) \rightarrow p_0 \exp\left[-\frac{\Delta H_r}{R}\left(\frac{1}{T} - \frac{1}{T_0}\right)\right] , \qquad (1)$$

which results in the p-T^{-1} relation shown in Figure 5.1[48]. The relation indicates that in the pressure range $p_{N_2} \leq 10^2$ bar and for substrate temperatures $\leq$ 900 K the surface decomposition of InN will be effectively suppressed.

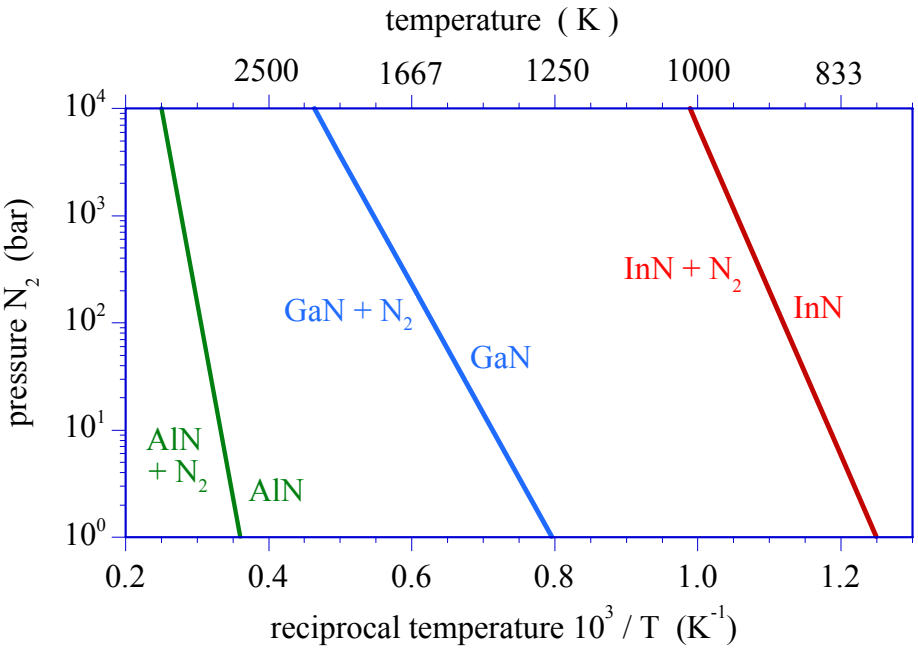

Figure 5.1: Thermal decomposition pressure vs. reciprocal temperature for AlN, GaN and InN[48].

This chapter focuses on the growth of group III-nitrides under high pressure chemical vapor deposition (HPCVD) conditions using InN as a model system in order to demonstrate the capabilities of HPCVD. InN is the most challenging material system, due to the fact that the equilibrium vapor pressure of nitrogen over InN is much higher as compared to AlN and GaN[67]. A high-pressure flow channel reactor with incorporated real time optical characterization capabilities[77-80] is utilized to study and optimize the InN nucleation and growth[55,81-83]. At above atmospheric pressures, optical diagnostic techniques are uniquely suited to provide real time information pertaining to gas flow dynamics in the laminar and turbulent flow regimes. Optical diagnostics are also being utilized to obtain crucial information on the precursor flow and decomposition kinetics. Several optical techniques have been explored, but only a small group satisfy the requirements of being robust as well as sensitive. For example, the substrate temperature during typical InN growth lies between 800K and 1200K, emitting significant visible and infrared radiation[84]. This favors the utilization of ultraviolet absorption spectroscopy (UVAS) or ultraviolet induced fluorescence spectroscopy to identify the group-V and organometallic group-III precursors in the gas phase, a technique well established in literature[85-88].

Moving towards HPCVD for the growth of group III-nitrides requires a reactor design with additional considerations of flow kinetics, gas phase reactions, diffusion through the surface boundary layer as well as altered surface chemistry[89]. To *minimize* gas phase reactions, extract sufficient organometallic (OM) nutrients from the bubbler,

and embed the precursor flow in the main reactor gas stream, a pulsed precursor injection scheme has been implemented, which is essential for

- *compression of precursors to reactor pressure,*
- *minimization of gas phase reactions,*
- *engineered nucleation kinetics and layer growth, and*
- *analyzing the gas-phase and surface decomposition dynamics in real-time.*

The implementation of the HPCVD system is schematically depicted in Figure 2, which shows the reactor cross section containing the substrates and optical monitoring plane, perpendicular to the flow direction. The flow channel is embedded in an inner reactor cylinder, while an outer reactor pressure vessel confines the overall pressure for well above 100 bar. The substrates are symmetrically embedded in the upper and lower part of the flow channel in order to prevent preferential material deposition. Optical access ports are integrated along the center axis of the substrates, allowing optical characterization of flow kinetics, gas phase reactions via laser light scattering (LLS) and UVAS. The optical access ports also provide access to the substrate surface through the back side, enabling the use of principal angle reflectance spectroscopy (PARS) and LLS in back-scattering geometry[77,80].

The HPCVD flow characteristics were analyzed using laser light scattering (LLS) in a forward scattering geometry[79,90], indicating that laminar flow conditions can be maintained in the flow and pressure regime of 1 standard liter per minute (slm) to 16 slm and 1 bar to 15 bar, respectively. The associated Reynolds number of the reactor flow channel averaged around 1480 with no significant pressure dependency observed[91].

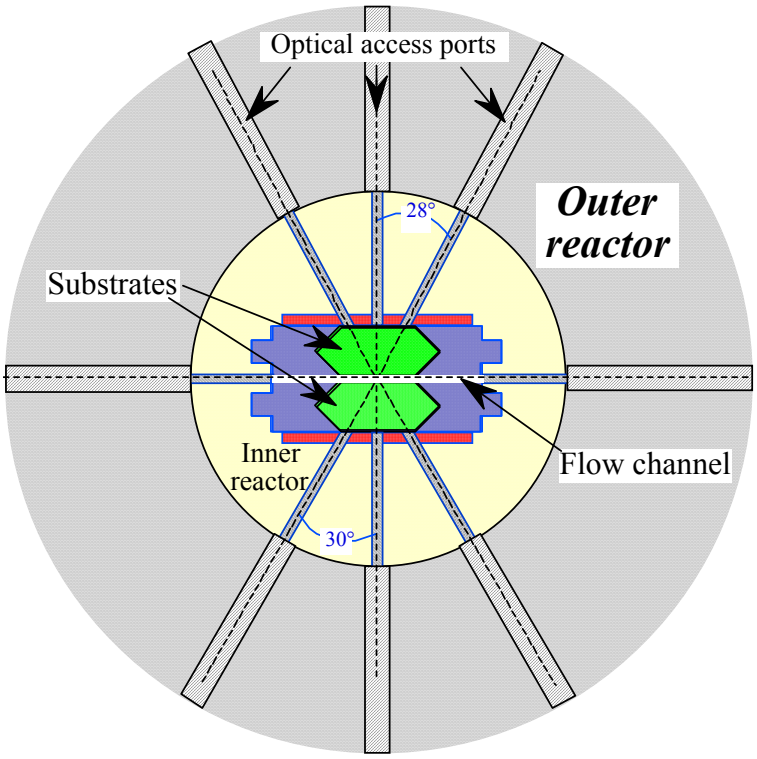

Figure 5.2: Schematic cross section of the reactor containing the optical access ports and the center of the substrates. Two optical ports provide access to the flow channel and three ports in each of the two half sections of the reactor provide access to the growth surface.

In the following sections, the optical characterization of ammonia during continuous and pulsed injection is presented. As outlined above, the pulsed precursor injection scheme is primarily essential for the compression of precursors up to reactor pressures. However, it is also crucial for analyzing and controlling the gas-phase and surface decomposition dynamics.

5.2 UVAS characterization of continuous ammonia flow

The optical characterization of NH_3 is treated separately for continuous flow and pulsed NH_3 injection. Under continuous flow condition, the vapor is transported from a gas cylinder, with a pressure set at 30 psi. The NH_3 flow is controlled via a mass flow controller with a 1 slm maximum flow, expressed via y = 1 -100% full scale (FS). The molar flow of ammonia and number of ammonia molecules per unit time are given by

$$n_{NH_3}=7.4405\cdot 10^{-6}\cdot y \quad [mol\cdot s^{-1}] \text{ and } N_{NH_3}=4.4808\cdot 10^{18}\cdot y \quad [s^{-1}], \quad (y=0\text{-}100\%FS) \quad (2)$$

respectively. The molar ammonia flow ratio χ through the reactor, defined as the ratio of ammonia flow rate to total flow (precursor flow plus nitrogen), can be expressed in term of the percentage of full scale flow, z and y as

$$\chi = \frac{n_{NH_3}}{n_{total}} = \frac{n_{NH_3}}{n_{Main\_N_2} + n_{NH_3}} = \frac{y}{50\cdot z + y}. \quad (3)$$

where z represents the nitrogen main flow with 50 slm maximum flow (z= 0 to 100 %FS). The ammonia induced absorption has been characterized by UVAS in the wavelength range of 180 nm to 300 nm. Figure 5.3 shows the UV absorption spectra for ammonia flow ratios χ in the range of 10^{-1} to 10^{-3} at room temperature (RT) and a reactor pressure of 1.6 bar, which are typical molar ammonia flow ratios χ required for the growth of InN. As depicted in Figure 5.3, even for the lowest flow setting, several of the absorption structures at higher energies exhibit a saturation effect and are not suitable for ammonia

characterization in the molar flow ratios. The absorption peak positions match those reported in literature[92,93] for a constant ammonia volume. No literature data were found for continuous ammonia flow characterization.

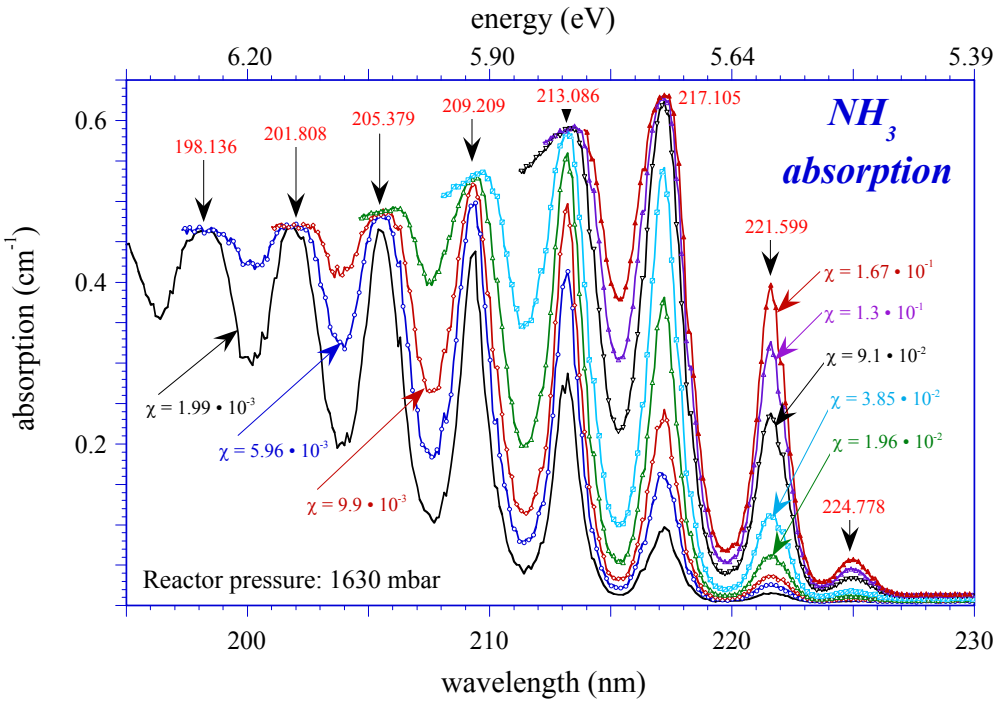

Figure 5.3: Absorption spectra for ammonia flow ratio χ in the range of 10^{-3} to 10^{-1} for a rector pressure of 1.6 bar.

In order to characterize ammonia molar flow rate below 10^{-3}, a second mass flow controller with 2 sccm full scale flow was utilized. The UV absorption spectra for ammonia flow ratios χ in the range of 10^{-4} to 10^{-5} are depicted in Figure 5.4. These spectra have been corrected in order to eliminate the nitrogen base line absorption. Overall, a total of 9 absorption features were identified being sensitive to molar ammonia

flow rates less than a part per billion per sec. The sensitivity ranges for each of the absorption peak maximum are summarized in table 5.1. The analysis of the peak maxima indicate a linear relationship between absorption peak maxima and the ammonia flow ratio in a double logarithmic scale[84].

For the growth of InN, ammonia flow ratios on the order of 10^{-2} are required. For these ammonia flow ratios, the UV absorption peaks at 217.1 nm and 221.6 nm are best suited for further analysis. However, due to the onset of saturation in the absorption peak at 217.1 nm, this peak will only be considered for ammonia flow ratios for smaller ammonia flows. The correlation for these two absorption peak maxima with the flow ratio χ can be expressed as

$$\begin{aligned} \alpha_{peak\_217.1nm}(\chi) &= 0.38 \times \ln(\chi + 0.011) - 2.0 \times \chi + 1.73 \quad [cm^{-1}] \\ \alpha_{peak\_221.6nm}(\chi) &= -45 + 45.01 \times \exp\left(\chi/18\right) \times 10^{-2} \quad [cm^{-1}] \end{aligned} \tag{4}$$

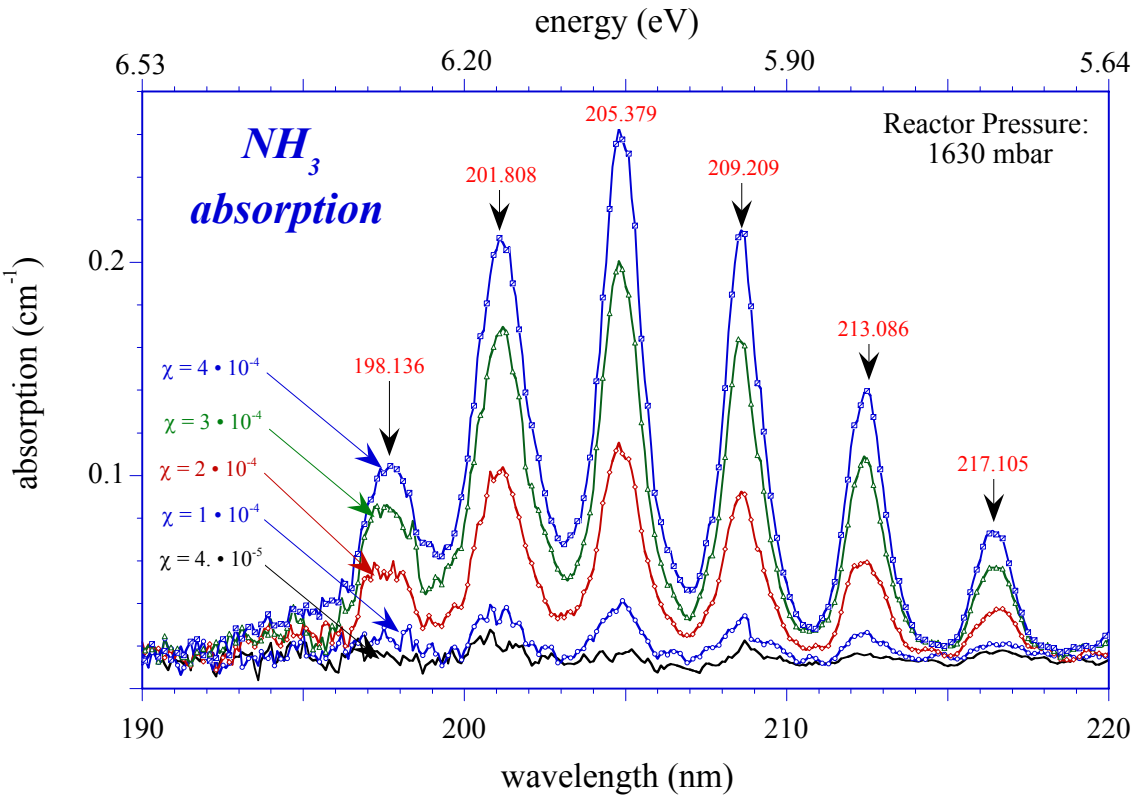

Figure 5.4: Absorption spectra for ammonia flow ratio χ in the range of 10^{-5} to 10^{-4} for a rector pressure of 1.6 bar.

No.	Ammonia absorption peak maximum (nm)	Sensitivity range (Molecules per sec)
1	194.62	$< 10^{+15}$
2	198.136	$< 10^{+16}$
3	201.808	$< 10^{+16}$
4	205.378	$10^{+14} – 10^{+17}$
5	209.209	$10^{+15} – 10^{+17}$
6	213.086	$10^{+16} – 10^{+18}$
7	217.105	$10^{+17} – 10^{+19}$
8	221.599	$10^{+18} – 10^{+21}$
9	224.788	$10^{+21} – 10^{+23}$

Table 5.1: Ammonia absorption peak maxima and their sensitivity ranges

For ammonia flow ratios in the range of $\chi = 1.0*10^{-2}$ to $1.6* 10^{-1}$, the absorption maxima at 221.6 nm is used to provide the correlation between UV absorption and the molar flow ratio χ as shown in Figure 5.5a. The number of NH_3 molecules per unit time is computed as function of the observed UV absorption. For the UV absorption feature located at 221.6 nm, we find the number of NH_3 molecules per time unit as

$$N_{NH_3}(\lambda = 221.6nm) = \frac{7.17 \times 10^{21} \times x \times \ln(\alpha')}{1 - 32 \times \ln(\alpha')} \left[s^{-1}\right] \; with \; \alpha' = \frac{\alpha_{@221.6nm}}{80.01}. \qquad (5)$$

Figure 5.5b shows the correlation between ammonia moleculues per time unit and the ammonia flow ratio in the range of $\chi = 1.0 * 10^{-2}$ to $9.0 * 10^{-1}$, for a reactor pressure of 1.6 bar. Under those conditions, the ammonia flow varies between 10^{19} and $2.5*10^{20}$ NH_3 molecules per sec under continuous flow conditions.

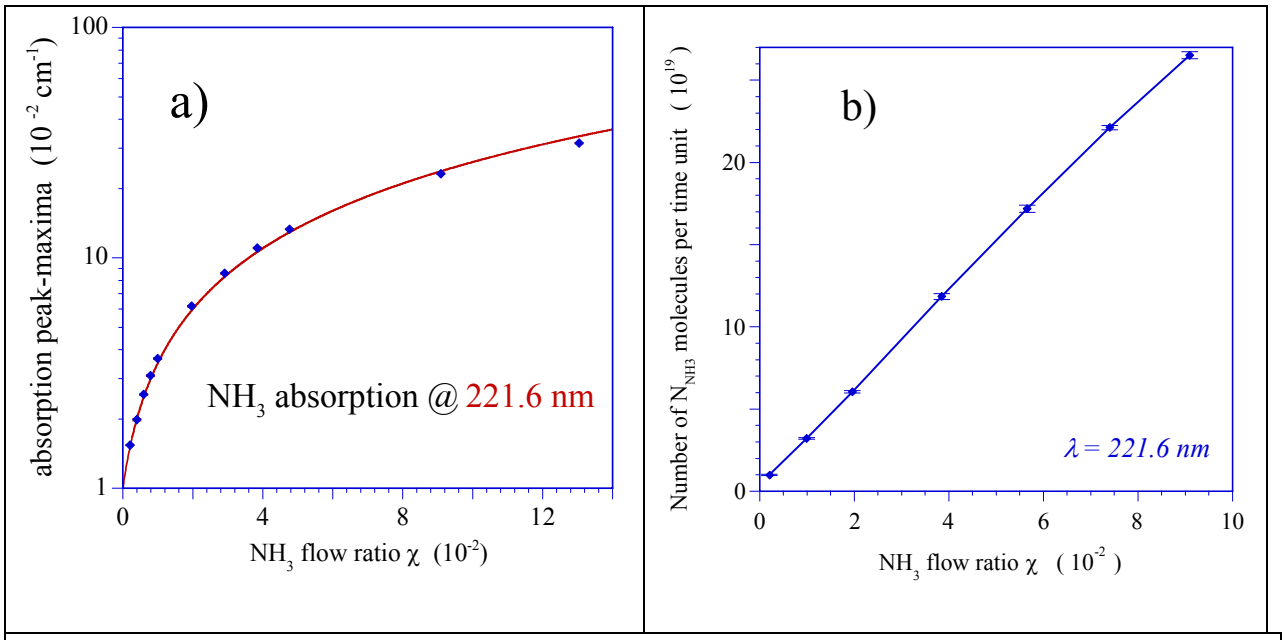

Figure 5.5a) Ammonia absorption monitored at λ=221.6 nm as function of ammonia flow ratio χ under steady state flow conditions for a reactor pressure of 1.6 bar. **Figure 5.5b)** Calculated concentration of ammonia molecules per sec using the absorption line at λ = 221.6 nm under continuous flow conditions.

5.3 UVAS characterization of pulsed ammonia injection

The flow of ammonia at higher pressures requires a compression and dilution step in order to allow ammonia gas to be injected in the HPCVD reactor. To accomplish this, an ammonia reservoir is filled at slightly above atmospheric pressure. In the following steps, the reservoir is compressed with nitrogen carrier gas and temporally controlled injection into the reactor. The cycle repetition rate, duration of injection, and position of injection can the adjusted within 10 ms resolution. Figure 5.6 shows typical absorption traces for various ammonia flow rates monitored at 221.6 nm during pulsed ammonia injection with a 6 sec repetition period. The reactor pressure and total gas flow were kept constant. The total number of ammonia molecules flowing through the reactor can be

calculated using the relationship between the UV absorption and ammonia flow rate provided by equation (5), taking in to account the compression ratio and gas reservoir volume.

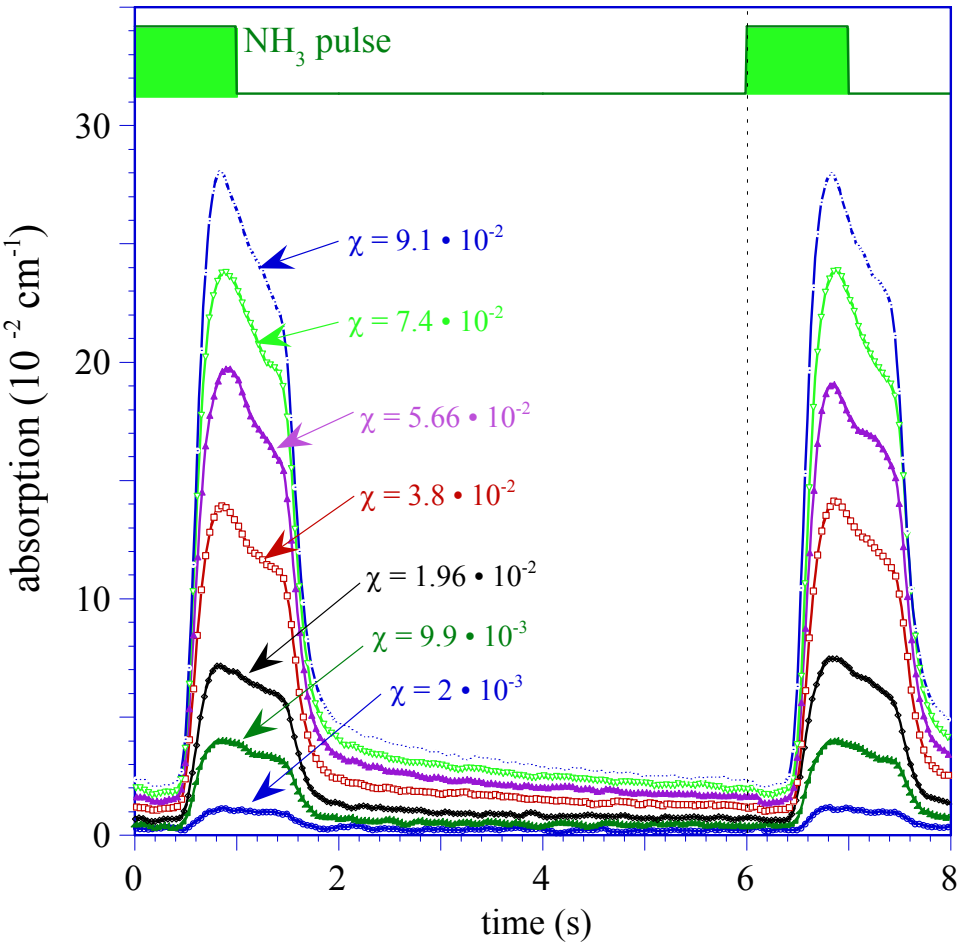

Figure 5.6: Ammonia absorption traces monitored at λ=221.6 nm for 1 sec NH_3 pulses injected 6 sec apart.

The pulsed ammonia injection has been analyzed as function of pulse width, ammonia molecules per pulse, total reactor flow and reactor pressure. Figure 5.7 shows the monitored absorption traces at λ=221.6 nm for various reactor pressures, while maintaining constant total gas flow at 5 slm and ammonia flow at 0.2 slm . A carryover of the UV absorption trace from one sequence to the next is observed at reactor pressures above 10 bar which results in an increase of the base line in the overall UV absorption.
As the reactor pressure is increased for a given fix flow rate, the ammonia pulses monitored at the substrate center line show three distinct features:

i) a systematic shift in the pulse arrival time,
ii) a systematic ammonia pulse broadening, and
iii) a change in the NH_3 absorption cross section for pressures larger 8 bar.

As shown in the following analysis, these distinct features provide crucial information pertaining to the reactor flow characteristics such as the average gas flow velocity. In addition, these features provide a pathway for the monitoring and engineering of the gas phase chemistry, which is crucial for the optimization of InN growth conditions. As shown in the following analysis, these distinct features provide crucial information pertaining to the reactor flow characteristics such as the average gas flow velocity. In addition, these features provide a pathway for the monitoring and engineering of the gas phase chemistry, which is crucial for the optimization of InN growth conditions.

5.4 Flow characterization during pulsed precursor injection:

The time delay Δt between the start of the ammonia pulse injection sequence and the arrival of the diluted ammonia gas to the center of the substrate is determined by the pneumatic valve opening time t_v, the reactor flow channel geometric factor r_g, the reactor pressure p_r (in bar) and the total gas flow through the reactor in terms of standard liters per min (slm) as:

$$\Delta t = t_v + \frac{l_d}{v_g} = t_v + r_g \cdot \frac{p_r}{V_{slm}} \qquad (6)$$

The reactor geometry factor r_g is a constant, containing parameters such as the reactor cross section A and the distance l_d between the injection valve and the substrate center line. Its unit is $[\,l \cdot min^{-1} \cdot bar^{-1} \cdot s\,]$. The time differences Δt as analyzed for ammonia precursor pulse injection rates of 6 s is depicted in Figure 5.8 as function of total gas flow and reactor pressure. Analysis of the time delay under these conditions reveals that the pneumatic valve opening time t_v = 240 ms and the reactor geometry factor r_g = 0.70 can be treated as constant values.

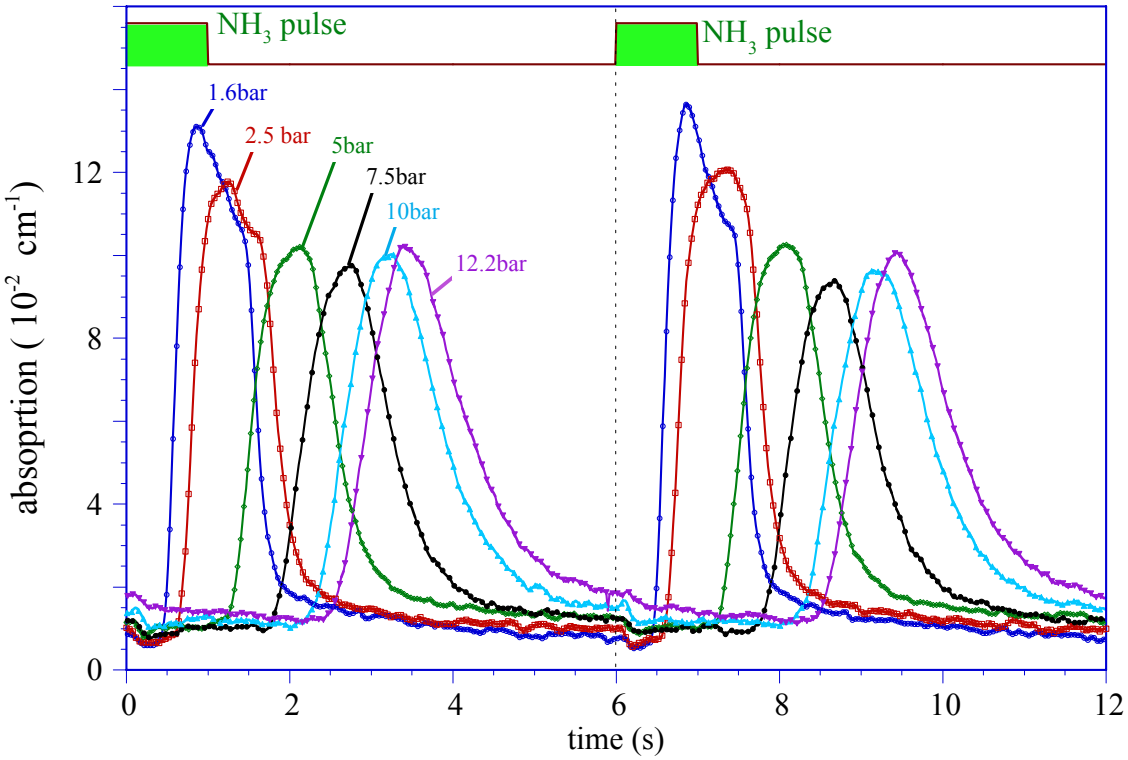

Figure 5.7: Absorption traces monitored at λ=221.6 nm for 1 sec NH_3 pulses injected 6 s apart. The reactor main flow and the ammonia flow were kept constant at 5 slm nitrogen and 0.2 slm, respectively.

The analysis also provided corrected values for the actual total gas flow through the reactor, which deviates from the set flow for higher flow rates. Based on this analysis, the average gas flow velocity v_g through the reactor system can be computed as

$$v_g = \frac{l_{dr} \cdot V_{slm_{cor}}}{r_g \cdot p_r} = 136.7 \cdot \frac{V_{slm_{cor}}}{p_r}, \qquad (7)$$

showing a direct relationship between the total gas flow V_{slm} and an inverse relationship to the reactor pressure. Note that this is the average gas flow velocity in the reactor system. Based on the reactor cross section and the gas volume per time unit, the average

flow velocity over the substrate is estimated at a factor 2 smaller due to the larger reactor flow channel cross section as compared to the precursor and carrier gas lines.

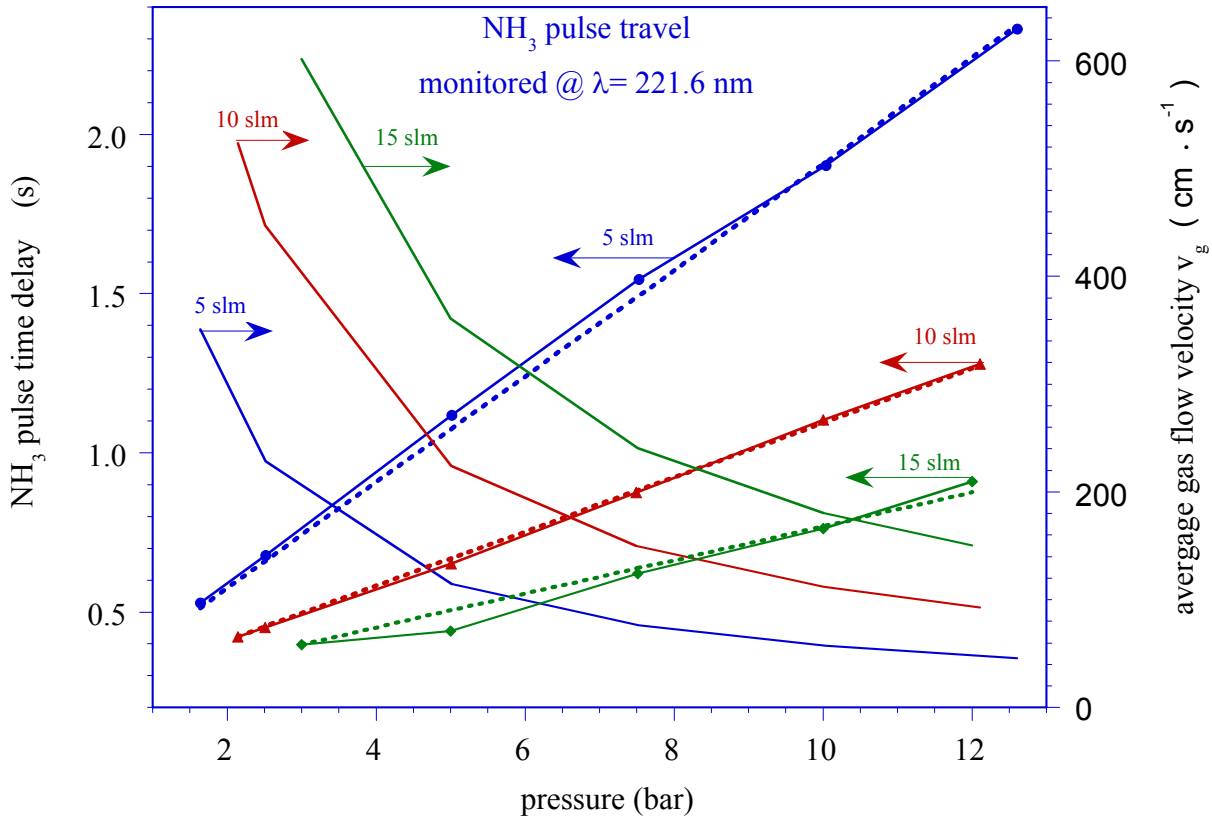

Figure 5.8: Time shift between injection and onset of pulse arrival at the substrate center line as function of the reactor pressure and for different flow rates. The right scale shows the computed average gas velocity v_g. between the ammonia reservoir and the substrate center line.

The systematic ammonia pulse broadening shown in Figure 5.7 can be directly explained from the relationship between gas flow velocity and pressure, as provided in equation 7. The reason for the pronounced increase in the NH_3 absorption observed for

pressures larger than 8 bar is at present not fully understood and requires a more detailed study. However, one possible explanation for this increase in the UV absorption is an increase in the UV absorption cross section for ammonia at elevated pressures. Such an increase in the UV absorption cross section would be beneficial for the decomposition kinetics of ammonia at elevated pressures as it would result in a more efficient decomposition of the ammonia precursor. The pulsed precursor flow characterization allows for precise engineering of precursor pulse separation / overlap and with it the control of gas phase chemistry and surface chemistry during the growth process.

5.5 Ammonia decomposition

The decomposition dynamics of ammonia have been analyzed in the temperature range of 300K to 1200K under continuous ammonia flow conditions for a reactor pressure of 1.6 bar. Figure 5.9 shows the change in the peak absorption maxima for an ammonia molar flow ratio χ of $4*10^{-3}$ as a function of temperature for absorption features found between 180 nm and 230 nm. The shift of the base line UV absorption due to the N_2 carrier gas has been taken in to account. As depicted in Figure 5.9, a significant reduction in the absorption strength is observed above 1000K, indicating the onset of decomposition of ammonia in the flow channel. The absorption peak maxima increase as the temperature rises due to the change in the absorption cross section. Above 900K a plateau is observed indicating the onset of decomposition with a strong cutoff above 1100K. Spectroscopic scans between 180 nm and 400 nm revealed no new UV

absorption features (not shown here) that could be associated to ammonia fragments at elevated temperatures. However, a broad background absorption in the wavelength regime of 250 nm and 350 nm is observed for high temperatures, the origin of which is still under investigation.

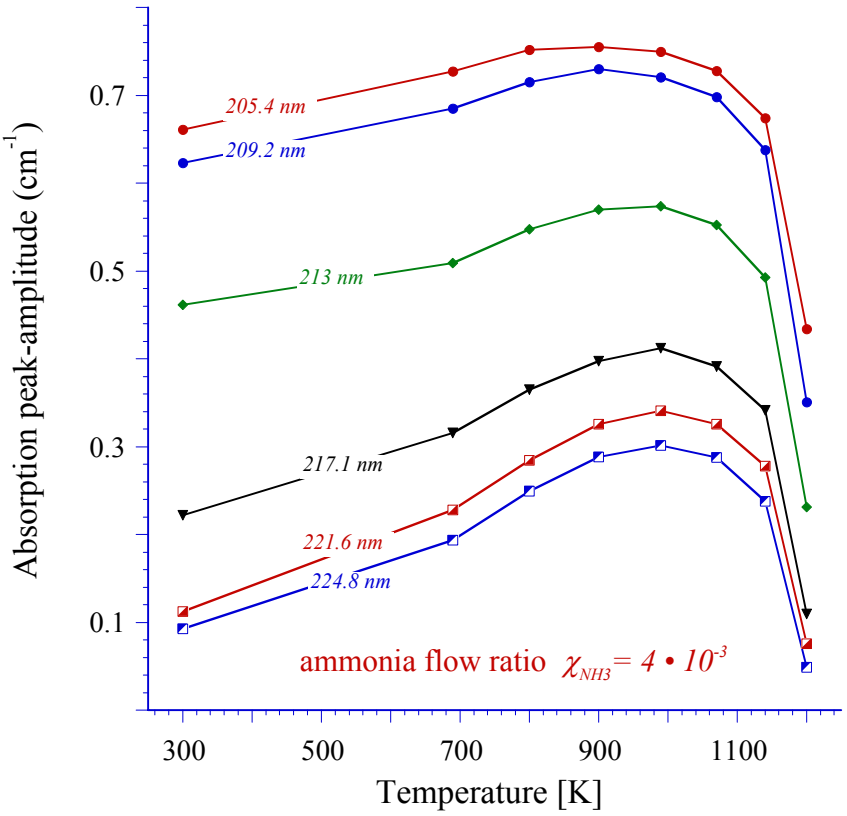

Figure 5.9: Ammonia absorption spectra taken at different temperatures during steady state flow conditions for a reactor pressure of 1.6 bar

5.6 Ammonia and Trimethlyindium (TMI) decomposition at higher pressures

For the growth on InN, the decomposition dynamics of the precursors ammonia and TMI at higher pressures are of importance. Figure 5.10a shows the temperature dependency of the UV absorption of ammonia monitored at 210.7 nm while maintaining a reactor pressure of 10 bar. For this elevated pressure, the onset of decomposition as indicated by a decrease in the UV absorption occurs at a temperature of about 850K. This indicates a significant reduction in the decomposition temperature as compare to that at atmospheric pressure, where the onset of ammonia decomposition was observed at about 900 K (see Figure 5.9). As for ammonia, also analyzed the TMI UV absorption spectrum, which has an absorption peak maximum at 213 nm. At present, there are no known experimental studies on the decomposition dynamics of TMI at higher pressures, however, several studies for low-pressure OMCVD growth conditions have been reported[59,86,94]. Figure 10b shows for comparison the TMI peak absorption as function of temperature, indicating that the onset of decomposition in the gas phase occurs around 800K. This onset in decomposition is slightly higher than those reported under low-pressure OMCVD conditions[86,95]. More detailed studies using UVAS and optical emission spectroscopy as function of pressure are required to correlate the experimental results to theoretical predications for the TMI decomposition at elevated pressures as formulated by Cardelino et al.[82].

The observed decrease of the temperature at which the onset of ammonia decomposition occurs under elevated pressure conditions is crucial for the optimization of the growth of InN and the control of point defect chemistry in this material system.

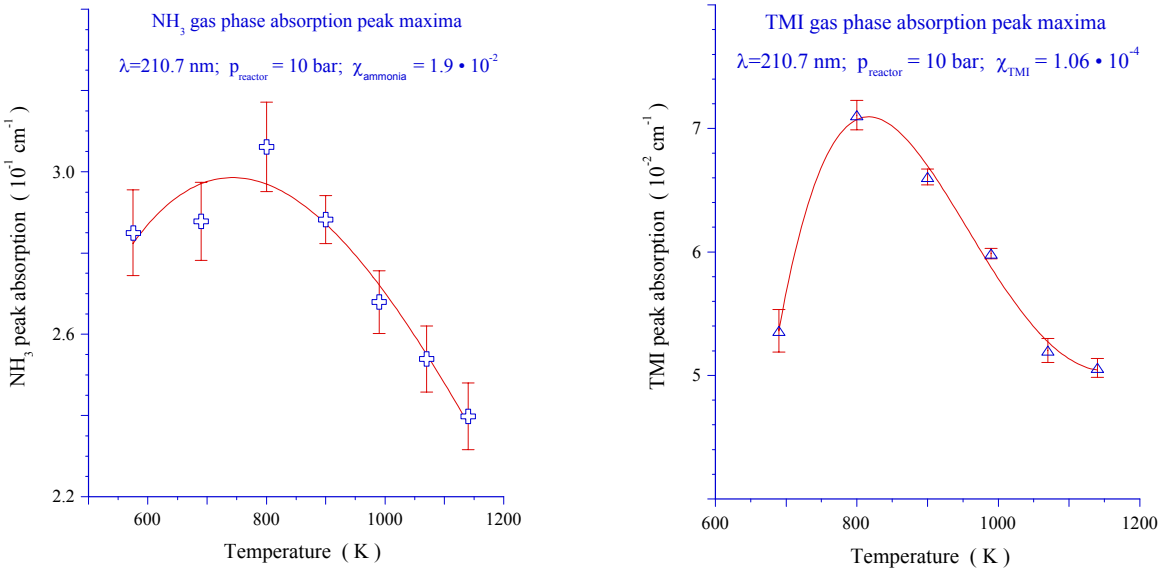

Figure 5.10a Change of the ammonia absorption peak maximum as function of temperature. **Figure 5.10b** Decomposition of TMI at 10 bar reactor pressure, monitored during pulsed TMI injection as function of temperature.

5.7 Conclusion

The flow kinetics and decomposition dynamics of the precursor gas ammonia have been studied by ultraviolet absorption spectroscopy (UVAS) during continuous flow and pulsed precursor injection. An analysis of the various UV absorption features with respect to the ammonia flow rates is provided, showing high sensitivity to less than a part per billion molecules per sec. For the ammonia molar flow ratios χ on the order of 10^{-2} to 10^{-1}, a direct relationship between the ammonia absorption strength at 221.6 nm and the ammonia flow rate is shown. Analysis of pulse shape and traveling time under a

pulsed injection of ammonia yield the average gas flow velocity in the HPCVD system as function of the total gas flow rate and the reactor pressure. The onset of ammonia decomposition is found to start above 900K at atmospheric pressure. At higher reactor pressures, the onset of decomposition is shifted to lower temperature, indicating a better match to the decomposition kinetics of TMI for the growth of InN.

6. Real Time optical characterization of InN growth

Published as: "InN growth by high-pressure chemical vapor deposition: Real-time optical growth characterization" Vincent Woods, Nikolaus Dietz, Materials Science & Engineering B **127**, 239-250 (2006)

6.1 Introduction

The development of integrated ultraviolet (UV) light emitting diodes (LEDs), laser diodes, solar blind detectors, high-frequency/high-power transistors operating at high temperature and room-temperature spintronic devices that are based on group III-nitride compound semiconductors has generated much interest in recent years. Of particular interest is an improved knowledge of the binary base systems InN, GaN, and AlN, and to which extent alloys and heterostructures can be employed in the fabrication of optical electronic device structures[24,96]. GaN is the most studied group III-nitride compound, but InN and AlN have become increasingly significant due to their unique properties as low band gap and wide band gap materials, respectively.

At present, the most commonly utilized growth techniques for the production of group III-nitrides are organometallic chemical vapor deposition (OMCVD - also denoted as MOVPE) and molecular beam epitaxy (MBE)[97,98]. However, these low-pressure deposition processes are limited to a temperature range under which the partial pressures of the constituents do not differ vastly and decomposition processes can be countered by off-equilibrium conditions. These off-equilibrium conditions employed in MBE and organometallic CVD growth of InN require a relatively low growth temperatures in order to overcome the thermal decomposition pressures, thus limiting the quality of InN and

related group III-nitride epilayers[24,72-74]. In addition, these low growth temperatures require the application of extremely high V-III ratios in order to prevent the formation of metal droplets on the thin film surface. Recent studies pertaining to the decomposition of InN layers[99] have shown that oxygen is easily incorporated into the InN crystal under thermal treatments, and has been suggested as the source for the wide discrepancy in reports in the bandgap energy of InN. Controversial reviews of the present status of InN growth and characterization have been provided by Bhuiyan et al.[24] and Davydov et al.[75], implying that different approaches for the growth of In-rich group-III-nitride alloys need to be explored in order to improve the structural and optical properties of InN and related alloys.

Recent studies in the indium - nitrogen system[76] show much uncertainty in the p - T - x relations due to missing experimental validation. However, studies of the nitrogen pressure required to prevent thermal decomposition of bulk InN, provide a relationship given by

$$p(N_2) \rightarrow p_0 \exp\left[-\frac{\Delta H_r}{R}\left(\frac{1}{T} - \frac{1}{T_0}\right)\right] , \qquad (1)$$

which results in the $p\text{-}T^{-1}$ relation shown in Figure 6.1[48]. This relation indicates that for the pressure range $p_{N_2} \leq 10^2$ bar and substrate temperatures $\leq$ 900 K the surface decomposition of InN can be effectively suppressed.

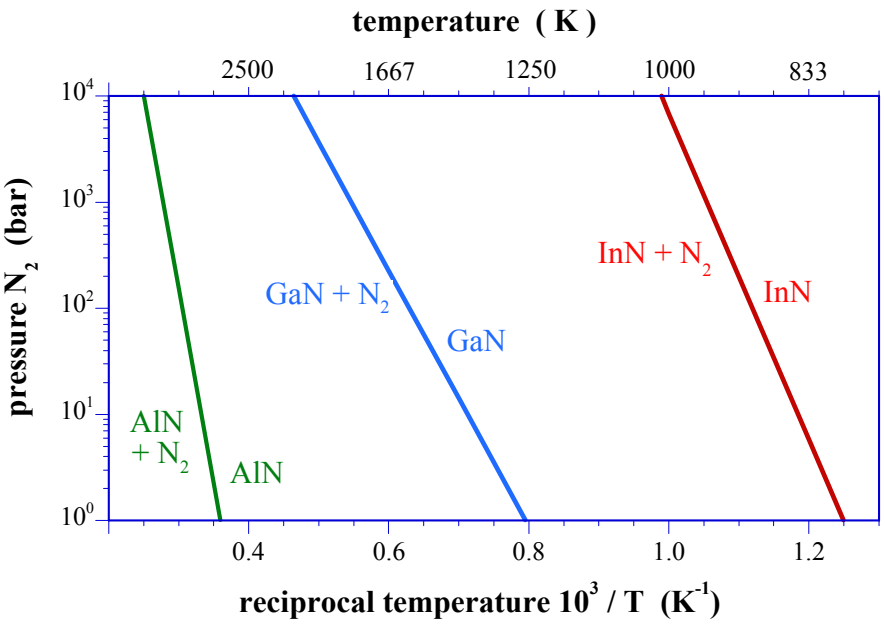

Figure 6.1: Thermal decomposition pressure vs. reciprocal temperature for AlN, GaN and InN[48].

The approach presented here explores the growth of indium-` rich group III-nitrides at elevated pressures using InN as a model system in order to demonstrate the capabilities of high pressure CVD. InN is the most challenging material system, since the equilibrium vapor pressure of nitrogen over InN is much higher compared to AlN and GaN[67]. A high-pressure flow channel reactor incorporating real time optical characterization capabilities[77,78,81,82] is utilized to study and optimize InN nucleation and growth. At above atmospheric pressures, optical diagnostic techniques are uniquely suited to provide real time information pertaining to gas flow dynamics in laminar and

turbulent flow regimes. Optical diagnostics are also utilized to obtain crucial information regarding precursor flow and decomposition kinetics. Several optical techniques have been explored, but only a few provide the required robustness and sensitivity. For example, the substrate temperature during InN growth under high pressure is between 800K and 1000K, resulting in a significant radiation emission, as shown in Figure 6.2. Even if modulation techniques are applied, the intensity of the emitted radiation from to the substrate heater limits the sensitivity of many optical probe techniques operating in visible and infra-red (IR) ranges. As depicted in the inset of Figure 6.2, the radiated intensity for a 1000K back body emitter vanishes very quickly below 350 nm, with negligible contributions below 300 nm.

Utilizing ultraviolet absorption spectroscopic (UVAS) techniques as well as UV induced fluorescence spectroscopy to identify the group-V and organometallic group-III precursors in the gas phase is well established in the literature[85-88].

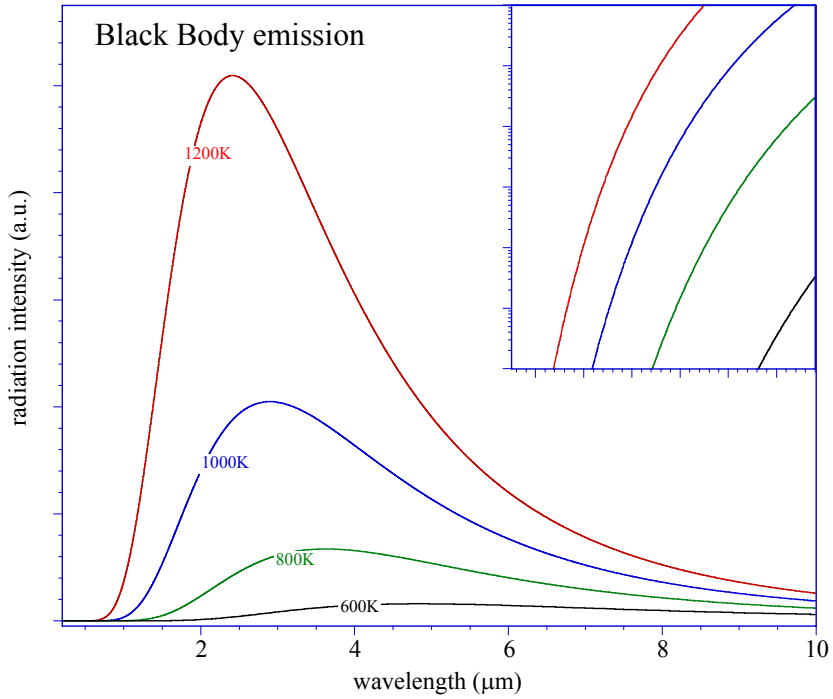

Figure 6.2: Intensities and spectral distribution of a black body emitter such as a hot substrate for different temperatures. In inset depict on a logarithmic scale the onset the radiation for 100K and 600K.

In the following sections, a brief introduction of the HPCVD reactor design is provided along with its real-time optical capabilities in order to characterize flow, gas phase and surface reactions. This is followed by three sections providing results on the optical characterization of the precursors trimethylindium (TMI) and ammonia (NH_3) and the optical monitoring of InN nucleation and overgrowth utilizing sequential precursor injection.

6.2 High-pressure reactor system

The growth of group III-nitrides at elevated pressures requires a completely redesigned OMCVD reactor system with special consideration directed towards flow kinetics, gas phase reactions, boundary layer diffusion and alteration of surface chemistry. This HPCVD reactor system utilizes a pulsed precursor injection technique, which is essential in order to achieve compression of the precursors to reactor pressure, minimization of gas phase reactions, optimization of nucleation kinetics, and analysis of gas phase and surface decomposition dynamics in real-time.

A symmetric arrangement of substrates in the upper and lower part of the flow channel is used, in order to prevent preferential material deposition on the opposite side of the heated substrate. As schematically depicted in Figure 6.3(b), optical access ports are integrated along the center axis of the substrates, which allows optical characterization of flow kinetics, gas phase reactions and the substrate surface through the back side. A more detailed description of the reactor design and the optical characterization capabilities is given elsewhere[78,100].

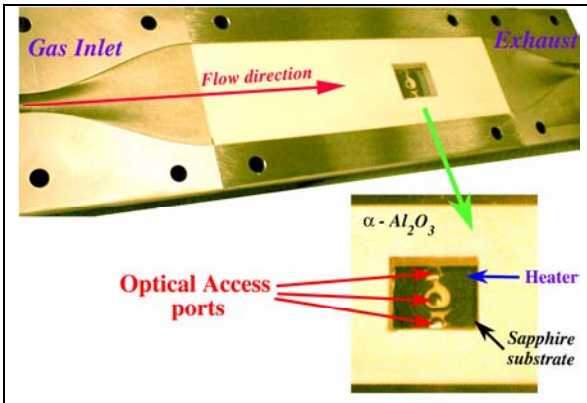

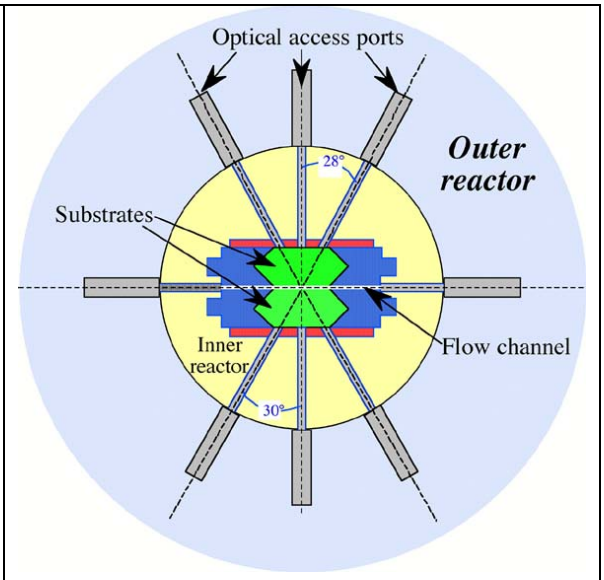

Figure 6.3(a): Half of the reactor flow channel assembly showing flow direction. The flow channel is designed with a constant cross sectional area for the maintenance of laminar flow. The sapphire substrate is seen along center axis of flow and is held in two α-Al_2O_3 plates. **Figure 6.3(b)**: Schematic cross section of the reactor containing the optical access ports and the center of the substrates. Two optical ports provide access to the flow channel and three ports in each of the two half sections of the reactor provide access to the growth surface.

The flow characteristics of the HPCVD reactor has been analyzed using laser light scattering, LLS, in a forward scattering geometry[90]. The onset of increased LLS scattering for pure nitrogen gas flow is summarized in Figure 4a, indicating the flow and pressure ranges at which laminar flow can be maintained. The associated Reynolds number can be calculated via

$$\text{Reynold's \#}\ \ Re = \frac{\rho u l}{\eta}, \qquad (2)$$

where $\rho = 1.12\ [\text{kg} \cdot \text{m}^{-3}]$ is the density of the gas, "u" the flow velocity, "l" a flow reactor characteristic length parameter, and $\eta = 1.8 \cdot 10^{-5}\ [\text{kg} \cdot \text{m}^{-1} \cdot \text{s}^{-1}]$ the dynamic

viscosity. For ideal gases, a direct proportionality between the density of the gas and the pressure exists, which for a constant "l" and η leads to a inverse proportionality between flow velocity and pressure. The calculated Reynolds numbers are shown in Figure 6.4(b) with an average around 1480. No significant pressure dependency is observed.

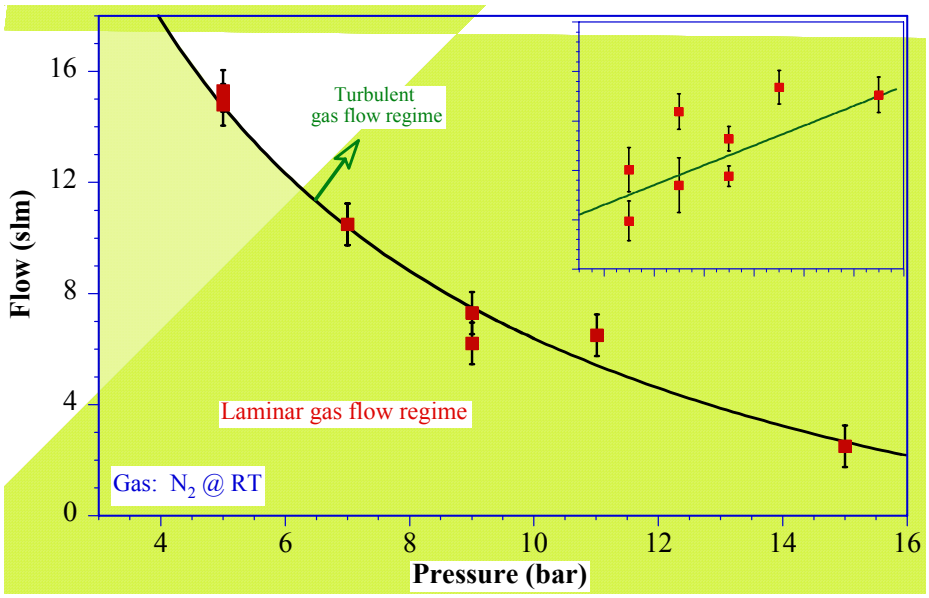

Figure 6.4(a): Transition from laminar to turbulent flow conditions as determined by LLS intensity measurements. The inset depicts the increase of the LLS with increasing pressure.

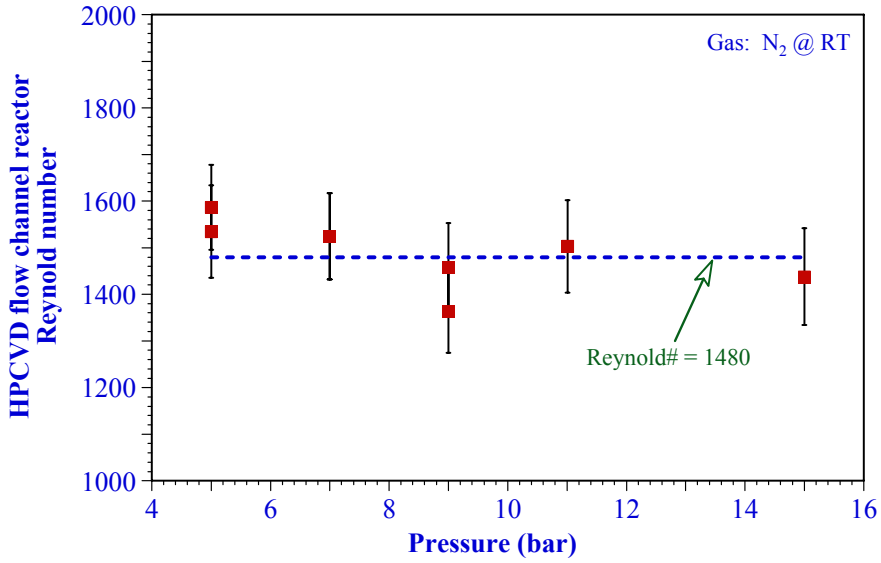

Figure 6.4: Calculated Reynolds numbers for HPCVD flow channel reactor with a cross section of A=50 mm^2.

6.3 Optical characterization of precursors and reactor flow characteristics

Transport of the TMI precursor from the bubbler to the gas flow control panel is achieved via a nitrogen carrier gas maintained at a temperature of 20ºC and pressure of 760 torr. The actual molar flow rate of TMI is calculated from standard partial pressure curves (provided by the manufacturer) and nitrogen carrier gas flow rates and can be expressed as

$$n_{TMI} = 8.3216 \cdot 10^{-9} \cdot x \qquad [mol \cdot s^{-1}] \qquad (3)$$

where x is the % full scale (%FS) setting of the carrier gas mass flow controller (100% FS = 500 sccm).

Initially, optical characterization of the TMI flux through the reactor flow channel is achieved under continuous flow conditions at near-atmospheric pressure, which does not require a compression stage. This carrier gas containing diluted TMI is combined with the main reactor nitrogen flow in the gas flow control panel and is directed to the reactor flow channel. The molar TMI:N_2 flow ratio χ through the reactor can be expresses as

$$\chi = \frac{n_{TMI}}{n_{total}} = \frac{n_{TMI}}{n_{Main\_N_2} + n_{bubbler\_N_2} + n_{TMI}} = \frac{2.237 \cdot 10^{-5} \cdot x}{z + 10^{-2} \cdot x + 2.237 \cdot 10^{-5} \cdot x} \qquad (4)$$

where x and z are the percent full scale flow settings of the TMI carrier gas and main reactor N_2 mass flow controller settings, respectively.

The absorption of ultraviolet light as a function of TMI concentration has been characterized between 190 nm and 500 nm. A broad absorption feature in the

wavelength range of 190nm - 250nm is observed at room temperature (RT) with the absorption peak centered at 210.7 nm. Figure 6.5 shows the spectrally resolved absorption structure as a function of TMI carrier gas flow settings. For higher carrier gas flow settings, two absorption features centered at 210.7 nm and 221 nm can be observed. The center location of the strongest absorption feature remains constant at 210.7 nm for all TMI concentrations investigated. The maximum absorption and Full-Width-Half Maximum (FWHM) of this feature are shown in Figure 6.6 as function of the TMI carrier gas mass flow controller setting while maintaining a reactor pressure of 1.6 bar and a total flow of 5 slm through the reactor. Analysis of this absorption feature provides a correlation between measured the absorption maxima and the TMI carrier gas flow setting, which can be expressed as $\alpha_{(x=\%FS)} = 1.72 \cdot 10^{3}$ [cm^{-1}].

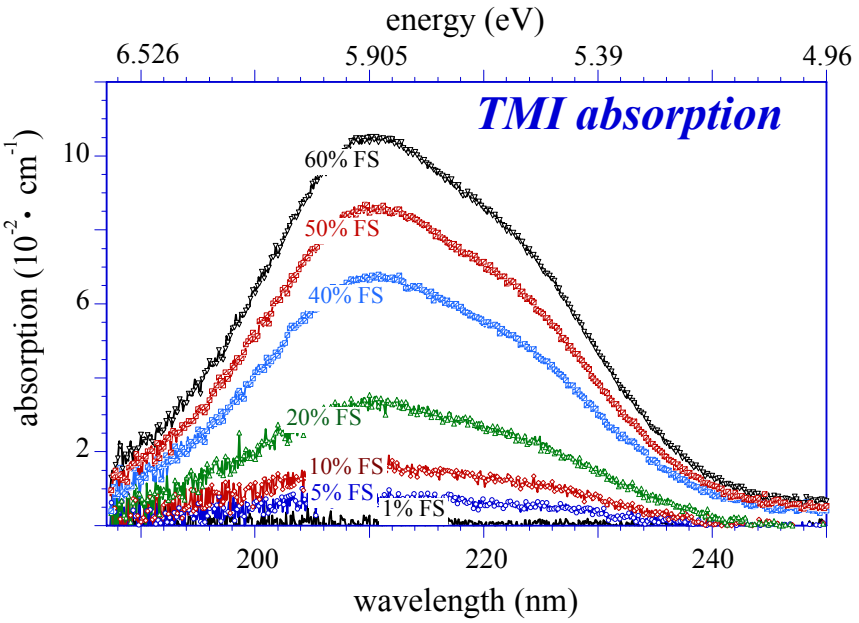

Figure 6.5: Spectrally resolved absorption on TMI diluted in N_2-carrier gas as function of N_2-flow through TMI bubbler in %FS. The total flow through the reactor is maintained at 5 slm at 1630 mbar.

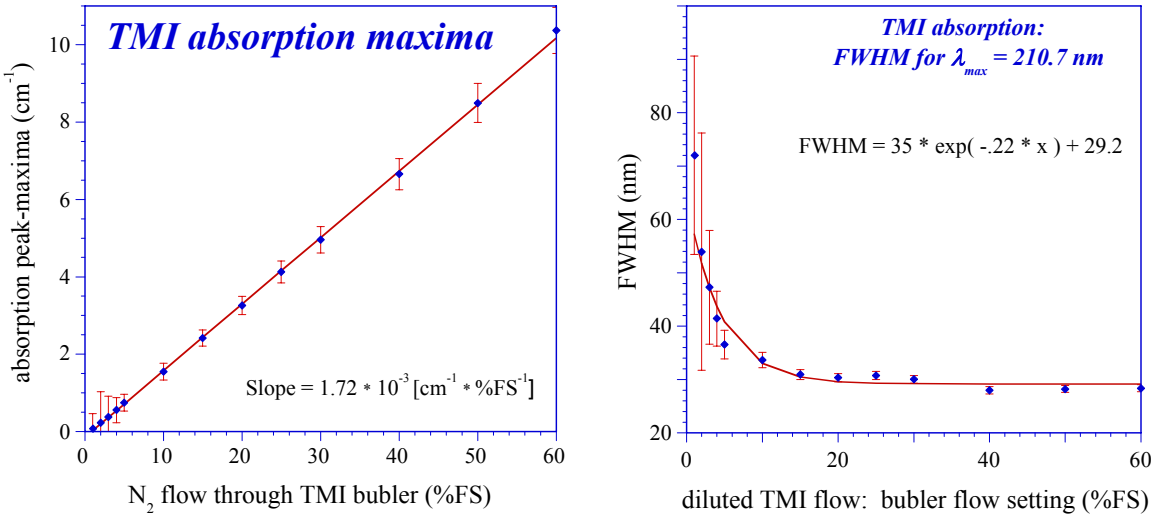

Figure 6.6a: Absorption strength at λ=210.7 nm as function of N_2 carrier gas flow through TMI bubbler in %FS. **Figure 6.6b:** FWHM for the absorption maximum at 213.5 nm.

Further analysis of the influence of the molar TMI flow ratio χ on this peak absorption maximum centered at 210.7 nm reveals an exponential relationship in the form of

$$\alpha_{(\chi)} = - 0.37367 + 0.37282 \cdot e^{\frac{\chi}{5.44 \cdot 10^{-4}}} \quad [cm^{-1}] \qquad (5)$$

which is depicted in Figure 6.7.

The combination of Equations 4 and 5 allow for real-time calculation of the flux of TMI molecules per unit time based on the observed ultraviolet absorption based upon

$$N_{TMI} = \frac{10^{18} \cdot y \cdot \left(\ln(\alpha') - 2.28 \cdot 10^{-3} \right)}{8.21 - 2 \cdot \ln(\alpha')} \qquad (6)$$

where $\alpha' = \frac{\alpha + 0.37367}{0.37282}$ [cm^{-1}] and y is the %FS setting of the main nitrogen reactor flow. This result is used in the following section to compute the number of TMI molecules contained in a single pulse during TMI injection.

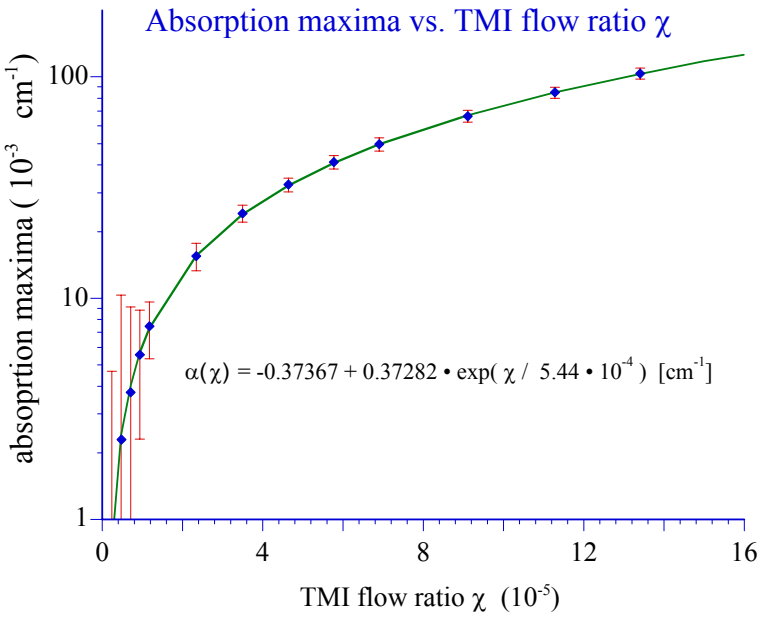

Figure 6.7: Correlation of TMI absorption maximum and molar TMI flow ratio χ under steady-state flow conditions.

6.3.1 Optical characterization of pulsed TMI injection, diluted in N_2-carrier gas

In order to grow InN at above atmospheric pressures, a two step process is employed for the injection of the precursors in to the HPCVD reactor flow channel. Initially, a 75 cm^3 reservoir at atmospheric pressure is filled with TMI diluted in N_2 carrier gas. In the second step, the reservoir is compressed by high pressure nitrogen and injected into the main nitrogen flow. The filling of the reservoir, subsequent compression and injection in to the reactor, denoted as 'cycle sequence', is continually repeated. The

cycle repetition rate, duration of the injection, as well as the temporal position of injection within a given cycle sequence are process parameters that are used to control gas phase reactions and the film growth process itself.

Figure 6.8 shows real-time traces of the transmitted intensity monitored at 210.7 nm during pulsed TMI injection with a 6 sec repetition rate for various TMI carrier gas flow rates. The reactor pressure is maintained at 1.6 bar with a total flow of all gases (TMI carrier gas and nitrogen main flow) through the reactor maintained at 5slm. From the transmitted intensity traces, the associated absorption is computed, which can then be correlated to the molar TMI concentration contained in the each injected pulse.

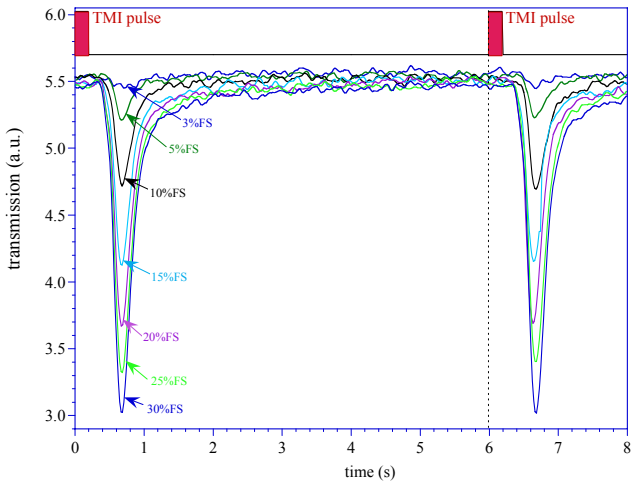

Figure 6.8: Transmitted intensity trace monitored at 210.7 nm during TMI precursor pulse injection in the reactor at 1.6 bar and a total flow through the reactor of 5slm. The TMI flow was varied from 15 – 150 sccm (3 - 30%FS). The cycle sequence is 6 s with a 0.2 s TMI pulse width.

Figure 6.9 shows a typical trace for the absorption at 210.7 nm and the computed number of TMI molecules contained in the pulse. Analysis indicates that the sensitivity limit for TMI concentrations is on the order of 10^{14} TMI molecules per time unit depending on the reactor pressure and total flow rate.

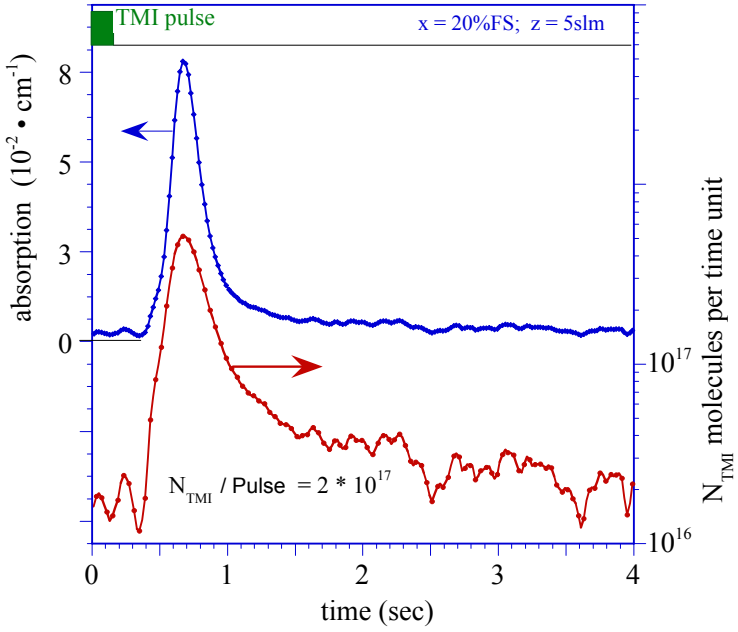

Figure 6.9: UV Absorption due to and concentration of TMI atoms (N_{TMI}) per unit time during pulsed TMI injection.

6.3.2 Optical characterization of ammonia (NH_3) precursor

Detailed characterization of the NH_3 flow dynamics and gas phase kinetics of NH_3 under HPCVD conditions has been previous published[30]. However, a brief summary of the characterization capabilities and analysis of the kinetics of NH is presented here. Similar to section II, the optical characterization of NH_3 is treated separately for

continuous NH_3 flow and pulsed NH_3 injection. Under both continuous and pulsed flow conditions, the NH_3 vapor is transported from a NH_3 gas cylinder, which is regulated to deliver gas at 30psi. An in-line filter is utilized in order to lower the concentrations of trace contaminants such as oxygen and water. Similar to the TMI flow analysis, the molar flow rate of NH_3 can be expressed as

$$n_{NH_3} = 7.4405 \cdot 10^{-6} \cdot y \quad [mol \cdot s^{-1}]. \qquad (7)$$

where y is the %FS scale setting of the NH_3 mass flow controller (100% FS = 1 slm). Under continuous flow conditions, the molar ammonia flow ratio χ through the reactor can be expressed as

$$\chi = \frac{n_{NH_3}}{n_{total}} = \frac{n_{NH_3}}{n_{Main\_N_2} + n_{NH_3}} = \frac{y}{50 \cdot z + y} \quad (8)$$

where y and z are the % full scale settings of the NH_3 and main nitrogen mass flow controllers, respectively (100% FS(z) = 50 slm)

The flow of ammonia through the reactor has been characterized by UVAS in the wavelength range of 180 nm and 300 nm. Significant, concentration dependent absorption features are observed in the wavelength range of 190 nm to 240nm. These absorption features are shown in Figure 10 for various NH_3 mass flow controller settings with a 5slm nitrogen main reactor flow of and a reactor pressure of 1.6 bar. The characteristic absorption features match previously reported data in literature[92,93]. The molar ammonia flow ratio χ required for the growth of InN is sufficiently high that several of the absorption lines are "saturated" at their peak value.

For ammonia flow ratios in the range of $\chi = 1.0 \cdot 10^{-2}$ - $1.6 \cdot 10^{-1}$, the absorption feature centered at 221.6 nm is used in order to correlate the observed absorption and the NH_3 flow ratio χ through the reactor flow channel, as shown in Figure 6.11. Analysis of this absorption feature, reveals the following relationship:

$$\begin{aligned} \alpha_{peak\_217.1nn}(\chi) &= 0.38 \cdot \ln(\chi + 0.011) - 2.0 \cdot \chi + 1.73 \quad [\mathrm{cm}^{-1}] \\ \alpha_{peak\_221.6nn}(\chi) &= -45 + 45.01 \cdot \exp\left(\chi / 18\right) \cdot 10^{-2} \quad [\mathrm{cm}^{-1}] \end{aligned} \tag{9}$$

between the UV absorption and ammonia ratio □.

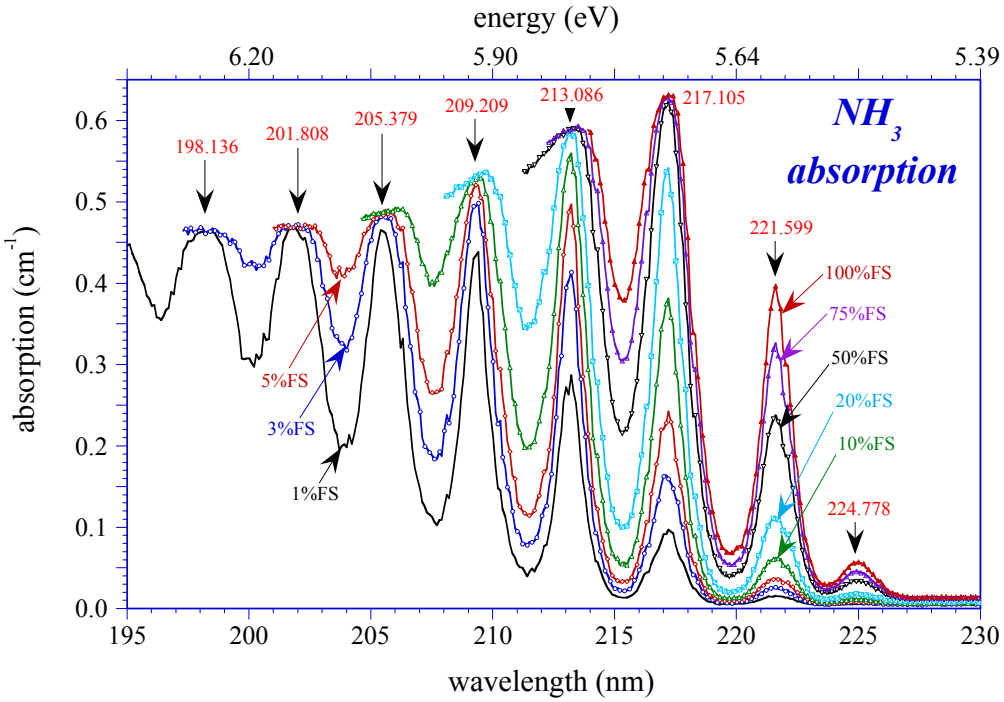

Figure 6.10: Absorption spectra for various ammonia flows in %FS of the NH_3 mass flow controller diluted in 5 slm nitrogen main flow and a rector pressure of 1.6 bar.

The number concentration of NH_3 molecules per unt time can be computed as a function of the observed absorption. Considering the absorption feature at 221.6 nm, we find the NH_3 number concentration can be expressed as a function of the absorption α by

$$N_{NH_3}(\lambda=221.6\text{nn}) = \frac{7.17 \cdot 10^{21} \cdot z \cdot \ln(\alpha')}{1 - 32 \cdot \ln(\alpha')} \quad [s^{-1}] \quad \text{with } \alpha' = \frac{\alpha_{@\ 221.6nn} - 80}{80.01}. \quad (10)$$

The number concentration of NH_3 determined from Eq. 10 (□ = 221.6 nm) is plotted in Figure 6.17b for NH_3 mass flow controller settings between 1% and 50 %FS while

maintaining a main reactor flow rate of 5 slm and a reactor pressure of 1.6 bar. Under continuous flow conditions, the ammonia concentration can be varied between 10^{19} and $2*10^{20}$ NH_3 molecules/sec.

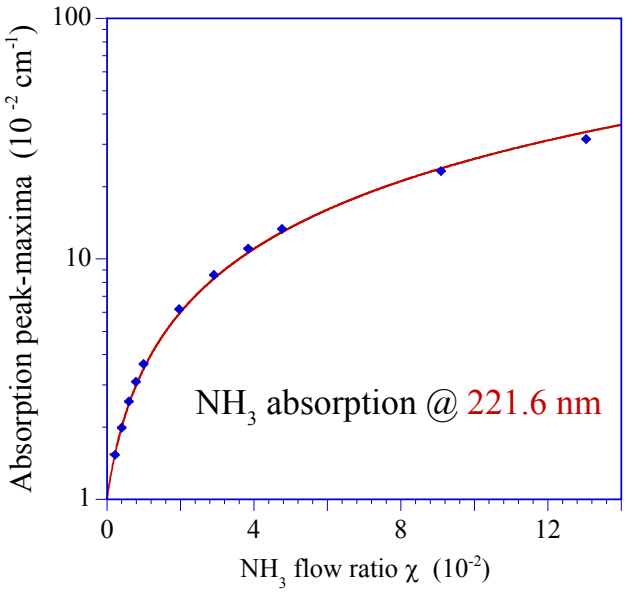

Figure 6.11: Ammonia absorption monitored at $\lambda = 221.6$ nm as function of ammonia flow ratio χ under steady state flow conditions for a reactor pressure of 1.6 bar.

6.3.3 Optical characterization of pulsed ammonia injection

The flow of ammonia at higher pressures requires a compression and dilution stage in order to enable the injection of ammonia into the HPCVD reactor flow channel. As in the injection of the TMI precursor, a 75 cm^3 reservoir is filled at slightly above atmospheric pressure with ammonia gas, controlled by a mass flow controller (MFC) and

a computer controlled filling time. In the following step, the reservoir is compressed with high pressure N_2 up to the reactor pressure and injected into the reactor. Cycle repetition rate, duration of injection, and the position of injection can the adjusted with an accuracy of 1 msec.

Depending on the ammonia concentration per pulse injected into the reactor, several absorption features can be utilized to characterize and analyze the ammonia pulses. Figure 6.12 shows typical absorption traces monitored at 221.6 nm during pulsed ammonia injection with a 6 sec total cycle sequence time for various ammonia mass flow controller settings. The reactor pressure was maintained at 1.6 bar with a total gas flow through reactor at 5 slm.

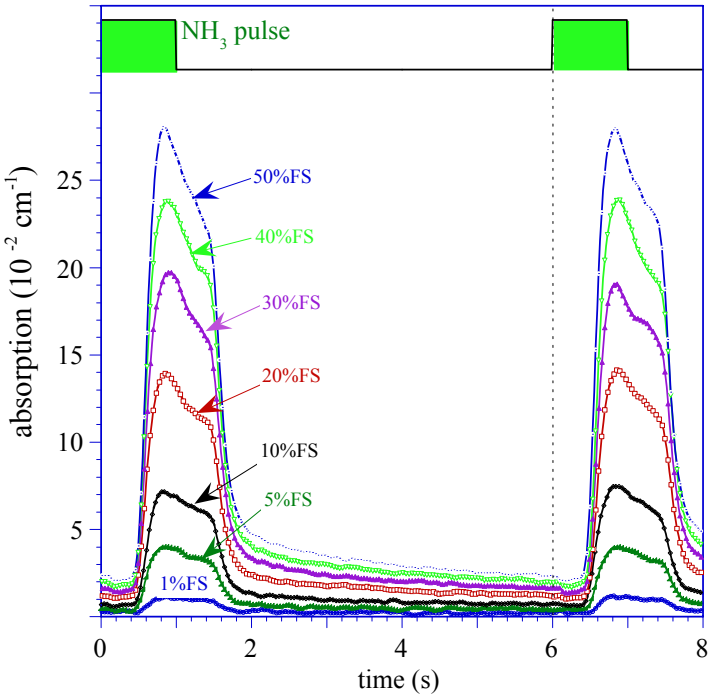

Figure 6.12: Ammonia absorption traces monitored at $\lambda = 221.6$ nm for 1.0 sec NH_3 pulses injected 6 sec apart.

The relationship between the absorption strength and ammonia number concentration provided by Eq. 10, together with the reservoir compression ratio and volume, the total number of ammonia molecules per pulse can be calculated.

The pulsed ammonia injection has been analyzed as function of pulse width, ammonia concentration per pulse, total reactor flow and reactor pressure. Figure 13 shows the monitored absorption traces λat λ=221.6 nm for various reactor pressures, while maintaining a total gas flow through the reactor at 5 slm and ammonia flow of 200

sccm. It is important to note that for pressures above 10 bar, a carryover of ammonia from one cycle to the next is observed, resulting in an increase in the base line absorption of the overall absorption observed in the reactor flow channel.

Similar to the characterization of pulsed TMI injection, the pulsed ammonia injection monitored at the substrate center line shows three distinct features. These pressure dependent features are 1) a systematic shift in the pulse arrival time 2) a systematic ammonia pulse broadening and 3) a change in the NH_3 absorption cross section for pressures larger 8 bar. These features have been analyzed in detail and are published elsewhere[30].

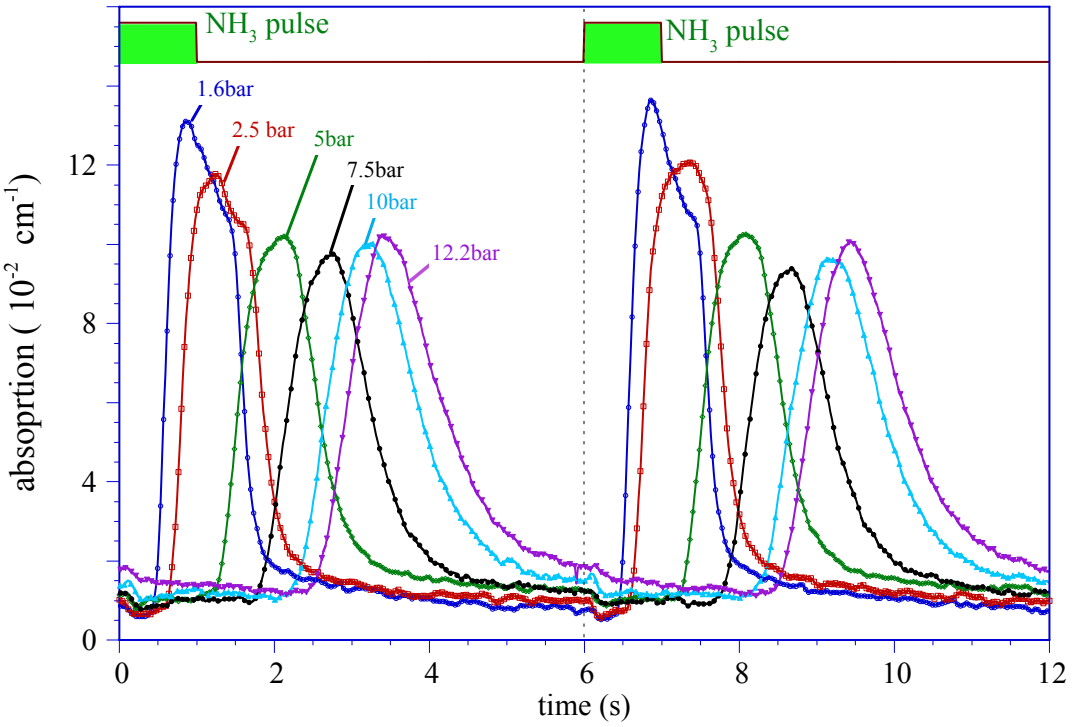

Figure 6.13: Absorption traces monitored at $\lambda = 221.6$ nm for 1 sec NH_3 pulses injected 6 s apart. The reactor main flow and the ammonia flow were kept constant at 5 slm nitrogen and 200 sccm, respectively.

6.4 Decomposition dynamics of TMI and ammonia precursors

The decomposition dynamics of ammonia has been analyzed in the temperature range of 300K to 1200K under continuous ammonia flow conditions at a reactor pressure of 1.6 bar. Figure 6.14 shows the temperature dependence of ammonia spectra recorded between 180 nm and 230 nm for a molar ammonia flow ratio $\chi = 4 \bullet 10^{-3}$. The increase of

the nitrogen absorption base line as function of the temperature has been accounted for. The spectroscopic scan between 180 nm and 400 nm revealed no new absorption feature that could be associated with ammonia fragments at higher temperatures.

Above 990K, a significant reduction in the absorption strength is observed, indicating the onset of the decomposition of ammonia in the reactor flow channel. The change in the absorption peak maxima as a function of temperature as is shown in Figure 15a for a molar ammonia flow ratio χ of 10^{-2}.

The absorption peak maxima increase as the temperature raises due to the change in the absorption cross-section. Above 900K, a plateau is observed with a strong fall-off above 1100K. The decomposition dynamics at higher reactor pressures were studied during pulsed ammonia injection as a function of temperature, as depicted in Figure 6.15b. Starting around 850K, a falloff in the peak absorption amplitude can be observed, which is at a slightly lower temperature as observed at 1 bar reactor pressure and the same total flow. Since the gas flow velocity in the reactor system decreases inversely with pressure, an additional temperature effect due to the reduced gas velocity at higher pressures must be considered.

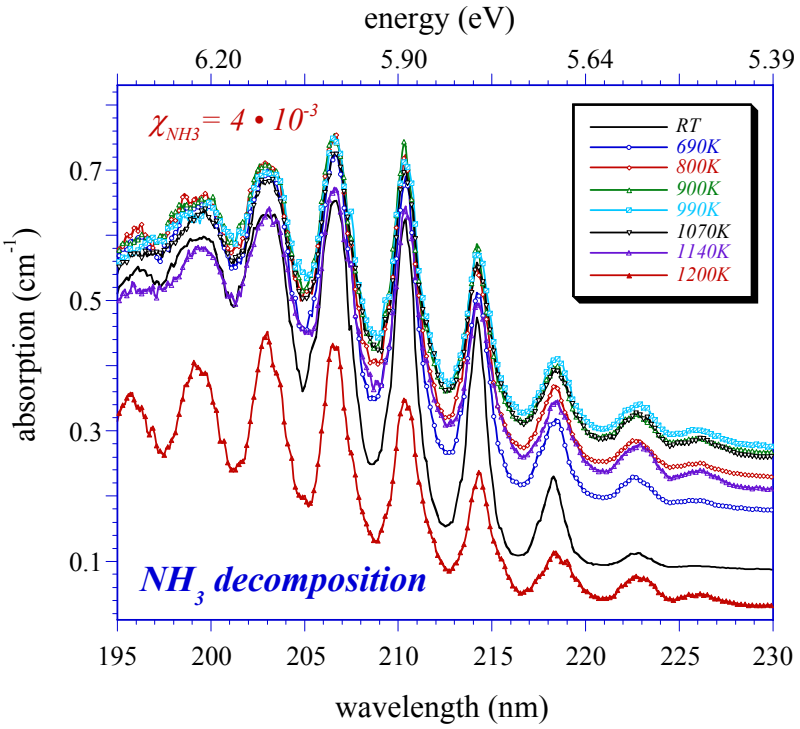

Figure 6.14: Ammonia absorption spectra taken at different temperatures during steady state flow conditions for a reactor pressure of 1.6 bar.

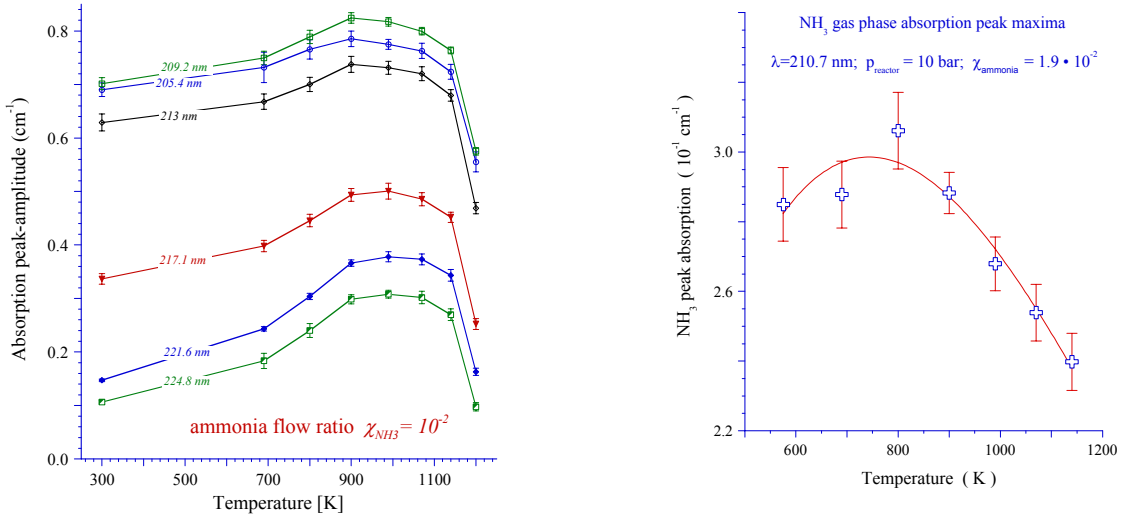

Figure 6.15a) Change of the ammonia absorption peak maxima as function of temperature. **Figure 6.15b)** Decomposition of ammonia during pulsed precursor injection at a reactor pressure of 10 bar.

The decomposition dynamics for TMI were studied only for pulsed TMI injection at higher reactor pressures, in order to avoid the formation of atomic indium on the windows at higher temperatures. Figure 6.16 shows the observed changes in the amplitude of peak maximum absorption at 210.7 nm. The onset of TMI decomposition in the gas phase occurs around 800K, which is slightly higher than those reported under low-pressure OMCVD conditions[86,95] for the growth of group In-V compounds[93,94].

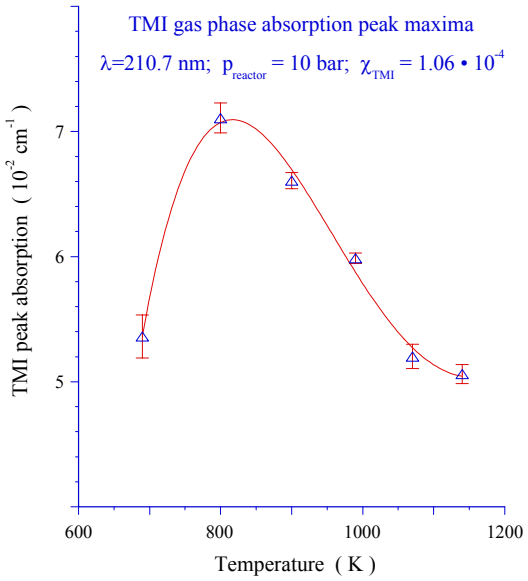

Figure 6.16: Decomposition of TMI at 10 bar reactor pressure, monitored during pulsed TMI injection as function of temperature.

6.5 Real-time optical characterization of InN growth: nucleation and overgrowth

An understanding of the decomposition kinetics of precursors utilized in OMCVD growth techniques is crucial to precise engineering of both nucleation and subsequent film growth. Detailed modeling of the expected precursor flow dynamics and chemical kinetics under HPCVD conditions has been previously published[15]. The decomposition studies for ammonia in the previous section suggest temperatures above 1000K are required for sufficient cracking of the ammonia precursor for the growth of InN. However, literature data for InN growth by OMCVD indicate a growth temperature of 675K to 750K[25], 775K[26], 810k-840K[24]. Under HPCVD conditions, we can expect to be able to increase the growth temperature about 50K -100K higher than possible at low-

pressure OMCVD conditions. However, this still leaves a temperature mismatch between optimum ammonia decomposition and optimal InN growth temperature, which remains a challenge to be solved. For low-pressure OMCVD growth techniques, TMI:NH_3 ratios of $1:10^4$ and larger[24.25] are required to counteract the low ammonia decomposition rate at optimum growth temperatures.

Here, the growth of InN is achieved by exposing the substrate surface to pulses of TMI [$In(CH_3)_3$] and ammonia [NH_3] at 800 K - 1050 K. The symmetrically embedded sapphire crystals with a (0001) growth surface are heated to 1150K and exposed to ammonia for typically 30 min. After the nitrification of the sapphire surface, the temperature is lowered to the growth temperature, and the InN growth is initiated.

The growth of InN is initiated by supplying pulses of the precursors that are sequentially separated by pauses as shown schematically in Figure 6.17. As discussed in the previous sections, the TMI and NH_3 pulses are temporally controlled and embedded in a nitrogen gas main flow through the reactor. The total flow through the reactor as well as the reactor pressure are kept constant.

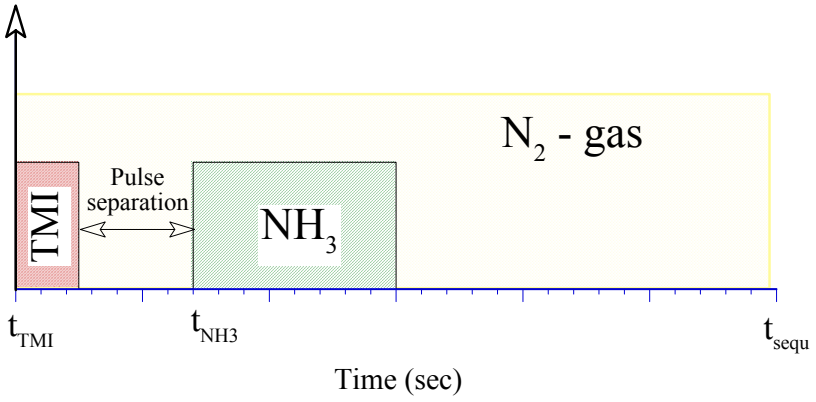

Figure 6.17: Schematic representation of a precursor cycle sequence used for the growth of InN via the precursors TMI and ammonia.

This growth at elevated-pressures has an extended growth parameter space as compared to low-pressure organometallic chemical vapor deposition (OMCVD). Growth parameters that need to be evaluated are reactor pressure, average gas velocity, TMI and ammonia pulse separation and reaction time, the molar TMI to ammonia, $R_{TMI:NH_3}$ and growth temperature.

This large parameter space requires the application of real-time optical monitoring techniques in order to access the nucleation and growth conditions and in order to optimize the growth parameters. For monitoring InN nucleation and growth, single wavelength principal angle reflectance (PAR)[100] and laser light scattering (LLS) is applied, employing a p-polarized light λ beam (λ=6328Å) and a Glan-Thompson prism. The beams impinge on the substrates at an angle of incidence ϕ=30° and ϕ=28° for the upper and lower part, respectively. The reflected beams are detected by Si photodiodes.

The intensity of the scattered radiation is monitored simultaneously by a photo multiplier tube (PMT) located perpendicular to the plane of incidence.

PAR is based on the same principle as p-polarized reflectance spectroscopy[27-30]. However, PAR utilizes p-polarized light impinging the substrate-ambient interface near the principal angle ϕ_P. corresponding to the pseudo-Brewster angle ϕ_B for p-polarized light impinging the ambient-substrate interface. Depending on the substrate temperature and laser wavelength, the principal angle ϕ_P. varies from 27.5 deg to 30 deg for the sapphire - ambient interface[100]. The angle of total reflection, ϕ_T, is approximately 5 deg above ϕ_P.

Figure 6.18 shows the PAR trace recorded for the wavelength λ=6328 Å, during InN growth. Superimposed on the interference oscillations of the reflected intensity is a fine structure that is strongly correlated to the time sequence of the supply of precursors employed. Each peak in the fine structure corresponds to a complete precursor cycle sequence.

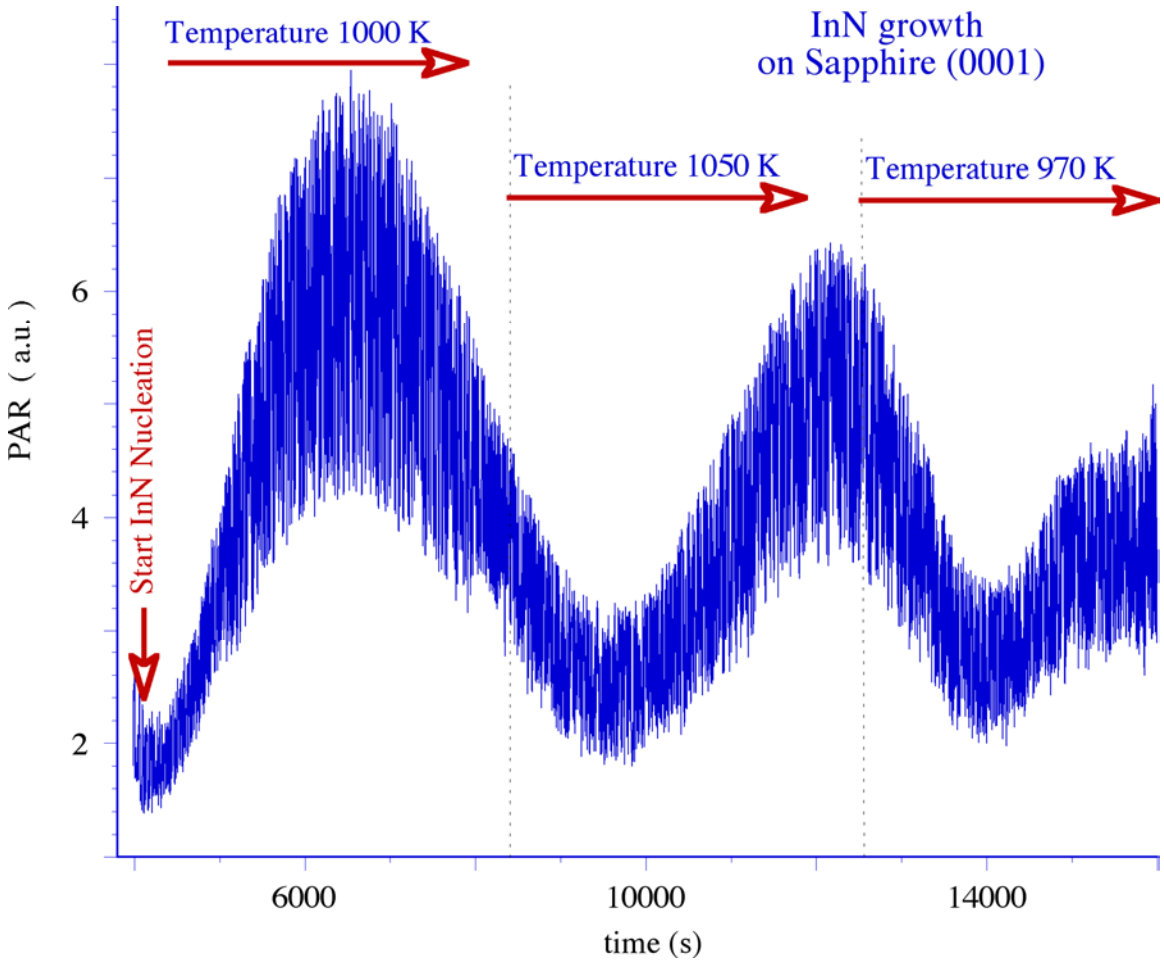

Figure 6.18: Monitoring of InN growth by PAR for 2.5 interference fringes. The inset shows a section of the InN layer (approx. 380 nm) deposited on a sapphire (0001) substrate.

Figure 6.19 shows typical observed PARS and UVAS monitored during nucleation on InN. The lower trace shows the UVAS trace recorded for the wavelength λ=210.8 nm, monitoring the un-decomposed ammonia and TMI species above the growth surface. The PAR trace in the upper half of the Figure is recorded for the wavelength λ=6328 Å, monitoring with high sensitivity the changes in the dielectric function of the

substrate-ambient interface. Also indicated are the positions of the pulsed precursor injection with a total cycle sequence time of 6 sec. Note that the precursor injection time and the response seen in UVAS and PAR are temporal shifted according to the average gas velocity in the reactor which is a result of the time lag between the opening of the injection valve and the arrival of the precursors at the centerline of the substrate in the reactor flow channel.

Prior to growth, the surface is exposed only to pulses of ammonia. The growth of InN is initiated with the first TMI pulse at 58 sec followed by an ammonia pulse 1.4 sec later. Figure 20 clearly shows the time delay of the pulses from the injection point until they reach the centerline of the substrate. About one to two cycle sequences elapse before the UV absorption trace of TMI is clearly observed (see arrows). The PAR signal shows a large jump after the ammonia pulse reaches the substrate, indicating the start of nucleation of InN and the present of TMI fragments in the surface vicinity. During the first few growth sequence cycles, the PAR signal shows growth related oscillations that are not well developed. The growth temperature is 990K, a reactor pressure of 10 bar, a total flow of 5 slm, and a molar ratio TMI to ammonia, $R_{TMI:NH_3}$ of 1:500.

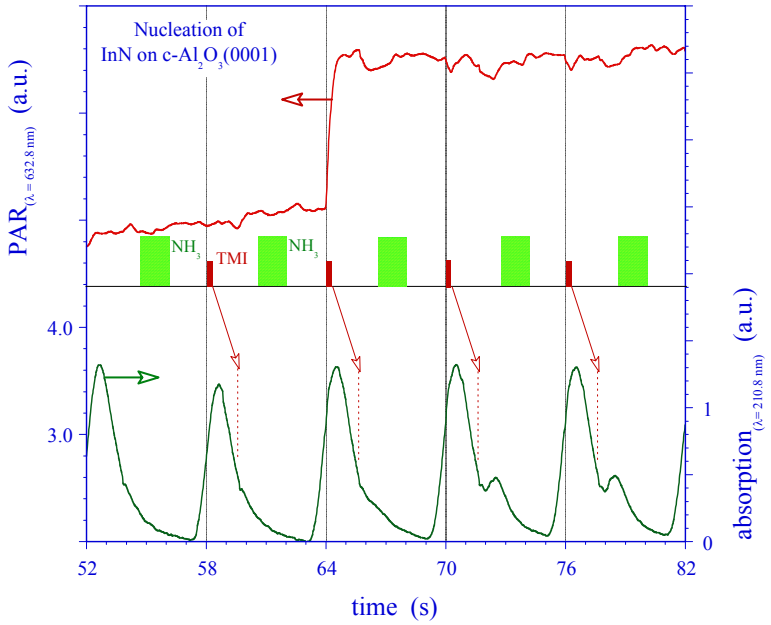

Figure 6.19: Monitoring of InN nucleation by PAR and UV absorption. A precursor cycle sequence of 6 sec with 0.4 sec TMI and 1.4 sec ammonia pulses, separated by 1.4 sec were used.

Steady state surface chemistry is reached after 5 to 20 cyclic precursor injections, depending on substrate temperature, precursor flow ratio, gas phase velocity and reactor pressure. As depicted in Figure 6.20, a periodic modulated PAR signal is observed under steady-state growth conditions where the signatures found in the PAR signal can be directly correlated to the present of ammonia an TMI fragments in a surface layer and at the growth surface. The overall decrease in the PAR signal intensity correlates to the InN growth per cycle sequence as discussed in detail for p-polarized reflectance[29]. The signatures observed in UV absorption trace coincide with the PAR response, even though the nature of these responses is different.

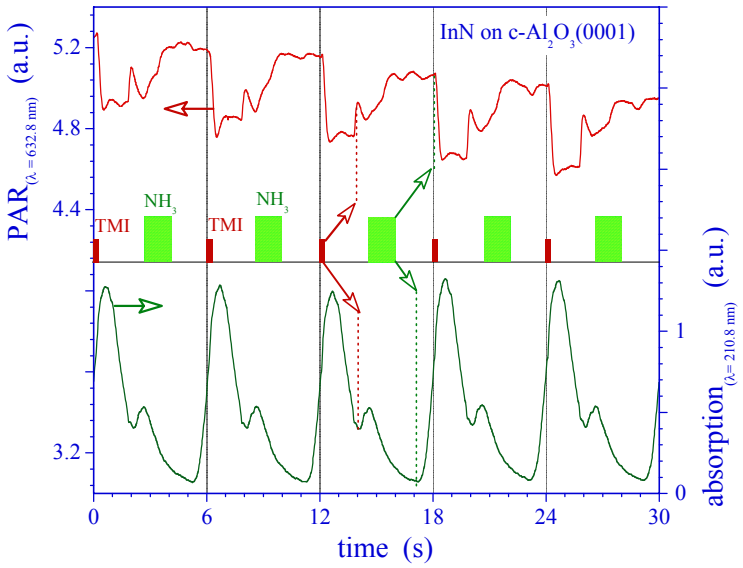

Figure 6.20: PAR and UV absorption traces during steady-state InN growth at 990K. The rector pressure was 10 bar with a total flow of 5 slm. The overall decrease in the PAR signal corresponds to InN growth.

As the temperature is lowered from 940K to 840K, the amplitude of the growth related PAR (not shown) signal becomes smaller and less pronounced. At 840K the growth related features indicate no growth due to inefficient decomposition of ammonia and TMI in the gas phase and surface reaction layer. This result agrees with the decomposition dynamics shown in Figure 6.15 for ammonia.

Monitoring the PAR, LLS and UVAS responses during various growth conditions provides crucial information on the gas phase decomposition dynamics of the precursor and the subsequent diffusion through the surface boundary layer to the growth surface. The establishment of an optical data base as function of reactor pressure, flow velocity,

molar III:V ratio and growth temperature will provide the base for a more detailed understanding on the dissociation of the precursors ammonia and TMI and of reaction rate constants for growth of InN as theoretical predicted by Cardelino et al.[82].

6.6 Ex-Situ InN Layer Characterization

The structural properties of epitaxially grown InN films have been investigated using x-ray diffraction. Figure 6.21 shows typical XRD spectra recorded in the □ - 2θ mode for samples #22L, #24L and #25L. These samples were grown at a temperature of 850 °C with a reactor pressure of 11 bar and average gas flow velocity of 45 cm/s. The precursors ratio, $R_{NH3:TMI}$, for samples #22L, #24L and #25L was set at 8000, 1000 and 410, respectively, Sample #22L shows a broad reflection from wurtzite-type InN centered at 31.26 deg with a full width at half maximum (FWHM) of 650 arcsec. This indicates a structural quality that is equivalent to InN thin films grown on GaN/AlN buffer layers, which have been produced by MBE growth methods[31]. As the precursor ratio $R_{NH3:TMI}$ is lowered from 8000 to 1000 (sample #24L) the InN (002) reflection broadens and shifted lower to 31.2 deg. In addition, the InN (101) reflection centered at 31.1 deg becomes more pronounced. For $R_{NH3:TMI}$ at 200 (sample #25L), both the InN (002) and InN(101) reflections show double structures, indicating the existence of additional InN related phases with FWHM less than 200 arcsec in very close proximity.

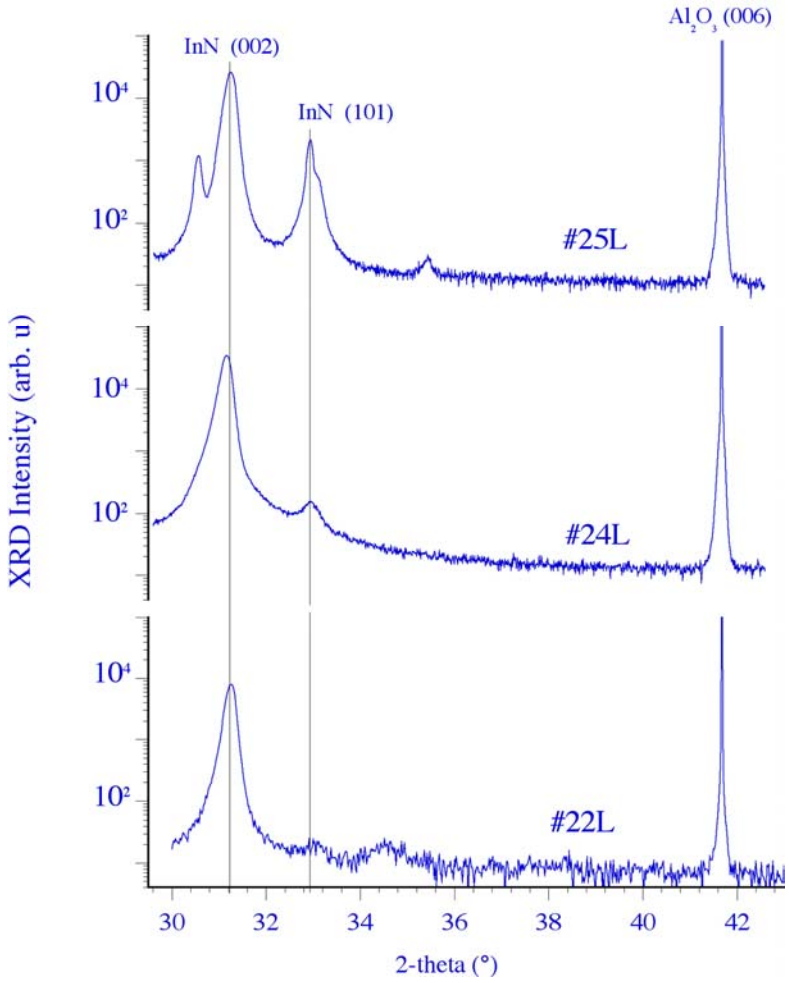

Figure 6.21: Results of XRD measurements of InN on Sapphire (0001). Precursor flow ratio, $R_{NH3:TMI}$, employed during growth of samples #22L, #24L and #25L was 8000, 1000 and 200, respectively

Analysis of the spectra for samples #22U and #25L reveal the lattice constants a = 3.557 Å and c = 5.754 Å. These values are in close proximity to previous reported lattice constants for high quality InN[32]. It is important to note, however, that the asymmetric line

suggest the existence of additional phases in close proximity to the main InN reflections, the origin of which is presently under investigation.

Figure 6.22 shows the optical absorption spectra in the energy range from 3 eV to 0.5 eV for a set of typical InN thin films grown under HPCVD conditions. For all samples shown, the layers were grown at a reactor pressure of 15 bar, a gas flow velocity of 50 cm/s and temperature of 850 °C. The precursor flow ratio $R_{NH3:TMI}$ was maintained at 3900, 2800, 1000 and 420 for samples #31L, #37U, #24L and #30L, respectively. Note that all samples, regardless of $R_{NH3:TMI}$ exhibit an absorption feature centered at 0.63 eV. This feature has been attributed to plasmon excitations in the conduction band[33] due to a large free carrier concentration. Since this feature remains unchanged in position and strength, our data suggest that the absorption edge shift towards lower energies is not directly related to the free carrier concentration, but rather to stoichiometry variations in InN.

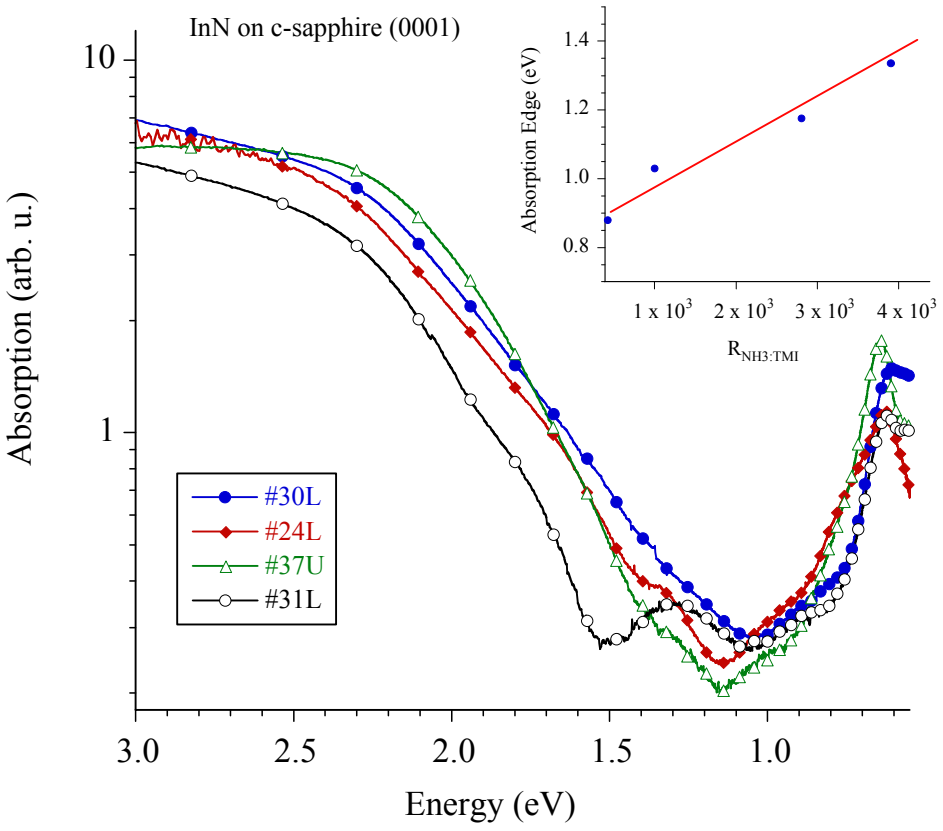

Figure 6.22: Absorption Spectra for characteristic InN samples grown with different ammonia to TMI ratio. The inset shows the absorption band edge as a function of ammonia to TMI precursor flow ratio.

The large variation in the absorption structures exhibited by these samples suggest that the observed absorption shift from approximately 1.3 eV to 0.83 eV are governed by a series of absorption structures centered at 0.87 eV, 1.1 eV and 1.3 eV. Numerical analysis of these features has been used to examine the dominant absorption band edge

beginning at 2.5 eV as a function of the $R_{NH3:TMI}$, the results of which are shown in the inset of Figure 22. The correlation between optical absorption edge shift and the precursor flow ratio $R_{NH3:TMI}$ indicated a close correlation between the precursor flow ratio and film stoichiometry.

6.7 Conclusion

The growth of epitaxial InN layers by *High-Pressure Chemical Vapor Deposition* has been explored in the laminar flow regime, evaluating the growth parameter for reactor pressures in range of 10 to 15 bars, gas flow velocities from 20 to 50 $cm*s^{-1}$, and molar ammonia to TMI ratios between 400 to 8000. The flow and decomposition kinetics of the precursors ammonia and TMI have been studied by ultraviolet absorption spectroscopy under pulsed precursor injection. UVAS, principal angle reflectance (PAR), and laser light scattering (LLS) have been applied to study the growth of epitaxial InN layers under high-pressure chemical vapor deposition conditions. As demonstrated, the combination of UVAS, PAR and LLS allow the characterization of gas phase chemistry as well as highly sensitive studies of surface processes during InN nucleation and steady-state InN growth, which will be essential for engineered nano-scale device structures. The link between the surface sensitive PARS response to the real-time gas phase analysis (UVAS) will enable the formulation of a comprehensive growth model, providing crucial insights in the gas phase decomposition kinetics, surface chemistry processes, and film growth processes at high pressures.

Epitaxial InN growth has been achieved in the flow range of 8 slm and 12 slm with $R_{TMI:NH_3}$ varying from 1:400 to 1:8000 at growth temperatures of approximately 850°C. The ex-situ InN layer characterization indicates that the shift of the absorption edge from 1.8 eV down to approximate 0.7 eV is closely related to the precursor flow ratio and with it to stoichiometry of the InN layer. The structural characterization of the InN thin films by XRD found reflection features indicating both the presence of high quality InN and a strong dependence of these features on the precursor flow ratio. The initial results suggest that the optimum molar flow ratio, ammonia to TMI, under HPCVD conditions might be below 400, which is due to the efficient cracking of the nitrogen precursor at the high reactor pressure and high growth temperature. Further studies varying the ammonia to TMI flow ratio, the center flow velocity, and the growth temperatures will be needed to access the optimum growth window. Due to the good match with the GaN/AlN processing windows, HPCVD will be a valuable tool to explore indium rich group III-nitride alloys and heterostructures.

Acknowledgments:

We would like to acknowledge support of this work by NASA grant NAG8-1686, DOD MURI Grant F-49620-95-1-0447, the collaborative support by Prof. Ferguson's research group at Georgia Institute of Technology, and support through GSU-RPE.

7. Properties of InN grown by High Pressure CVD

7.1. Introduction

Indium rich group III-nitride compound semiconductor heterostructures in conjunction with wide bandgap $Ga_xAl_{1-x}N$ layers have many potential applications for novel devices that are of significant importance due to their large spectral tunability. Device structures based on $(Ga_{1-y-x}Al_yIn_x)N$ heterostructures and related alloys will enable the fabrication of high efficiency, monolithic integrated energy conversion systems and high speed optoelectronic devices for optical communications. Presently, the growth of group III nitrides is dominated by low-pressure deposition techniques such as organometallic chemical vapor deposition (OMCVD)[66] and molecular beam epitaxy (MBE) [72,101], relying on off-equilibrium growth conditions to stabilize and the control the growth process. This narrows the process parameter window and limits the temperature regime and the control of gas constituents, which is a challenge for the growth of high quality indium rich group III-Nitride alloys such as InGaN. At present, many of the fundamental properties of the InN compound itself are still in debate[72,102] such as band gap, lattice constants, effective electron mass and the influence of the intrinsic materials point defect chemistry on the optical and electrical properties[24]. The effects of extrinsic impurities such oxygen on the band gap [99,103] are currently being discussed as the origin of the wide variations in the measured physical properties of InN.

In order to understand and optimize the properties of InN and indium-rich alloys, new approaches for gaining insights and controlling the vastly different partial pressures in indium rich group III-alloys are required[24]. High-pressure chemical vapor deposition

(HPCVD)[104] is unique technique, specifically development to stabilize compounds with large differences in the partial pressures as encountered in the growth of InN and related materials. HPCVD utilizes reactor pressures up to 100 bar in order to counteract the decomposition of constituents and thereby stabilizes the surface at optimum growth temperatures. This is essential for controlling the point defect chemistry in indium-rich group III-nitride alloys. Previously demonstrated a successful suppression of InN decomposition for growth temperatures at around 850K-1100K[84,104], which is a major step toward the growth of indium-rich group III-nitride heterostructures. The main advantages of this method are

(a) the extended parameter space (e.g. precise control of precursor ratio, partial pressures, temporal separation of constituents, reactor pressure, or temperature) allows to explore and optimize the growth of InN in a process regime not accessible before,
(b) the implemented real-time optical diagnostics in the HPCVD provide crucial insight and understanding in to the gas phase and surface chemistry processes that govern the growth of InN and indium-rich group III nitrides alloys;
(c) the implemented precursor injection scheme enable the precise control and optimization of the gas phase reactions.

In this chapter, initial results on the structural and optical properties of InN layers grown by HPCVD are discussed.

7.3 Experimental Details

A high-pressure flow channel reactor with incorporated real time optical characterization capabilities is utilized to study and optimize InN nucleation and growth. Ammonia (NH_3) and trimethylindium (TMI) are employed in a pulsed injection scheme,

utilizing pulse width, precursor pulse separation, and cycle sequence time as growth control parameters. The pulsed precursors are embedded in a high-pressure carrier stream (ultra-pure nitrogen) and injected in the reactor utilizing a temporally controlled gas injection system. The total gas flow through the reactor as well as the reactor pressure are kept constant at all times during the growth. Ultraviolet absorption spectroscopy (UVAS) is applied in order to monitor the group-V and organometallic group-III precursors in the gas phase perpendicular to the gas flow at the center axis of the substrates [85,88]. The nucleation and growth process is monitored through the backside of the substrate, utilizing principle angle reflectance spectroscopy (PARS)[78] and laser light scattering (LLS). The InN layers discussed here were grown at a reactor pressure of 15 bar with total gas flows between 9 and 12 slm. The precursor flow ratio was evaluated for molar ratio of ammonia to TMI between 300 to 8000 and growth temperatures between 800 to 900 °C. All temperature settings refer to the calibrated correlation of the analyzed blackbody radiation as a function of the power setting of the substrate heater. The temperature is not corrected for the change in surface emissivity during the growth.

7.4 Results and Discussion

The structural properties of epitaxially InN films have been investigated using X-ray diffraction, Raman spectroscopy, and transmission spectroscopy. Figure 7.1 shows the variations of XRD patterns in a logarithmic scale for InN layers grown with ammonia

to TMI flow ratios of 8000, 500, 330, respectively. The XRD peak centered at 2θ= 31.28 deg corresponds to the diffraction of hexagonal phase InN(0002) plane. As the ammonia to TMI flow ratio is decreased to 500, the InN(0002) peak slightly broadens and a second peak in close proximity to the InN(0002) peak appears at the lower angle side.. A further decrease of the ammonia to TMI flow ratio down to ~300 leads to two sharp InN(0002) XRD peaks, as well as the an increase in the InN(101) and InN(100) peaks centered at 32.38 deg an 29.15 deg, respectively. The splitting of InN(0002) peak is observed in InN layers grown on both GaN/sapphire and sapphire substrates. The InN(101) diffraction peak positioned at 32.38 deg increases as the ammonia to TMI precursor ratio is lowered below 500, indication the formation of indium rich phases.

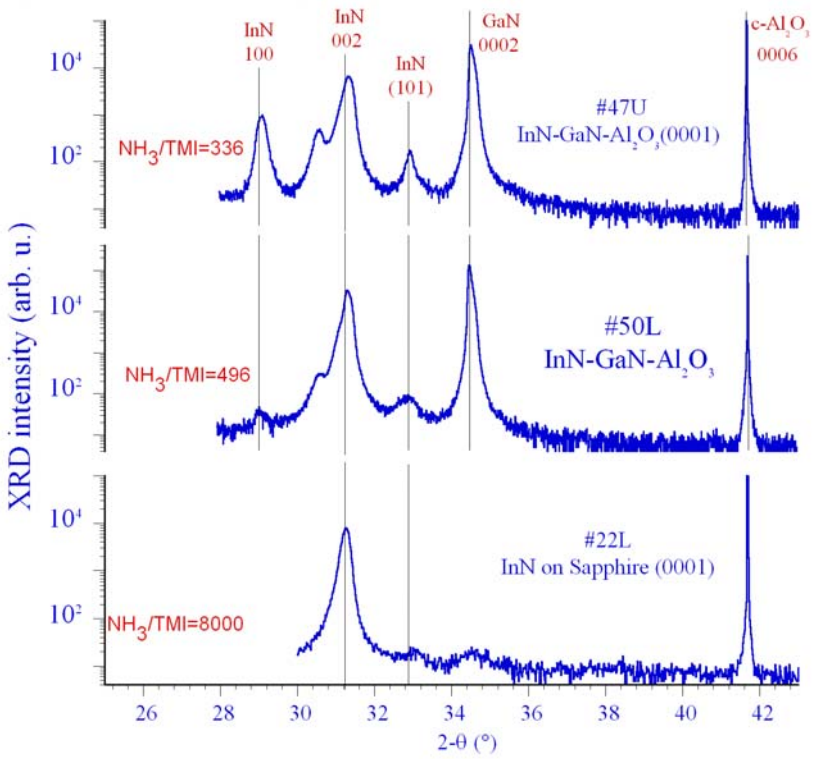

Figure 7.1: XRD spectra for InN layers grown on sapphire and GaN/ sapphire with the various NH_3/TMI ratio

Figure 7.2 shows Raman spectra of InN samples grown on sapphire (22U, 39U) and GaN/sapphire substrates (47U, 50L), which were analyzed using an excitation energy of 2.33 eV. The Raman spectra are observed in backscattering configuration. All spectra are normalized to the peak intensity of the E_2 (high) phonon feature. The three optical phonon modes of hexagonal InN at 300 K analyzed in Raman spectra are E_2 (high), A_1(LO), and B_1(high). The peak centered at wave numbers in range 489-492 cm^{-1} is attributed to the scattering of light from E_2 (high)- phonon modes which is most sensitive

to strain [105]; whereas, the peak at 587 cm^{-1} is assigned to A_1(LO) phonons in InN. As depicted in Figure 7.2, the A_1(LO) is suppressed in the spectra as the precursor flow ratio is increased. The observed peak positions are in good agreement with those found in InN layers grown by MBE and OMCVD[96]. Based on the allowed phonon mode peak positions for E_2 (high) and A_1(LO), our experimental peak positions are similar to the calculated value of 483 cm^{-1} and 588 cm^{-1} from Davydoc and Klochikhin[96].

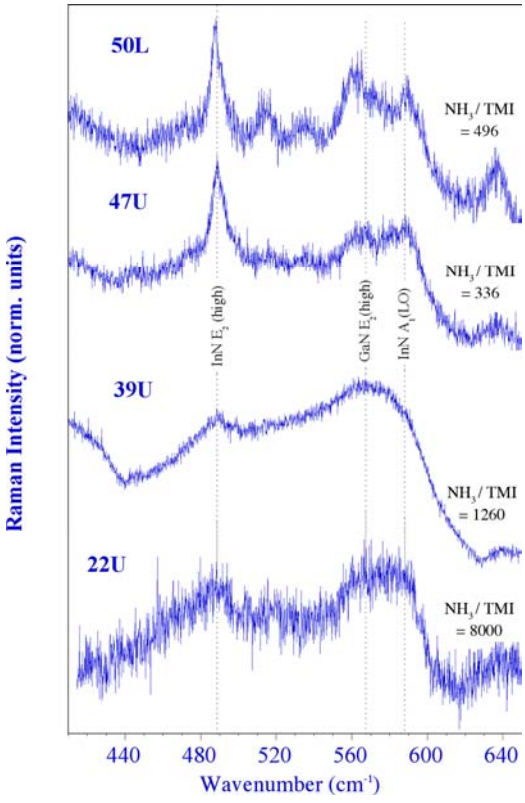

Figure 7.2: Raman spectra for InN layers grown on sapphire and GaN/ sapphire with the various NH_3/TMI ratio.

Figure 7.3 depicts the full width half maximum (FWHM) of the E_2 (high) mode together with the FWMH of the InN(0002) XRD peak plotted as a function of the precursor flow ratio. As the flow ratio decreases to 500, the FWHM of the E_2 (high) decreases. A sharp Lorentzian shaped E_2 (high) mode along with A_1(LO) and E_1(LO) mode indicates high quality hexagonal InN. Comparison with the XRD spectra shows, however, that with decreasing ammonia to TMI flow ratio the FWHM of InN(0002) XRD peak splits in two well defined structures. At the same time the InN(101) and InN(100) phases become stronger.

Figure 7.4 shows the absorption spectra observed for a set of characteristic samples; #22U, #32L, #38L, and #47L. As depicted in Figure 7.4, all samples show a dominant absorption structure centered at 0.63 eV. For the estimated ammonia to TMI precursor flow ratios (#22U / #32L $\rightarrow$ #38U $\rightarrow$ 47U) the absorption edge shifts downwards from an estimated 1.5 eV to approximate 0.7 eV, with absorption peaks / shoulders around 1.1 eV and 1.3 eV. The appearance and strength of these absorption centers coincide with the reduction of the ammonia to TMI precursor flow ratio, suggesting a close correlation between precursor ratio and the stoichiometry of the deposited InN layers. The absorption peak centered at 0.63 remains constant in strength and position. This feature has recently been assigned to plasmon excitations in the conduction band[106] due to large free carrier concentrations. If this theory proves correct,

it would suggest that the absorption edge shift towards lower energies is not directly related to the free carrier concentration, but rather to stoichiometry variations in InN.

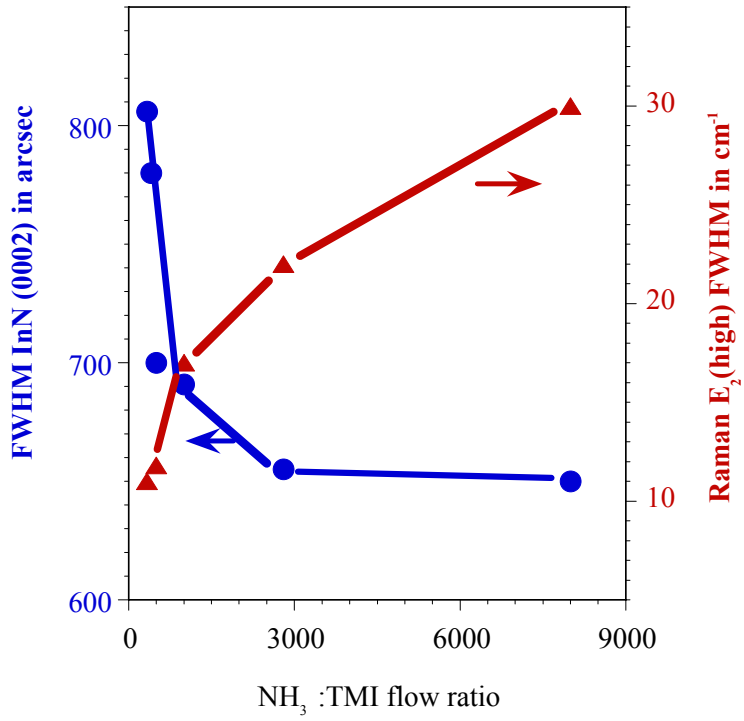

Figure 7.3: Correlation of Full width half maximum (FWHM) of Raman E2(high) and of InN(0002) XRD-peak intensity as function of molar ammonia to TMI flow ratio.

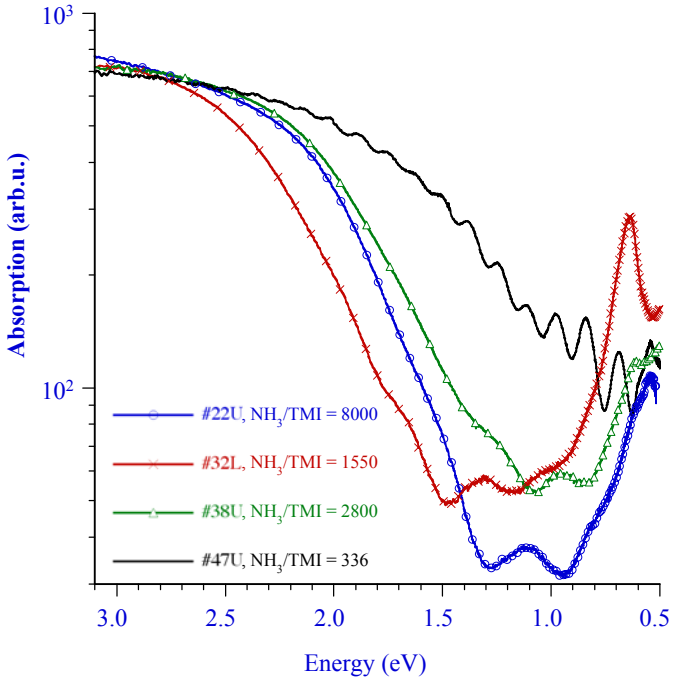

Figure 7.4: Shift of absorption edge for characteristic InN samples grown with different ammonia to TMI ratio.

7.4 Summary Conlusion

XRD, Raman, and absorption spectroscopy have been used to characterize InN epilayers grown under high-pressure CVD conditions on GaN/sapphire and sapphire substrates. HPCVD has been demonstrated to be a viable technique for the growth InN and related materials that exhibit high thermal decomposition pressures. Sharp E_2 (high) and A_1(LO) at 488 cm^{-1}, 590 cm^{-1} phonon modes are observed with decreasing ammonia to TMI flow ratio. The XRD results show that InN grown with higher NH_3:TMI flow ratios have smaller FWHM and are single phase in structure, while for decreasing

NH_3:TMI ratio multiple phases in XRD pattern are observed. Both XRD and Raman investigations revealed high structural quality of the InN epilayers with hexagonal symmetry. The absorption spectra indicate a shift of the absorption edge below 1 eV as the NH_3:TMI flow ratio decreases. The observed shifts indicate a wide homogeneity range in InN, accommodating excess indium as well as excess nitrogen in the lattice. A precise control of growth process parameter combined with real-time process characterization is required to gain more detailed insights in the growth chemistry and the associated InN material properties.

8. Recent Results and Future Work

8.1 Introduction

The previous chapters covering the design, implementation and results from our high pressure chemical vapor deposition reactor at Georgia State University clearly show that HPCVD is a viable means to produce high quality InN and In-rich group III-nitride thin films. While progress has been made in the calibration, optimization and production of InN thin films to date, there is still much effort required for this system to reach its full scientific potential. In this chapter, some recent results are presented, future worked is outlined and a brief discussion regarding the current debate over InN is presented.

8.2 Recent Results

While Chapters 6 and 7 covered many of the results from the InN reactor system, there are several new results that warrant inclusion in this thesis. Studies performed on the suface structure, composition and polarity of the InN thin films produced via HPCVD at Georgia State University have revealed N-polarity of the In-N and a 1x1 hexagonal LEED pattern. In addition, recent efforts in the effort to grow InN on p-type GaN epilayers has yielded single phase InN thin films, as indicated by XRD. The following two sections outline these results.

8.2.1 Surface structure of InN grown via HPCVD

Recent work into the structure and surface bonding configuration of InN thin films grown at Georgia State University have been performed by B.P. Bhatta, and B. D. Thoms[107]. This work is especially represents significant since is not as much fundamental information regarding the surface states of InN (and other group III-N) compared to conventional semiconductor compounds. These surface studies are an important part of understanding the underlying growth mechanisms, particularly nucleation and heteroepitaxial processes.

In this study, InN layers were grown via HPCVD at a growth temperature of 1100K and pressure of 15 bar. The NH_3:TMI precursor flow ratio was $\chi = 200$ (see Chapter 6). These InN layers were deposited on GaN epilayers on a sapphire (0001) substrate. The samples were cleaned in an acetone/isopropyl bath and mounted to a tantalum sample holder. The InN sample was placed in a Ultrahigh vacuum chamber (UHV) surface characterization system with a base pressure of 1.8×10^{-10} torr.

Auger electron spectroscopy (AES) revealed oxygen and carbon contamination in addition to In and N. The surface was then cleaned with a 1-keV nitrogen ion beam with a total flux of 560 $\mu C/cm^2$ at an incidence angle of 70° followed by 1000 $\mu C/cm^2$ at normal incidence. Full treatment of the experimental details have been accepted for publication[107].

Figure 8.1 shows the hexagonal 1x1 LEED pattern that was observed after several cycles of atomic hydrogen cleaning (AHC). This pattern was observed after a single cycle, but became clearer after several cycles. This pattern indicates that the surface is c-plane and well ordered. In addition, subsequent AES showed no carbon (which is in agreement with unpublished SIMS data) and a small oxygen content of < 3%. This is in agreement with AHC-cleaned InN produced via MBE[108].

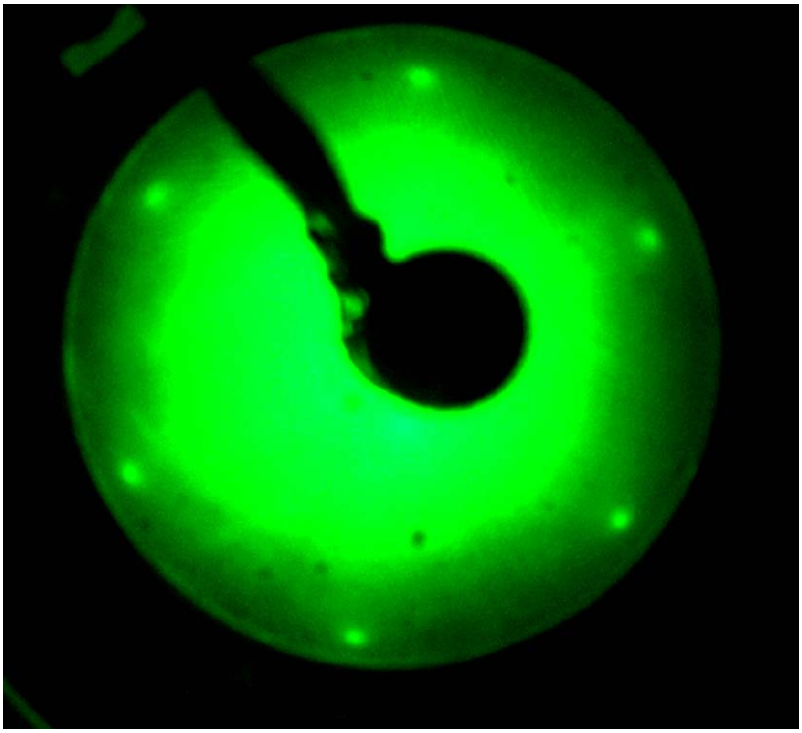

Figure 8.1: Low energy electron diffraction of AHC cleaned HPCVD-produced InN/GaN (39.5 eV incident energy).

8.2.2 InN thin films on GaN epilayers.

Recent efforts at Georgia State University aimed at the growth of InN on GaN epilayers has provided some encouraging results. The aim of this effort is to produce diode heterostructures with n-type InN on p-type GaN. as show in Figure 8.2. This is an important effort in light of the fact that p-type InN is, currently, not possible to produce. The ability to produce a light emitting diode structure based upon InN/GaN layers could potentially provide great insight in to the current debate regarding the fundamental band gap of InN. However, as discussed in Chapter 2, conventional OMCVD systems are not capable of producing high quality InN at the processing temperatures required to produce GaN.

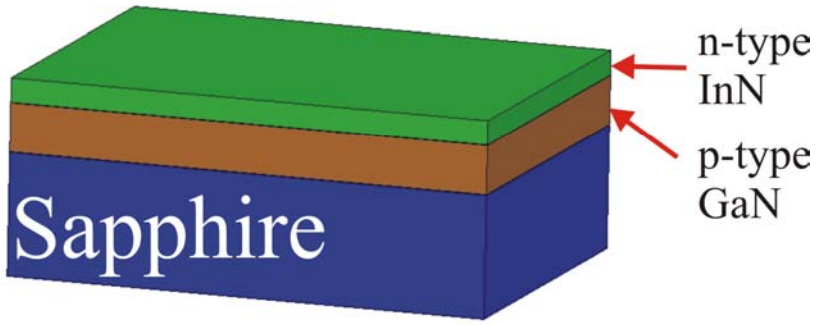

Figure 8.2: Schematic representation of n-type InN on p-type GaN epilayer.

InN layers were grown p-type GaN epilayers using the HPCVD reactor system at GSU. The reactor temperature was approximately 110K and the pressure kept constant at

15 bar. XRD analysis of the resultant 2 layer system was performed, the results are shown in Figure 8.3. As seen in the XRD results, the 2 layer system clearly shows the presence of single crystal InN on GaN epilayers. The FWHM of approximately 632 arc sec indicates good crystalline quality of the resultant layers. This result is particularly significant in that it clearly demonstrates a major point of the HPCVD design: ***HPCVD provides a closer match between the ideal processing temperature of InN and GaN!***

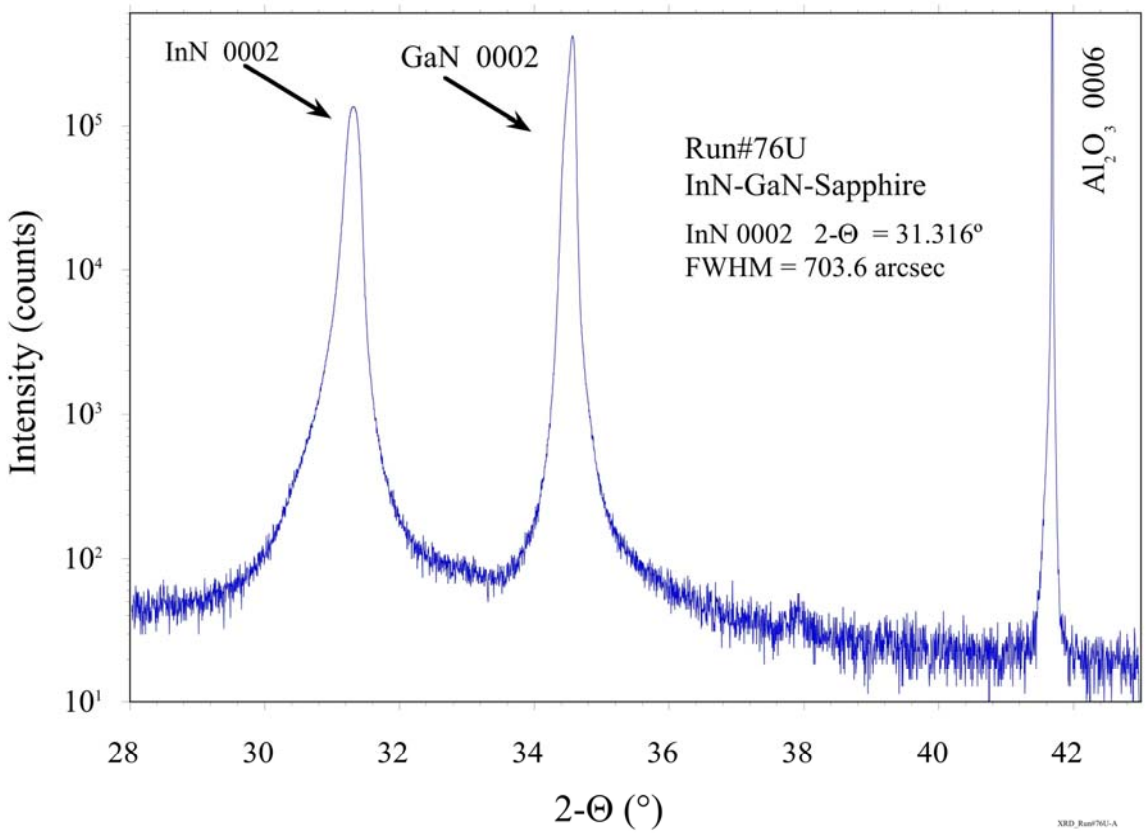

Figure 8.3: XRD analysis of InN thin films grown via HPCVD deposited on GaN epilayer. Sharp InN 0002 and the absence of other InN features indicates the presence of highly ordered single phase InN present.

8.3 Future work

While the HPCVD reactor system at Georgia State university has provided very good initial results for the epitaxy of InN thin films, there is significant future work needed in order to provide insight into the fundamental uncertainties surrounding InN. For this effort, future students will need to address several issues.

As discussed in the kinetic modeling section of Chapter 3, significant changes in the molar fraction of DMI occurs between and 20 and 50 bar. Currently, the HPCVD system is limited to approximately 17 bar, due to maximum pressure ratings of several component systems. This pressure limitation is just below the region of most interest with regard to molar DMI changes.The addition of a two stage nitrogen compressor in order to enable pressures of up to 50 bar would provide access to pressure regimes where DMI molar fractions are greatly reduced.

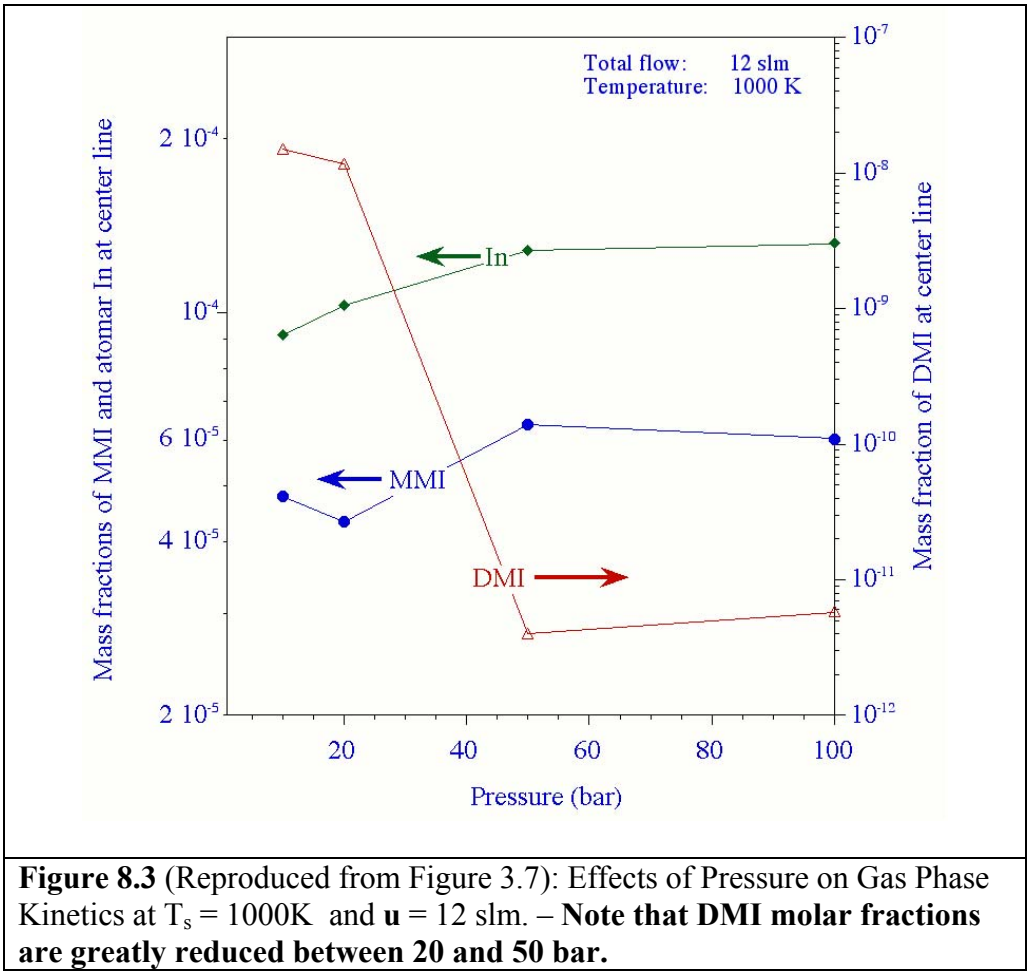

Figure 8.3 (Reproduced from Figure 3.7): Effects of Pressure on Gas Phase Kinetics at T_s = 1000K and **u** = 12 slm. – **Note that DMI molar fractions are greatly reduced between 20 and 50 bar.**

In addition, as shown in Figure 2.5 and continually discussed thoughout this work, access to higher pressures further stabilizes the InN at elevated pressures, preventing thermal etching and providing improved crystalline quality.

In addition to the increased pressure parameters for the HPCVD reactor, further work with regard to the characterization of the InN samples is desireable. While the current debate regarding the fundamental parameters of InN is not likely to be solved by any one research effort, the increased parameter space provided by this system does offer the opportunity to lend insight to the crucial discussion. The reader is refered to two excellent, and counter argued, reviews of the current uncertainty in the fundamental parameters of InN by Butcher[103] et al. and Monemar[109] et al. However, there is some interesting features in the aborption spectra of MBE produced InN that is also seen in the HPCVD samples. A key argument regarding the reduced band gap common in the MBE samples states that In clusters may be present. If that is the case, then Mie resonances would be present in the absorption spectra. As shown in Figure 8.4, Mie resonances are in fact observed in MBE grown InN when the samples are measured *at reduced temperatures.*

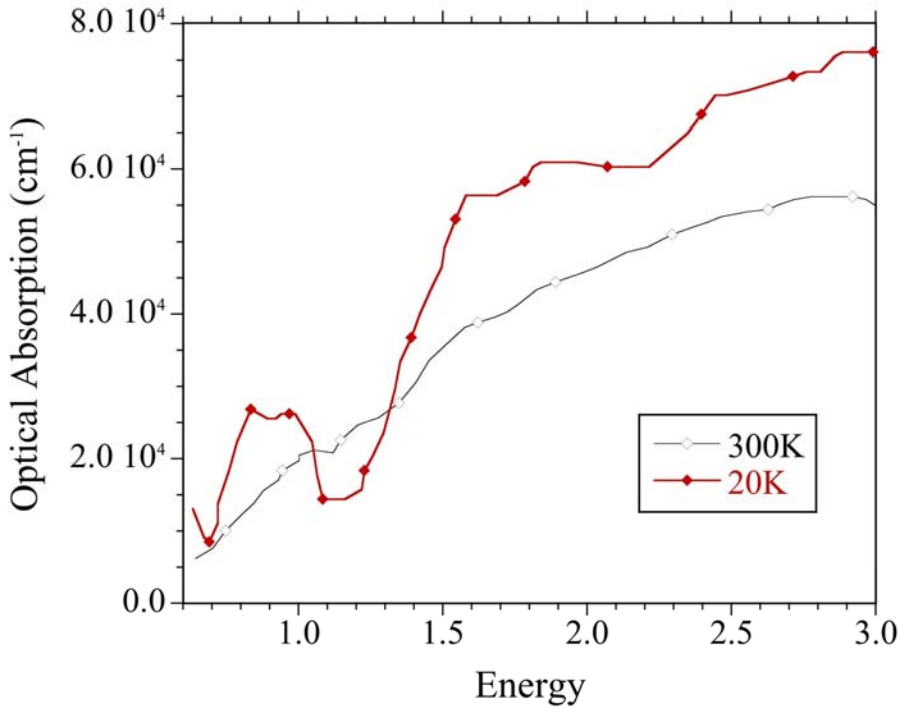

Figure 8.4: Optical absorption data from Shubina[110] et al. showing data for InN films at 300K and 20K. Mie resonant peaks are visible at 20K.

The reader is reminded of Figure 6.22 (shown here as Figure 8.5). The resonance features in question are clearly visible and change as a function of the precursor flow ration (and resultant InN film stoichiometry). The increased parameter space available to the HPCVD reactor system can provide a key tool to examine the influence of stoichiometry on the optical characteristics of the resultant InN thin films

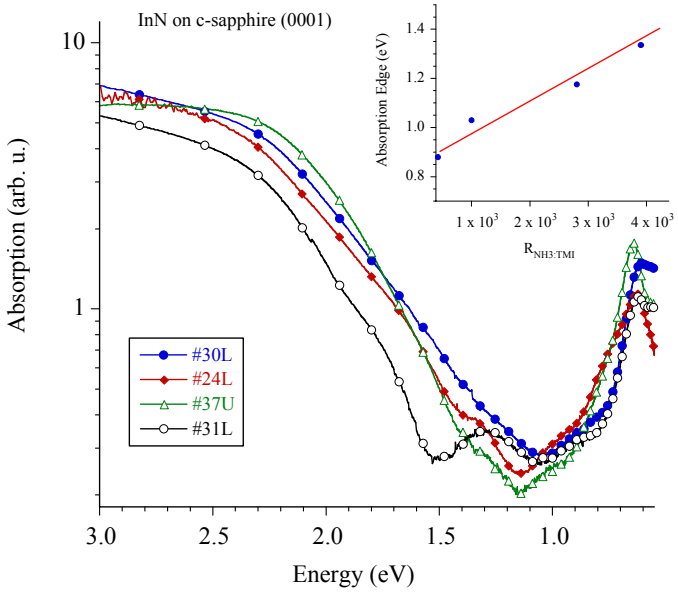

Figure 8.5 (FIGURE 6.22 REPRODUCED): Absorption spectra showing the possibility of resonance due to In clusters

REFERENCES

1 S. A. Wolf, A. Y. Chtchelkanova, and D. M. Treger, IBM Journal of Research and Development **40,** 101-110 (2006).

2 L. Geppert, Spectrum, IEEE **42,** 62-66 (2005).

3 R. Falster, V. V. Voronkov, and F. Quast, Physica Status Solidi B **222,** 219-44 (2000).

4 V. V. Voronkova and R. Falsterb, Journal of the Electrochemical Society **149,** G167-G174 (2002).

5 M. Futagami, Journal of Applied Physics **52,** 5575 (1981).

6 W. Shockley, Journal of Applied Physics **32,** 1402-1403 (1961).

7 F. J. Morin and J. P. Maita, Physical Review **96,** 28-35 (1954).

8 R. O. Carlson, Physical Review **104,** 937-941 (1956).

9 T. Buber, N. Kinayman, Y. Yong-Hoon, and J. Brogle, in *Low-loss high-isolation 60-80 GHz GaAs SPST PIN switch*, 2003, p. 1307-1310 vol.2.

10 INTEL, (2002).

11 Y. Taur, IBM Journal of Research and Development **46,** 213-222 (2002).

12 Y. Taur, D. A. Buchanan, C. Wei, D. J. Frank, K. E. Ismail, L. Shih-Hsien, G. A. Sai-Halasz, R. G. Viswanathan, H. J. C. Wann, S. J. Wind, and W. Hon-Sum, Proceedings of the IEEE **85,** 486-504 (1997).

13 C. W. Gwyn and P. J. Silverman, Proceedings of the SPIE - The International Society for Optical Engineering **5130,** 990-1004 (2003).

14 J. R. Birnbaum and S. Williams, Physics Today **53,** 38-42 (2000).

15 *Handbook of Condensed Matter and Materials Data* (Springer, 2005).

16 T. R. Weatherford and W. T. Anderson, Jr., Nuclear Science, IEEE Transactions on **50,** 704-710 (2003).

17 A. H. Johnston, (Jet Propulsion Laboratory, US Government, 2000).

18 P. G. Neudeck, R. S. Okojie, and L.-Y. Chen, Proceedings of the IEEE **90,** 1065-1076 (2002).

19 *GaN and Related Materials* (Gordon and Breach, New York, 1997).

20 Tokushima, Japan, 1997.

21 S. Nakamura and G. Fasol, *The Blue Laser Diodes* (Springer, 1997).

22 F. A. Ponce, *III-V Nitrides* (1997).

23 S. C. Jain, M. Willander, J. Narayan, and R. Van Overstraeten, Journal of Applied Physics **87,** 965-1006 (2000).

24 A. G. Bhuiyan, A. Hashimoto, and A. Yamamoto, Journal of Applied Physics **94,** 2779-2808 (2003).

25 B. E. Foutz, S. K. O'Leary, M. S. Shur, and L. F. Eastman, Journal of Applied Physics **85,** 7727-7734 (1999).

26 Juza R. and H. Hahn, Anorganic Allg Chem **239,** 282 (1938).

27 H. Grimmeiss and Z. H. Koelmans, Nature **14a,** 264 (1959).

28 H. P. Maruska and J. J. Tietjen, Applied Physics Letters **15,** 327-329 (1969).

[29] S. Yoshida, S. Misawa, and S. Gonda, Applied Physics Letters **42,** 427-429 (1983).
[30] I. Akasaki, H. Amano, M. Kito, and K. Hiramatsu, Journal of Luminosity **48&49,** 666 (1991).
[31] I. Akasaki, S. Sota, T. Tanaka, M. Koike, and H. Amano, Electronic Letters **32,** 1105 (1996).
[32] S. Nakamura, Applied Physics Letters **72,** 211 (1998).
[33] K. A. Brown, S. A. Ustin, L. Lauhon, and W. Ho, Journal of Applied Physics **79,** 7667.
[34] *Group III Nitride Semiconductor Compounds* (1997).
[35] T. S. Zheleva, O.-H. Nam, M. D. Bremser, and R. F. Davis, Applied Physics Letters **71,** 2472-2474 (1997).
[36] A. Sakai, H. Sunakawa, and A. Usui, Applied Physics Letters **71,** 2259-2261 (1997).
[37] A. M. Roskowski, E. A. Preble, S. Einfeldt, P. M. Miraglia, J. Schuck, R. Grober, and R. F. Davis, International Journal of High Speed Electronics and Systems **14,** 21-37 (2004).
[38] C. Hung-Seob, H. Young-Kue, H. Chang-Hee, C. Yoon-Ho, L. Shi-Jong, and L. Hyung Jae, Physica Status Solidi A **192,** 377-82 (2002).
[39] A. M. Roskowski, E. A. Preble, S. Einfeldt, P. M. Miraglia, J. Schuck, R. Grober, and R. F. Davis, Opto-Electronics Review **10,** 261-70 (2002).
[40] P. J. Schuck, R. D. Grober, A. M. Roskowski, S. Einfeldt, and R. F. Davis, Applied Physics Letters **81,** 1984-6 (2002).
[41] A. M. Roskowski, E. A. Preble, S. Einfeldt, P. M. Miraglia, and R. F. Davis, IEEE Journal of Quantum Electronics **38,** 1006-16 (2002).
[42] R. F. Davis, T. Gehrke, K. J. Linthicum, P. Rajagopal, A. M. Roskowski, T. Zheleva, E. A. Preble, C. A. Zorman, M. Mehregany, U. Schwarz, J. Schuck, and R. Grober, MRS Internet Journal of Nitride Semiconductor Research **7S1** (2002).
[43] W. Kim, O. Aktas, A. E. Botchkarev, A. Salvador, S. N. Mohammad, and H. Morkoc, Journal of Applied Physics **79,** 7657-7666 (1996).
[44] N. Grandjean and J. Massies, Applied Physics Letters **71,** 1816-1818 (1997).
[45] N. Grandjean and J. Massies, Applied Physics Letters **72,** 1078-1080 (1998).
[46] N. Grandjean, J. Massies, M. Leroux, and P. Lorenzini, Applied Physics Letters **72,** 82-84 (1998).
[47] O. Ambacher, A. Bergmair, M. S. Brandt, R. Dimitrov, G. Dollinger, R. A. Fischer, A. Miehr, T. Metzger, and M. Stutzmann, in *Thermal stability of group III-nitrides grown by OMCVD*, Berlin, Germany, 1996 (World Scientific), p. 561-4.
[48] J. B. McChesney and P. M. Bridenbaugh, Materials Research Bulletin **5,** 783 (1970).
[49] T. Renner, Anorganic Allg Chem **298,** 28 (1958).
[50] R. Juza and A. Rabenau, Anorganic Allg Chem **298,** 28 (1956).
[51] H. J. Hovel and J. J. Cuomo, Applied Physics Letters **20,** 71-73 (1972).

[52] L. A. Marasina, I. G. Pichugin, and M. Tlaczala, Kristal Technology **12,** 541 (1977).
[53] T. Matsuoka, H. Tanaka, T. Sasaki, and A. Katsui, Karuizawa, Japan, 1989 (Institute of Physics), p. 141.
[54] A. Wakahara and A. Yoshida, Applied Physics Letters **54,** 709-711 (1989).
[55] K. J. Bachmann, S. McCall, S. LeSure, N. Sukiji, and F. Wang, Journal of the Japanese Society for Microgravity Applications **15,** 436 (1998).
[56] K. J. Bachmann, B. H. Cardelino, C. E. Moore, C. A. Cardelino, N. Sukidi, and S. McCall, Materials Research Society Proceedings **569,** 59 (1999).
[57] N. Dietz, S. McCall, and K. J. Bachmann, Proceedings of the Microgravity Conference 2000**,** 176-181 (2001).
[58] M. J. Jacko and S. J. W. Price, Canadian Journal of Chemistry **42,** 1198 (1964).
[59] J. Haigh and O'Brien, Journal of Crystal Growth **68,** 550-556 (1984).
[60] N. I. Buchan and J. M. Jasinski, Journal of Crystal Growth **106,** 227-238 (1990).
[61] C. A. Cardelino, C. E. Moore, B. H. Cardelino, N. Zhou, S. A. Lowry, A. Krishnan, D. O. Frazier, and K. J. Bachmann, in *Development of an advanced computational model for OMCVD of indium nitride*, San Jose, CA, USA, 1999 (SPIE), p. 447-458.
[62] D. A. Lax, in *Taschenbuch fur Chemiker and Physiker, Band I*, edited by E. Lax and C. Synowietz (Spring, Berlin, 1967).
[63] C. R. Abernathy, S. J. Pearton, F. Ren, and P. W. Wisk, Journal of Vacuum Science & Technology B (Microelectronics Processing and Phenomena) **11,** 179-82 (1993).
[64] D. Yuan-Tung, L. Ying-Tsang, L. Ray-Ming, L. Ming-Chih Harris, C. Yang-Fang, L. Si-Chen, and L. Hao-Hsiung, Japanese Journal of Applied Physics, Part 2 (Letters) **36,** 811-14 (1997).
[65] S. Yamaguchi, M. Kariya, S. Nitta, T. Takeuchi, C. Wetzel, H. Amano, and I. Akasaki, Journal of Applied Physics **85,** 7682-8 (1999).
[66] T. Schmidtling, M. Drago, U. W. Pohl, and W. Richter, Journal of Crystal Growth **248,** 523-7 (2003).
[67] O. Ambacher, M. S. Brandt, R. Dimitrov, T. Metzger, M. Stutzmann, R. A. Fischer, A. Miear, A. Bergmaier, and G. Dolinger, Journal of Vacuum Science & Technology B (Microelectronics and Nanometer Structures) **14,** 3532-42 (1996).
[68] T. Matsuoka, H. Okamoto, M. Nakao, H. Harima, and E. Kurimoto, Applied Physics Letters **81,** 1246-1248 (2002).
[69] U. Grossner, J. Furthmuller, and F. Bechstedt, Applied Physics Letters **74,** 3851-3853 (1999).
[70] Z. X. Bi, R. Zhang, Z. L. Xie, X. Q. Xiu, Y. D. Ye, B. Liu, S. L. Gu, B. Shen, Y. Shi, and Y. D. Zheng, Materials Letters **58,** 3641-4 (2004).
[71] J. Aderhold, V. Y. Davydov, F. Fedler, H. Klausing, D. Mistele, T. Rotter, O. Semchinova, J. Stemmer, and J. Graul, Journal of Crystal Growth **222,** 701-705 (2001).

[72] V. Y. Davydov, A. A. Klochikhin, V. V. Emtsev, D. A. Kurdyukov, S. V. Ivanov, V. A. Vekshin, F. Bechstedt, J. Furthmuller, J. Aderhold, J. Graul, A. V. Mudryi, H. Harima, A. Hashimoto, A. Yamamoto, and E. E. Haller, Physica Status Solidi B **234,** 787-95 (2002).

[73] F.-H. Yang, S. Jih, Hwang, K.-H. Chen, Y.-J. Yang, T.-H. Lee, L.-G. Hwa, and L.-C. Chen, Thin Solid Films **405,** 194-197 (2002).

[74] V. Y. Malakhov, Solar Energy Materials and Solar Cells **76,** 637-646 (2003).

[75] V. Y. Davydov, A. A. Klochikhin, V. V. Emtsev, A. V. Sakharov, S. V. Ivanov, V. A. Vekshin, F. Bechstedt, J. Furthmuller, J. Aderhold, J. Graul, A. V. Mudryi, H. Harima, A. Hashimoto, A. Yamamoto, J. Wu, H. Feick, and E. E. Haller, in *Band gap of hexagonal InN and InGaN alloys*, St. Petersburg, Russian Federation, 2003 (The International Society for Optical Engineering), p. 68-71.

[76] B. Onderka, J. Unland, and R. Schmid-Fetzer, Journal of Materials Research **17,** 3065-83 (2002).

[77] N. Dietz, S. McCall, and K. J. Bachmann, in *NASA/CP-2001-210827*, 2001 (Nasa).

[78] N. Dietz, V. Woods, S. McCall, and K. J. Bachmann, in *NASA/CP-2003-212339*, Huntsville, Alabama, 2002 (NASA), p. 169.

[79] N. Dietz, H. Bom, M. Strassburg, and V. Woods, in *Real-time optical monitoring of gas phase dynamics for the growth of InN at elevated pressures*, Boston, MA, USA, 2004 (Mater. Res. Soc), p. 249-54.

[80] N. Dietz, M. Strassburg, and V. Woods, in *Real-time optical monitoring of ammonia flow and decomposition kinetics under high-pressure chemical vapor deposition conditions*, Anaheim, CA, USA, 2005 (AIP for American Vacuum Soc), p. 1221-7.

[81] S. D. McCall and K. J. Bachmann, in *Three-dimensional modeling of the high pressure organometallic chemical vapor deposition of InN using trimethylindium and ammonia*, Boston, MA, USA, 2002 (Mater. Res. Soc), p. 73-80.

[82] B. H. Cardelino, C. E. Moore, C. A. Cardelino, S. D. McCall, D. O. Frazier, and K. J. Bachmann, J. Phys. Chem. A **107,** 3708-3718 (2003).

[83] B. H. Cardelino, C. E. Moore, S. McCall, C. A. Cardelino, N. Dietz, and K. J. Bachmann, 117-3 (2004).

[84] N. Dietz, M. Alevli, V. Woods, M. Strassburg, H. Kang, and I. T. Ferguson, Physica Status Solidi B **242,** 2985-94 (2005).

[85] G. A. Hebner, K. P. Killeen, and R. M. Biefeld, Journal of Crystal Growth **98,** 293-301 (1989).

[86] G. A. Hebner and K. P. Killeen, Journal of Applied Physics **67,** 1598-1600 (1990).

[87] H. Okabe, M. K. Emadi-Babaki, and V. R. McCrary, Journal of Applied Physics **69,** 1730-1735 (1991).

[88] M. C. Johnson, K. Poochinda, N. L. Ricker, J. W. Rogers Jr, and T. P. Pearsall, Journal of Crystal Growth **212,** 11-20 (2000).

[89] B. H. Cardelino, C. E. Moore, C. A. Cardelino, D. O. Frazier, and K. J. Bachmann, J. Phys. Chem. A **105,** 849-868 (2001).

[90] V. Woods, H. Born, M. Strassburg, and N. Dietz, Journal of Vacuum Science & Technology A (Vacuum, Surfaces, and Films) **22,** 1596-9 (2004).
[91] V. Woods, J. Senawirante, and N. Dietz, in *Nucleation and growth of InN by high-pressure chemical vapor deposition: optical monitoring*, Anaheim, CA, USA, 2005 (AIP for American Vacuum Soc), p. 1790-4.
[92] J. A. Syage, R. B. Cohen, and J. Steadman, The Journal of Chemical Physics **97,** 6072-6084 (1992).
[93] F. Z. Chen, D. L. Judge, C. Y. R. Wu, and J. Caldwell, Planetary and Space Science **47,** 261-266 (1998).
[94] J. A. McCaulley, R. J. Shul, and V. M. Donnelly, Journal of Vacuum Science & Technology A (Vacuum, Surfaces, and Films) **9,** 2872-886 (1991).
[95] J. Haigh and S. O'Brien, Journal of Crystal Growth **68,** 550-556 (1984).
[96] V. Y. Davydov and A. A. Klochikhin, Semiconductors **38,** 861-898 (2004).
[97] Z. Sitar, M. J. Paisley, B. Yan, J. Ruan, W. J. Choyke, and R. F. Davis, in *Growth of AlN/GaN layered structures by gas source molecular-beam epitaxy*, Raleigh, NC, USA, 1990, p. 316-22.
[98] J. M. Van Hove, G. Carpenter, E. Nelson, A. Wowchak, and P. P. Chow, Journal of Crystal Growth **164,** 154-158 (1996).
[99] E. Kurimoto, M. Hangyo, H. Harima, M. Yoshimoto, T. Yamaguchi, T. Araki, Y. Nanishi, and K. Kisoda, Applied Physics Letters **84,** 212-214 (2004).
[100] N. Dietz, Materials Science and Engineering B: Solid-State Materials for Advanced Technology **87,** 1-22 (2001).
[101] T. Tsuchiya, M. Ohnishi, A. Wakahara, and A. Yoshida, Journal of Crystal Growth **220,** 191-196 (2000).
[102] T. Inushima, V. V. Mamutin, V. A. Vekshin, S. V. Ivanov, T. Sakon, M. Motokawa, and S. Ohoya, Journal of Crystal Growth **227-228,** 481-485 (2001).
[103] K. S. A. Butcher and T. L. Tansley, Superlattices and Microstructures **38,** 1-37 (2005).
[104] N. Dietz, in *III-Nitrides Semiconductor Materials*, edited by Z. C. Feng (Imperial Press, 2005), p. 203-235.
[105] V. Y. Davydov, V. V. Emtsev, I. N. Goncharuk, A. N. Smirnov, V. D. Petrikov, V. V. Mamutin, V. A. Vekshin, S. V. Ivanov, M. B. Smirnov, and T. Inushima, Applied Physics Letters **75,** 3297-3299 (1999).
[106] D. B. Haddad, J. S. Thakur, V. M. Naik, G. W. Auner, R. Naik, and L. E. Wenger, Materials Research Society Proceedings **743,** L11.22 (2003).
[107] R. P. Bhatta, B. D. Thoms, M. Alevli, V. Woods, and N. Dietz, Applied Physics Letters **Accepted** (2006).
[108] L. F. J. Piper, T. D. Veal, M. Walker, I. Mahboob, C. F. McConville, H. Lu, and W. J. Schaff, Journal of Vacuum Science & Technology A: Vacuum, Surfaces, and Films **23,** 617-620 (2005).
[109] B. Monemar, P. P. Paskov, and A. Kasic, Superlattices and Microstructures **38,** 38-56 (2005).

[110] S. V. I. V. N. J. M. M. G. A. P. K. M. G. T. A. V. J. L. A. K. T. V. Shubina, physica status solidi (a) **202,** 377-382 (2005).